

# Non-thermal emission modelling of the Crab Nebula

DISSERTATION  
ZUR ERLANGUNG DES DOKTORGRADES  
DES DEPARTMENT PHYSIK  
DER UNIVERSITÄT HAMBURG

vorgelegt von

**Ludmilla Dirson**  
aus Frankreich

Hamburg  
2020

Gutachter der Dissertation:	Prof. Dr. Dieter Horns Prof. Dr. Günter Sigl
Zusammensetzung der Prüfungskommission:	Prof. Dr. Marcus Brüggem Dr. Rolf Bühler Prof. Dr. Dieter Horns Prof. Dr. Jochen Liske Prof. Dr. Daniela Pfannkuche
Vorsitzende der Prüfungskommission:	Prof. Dr. Jochen Liske
Datum der Disputation:	06.07.2020
Vorsitzender Fach-Promotionsausschusses PHYSIK:	Prof. Dr. Günter Sigl
Leiter des Departments Physik:	Prof. Dr. Wolfgang Hansen
Dekan der MIN Fakultät:	Prof. Dr. Heinrich Graener

*“Il faut beaucoup savoir pour savoir qu’on n’en sait pas beaucoup. Celui qui ne sait rien croit tout savoir. ”*

René Bellaïche

# Abstract

Located at a distance of 2 kpc from us, the Crab Nebula is an astrophysical source which has been observed since 1054. It provides an exceptionally bright non-thermal emission throughout the whole observational range of photon energies. The numerous observations of the Crab Nebula, allows for a more complete and detailed study than with any other non stellar object. However, it has recently been demonstrated that the shape of its spectrum in the high to very-high energy (HE-VHE) range is not well-described anymore by state-of-the art modelling of the nebula.

In this thesis, the non-thermal emission model of the Crab Nebula is reexamined, and the spatial distribution of the seed photons coming from the thermal emission of the dust is included for the first time in detail. The spatial overlap between the soft photons and the ultra relativistic electrons is calculated in order to determine the inverse Compton flux, as well as the spectral morphology of the Crab Nebula in the high to very-high-energy (HE-VHE) range. Under the assumption of a constant magnetic field model, modelling of both the synchrotron and IC emission components provides the average magnetic field inside the Crab Nebula:  $B = (167 \pm 6 \text{ (stat.)}_{-6}^{+15} \text{ (sys.)}) \mu\text{G}$ . The scale length of the electrons distribution is inferred from the spatial extension of the synchrotron emission. The dust emissivity is modeled with a two temperature gray body and is assumed to be located in a shell of thickness  $\sim 0.6$  pc. The size of the nebula is determined by calculating its 68% containment radius. In order to do so, the intensity is calculated by integration of the inverse Compton emissivity along the line of sight.

The constant  $B$ -field model reproduces well the synchrotron emission, but underestimates the IC flux in the high energy regime. Furthermore, it fails to describe the  $\gamma$ -ray extension, especially in the 5-20 GeV energy range. This may be due to the presence of electrons coming from the outer shell of the nebula, which would contribute to the low energy IC flux. Therefore, a more detailed treatment of the magnetic field structure is required to explain for both the IC part of the spectral energy distribution (SED) and the size of the nebula when viewed in the gamma-ray regime. A more realistic approach is used to model the magnetic field by a step function. Assuming that electrons at the unseen outer shell of the nebula are located at an angular size of  $\sim 0.2$  deg, a lower limit

on the low energy IC flux produced by the electrons confined in the radio nebula can be estimated. Taking this into account, the best values for the parameters describing the magnetic field in a step model are determined. The IC flux is recalculated, and it is shown that the data are better described by a varying magnetic field.

The inverse-Compton component of the energy spectrum from the Crab nebula is used to cross-calibrate the Fermi-LAT flux measurements with ground-based flux measurements. It was shown that the relative shift of the energy scale among ground based telescopes is smaller than the estimated systematic uncertainty of the instruments (15%).

# Kurzfassung

Der Krebsnebel in 2 kpc Entfernung ist eine astrophysische Quelle, die schon seit dem Jahr 1054 beobachtet wird. Er liefert besonders helle, nicht-thermische Emissionen über den gesamten Bereich beobachtbarer Photonenergien. Die zahlreichen Beobachtungen des Krebsnebels ermöglichen eine vollständigere und detailliertere Erforschung, als es mit jedem anderen nicht stellaren Objekt möglich ist. Jedoch wurde vor kurzem gezeigt, dass die Form seines Spektrums im hoch- bis sehrhochenergetischen (HE-VHE) Bereich nicht gut durch die aktuellen Modelle beschrieben wird. In dieser Dissertation wird das nicht-thermische Emissionsmodell des Krebsnebels überprüft und die räumliche Verteilung der “Saar-Photonen”, die durch thermische Emission des Staubes erzeugt werden, zum ersten Mal detailliert berücksichtigt. Der räumliche Überlapp von weichen Photonen und ultrarelativistischen Elektronen wird berechnet, um den inversen Compton-Fluss (IC) sowie die spektrale Morphologie des Krebsnebels im HE-bis-VHE-Bereich zu bestimmen. Unter der Annahme eines Modells mit konstantem Magnetfeld erhält man durch Modellieren sowohl der Synchrotron und IC-Emissions-Komponente das durchschnittliche Magnetfeld innerhalb des Krebsnebels:  $B = (167 \pm 6 \text{ (stat.)}_{-6}^{+15} \text{ (sys.)}) \mu\text{G}$ . Von der räumlichen Ausdehnung der Synchrotronemissionen wird auf die Skalenlänge der Elektronenverteilung geschlossen. Die Emissivität des Staubes wird mit einem grauen Körper zweier Temperaturen modelliert, von dem angenommen wird, dass er sich in einer Hülle mit einer Breite von  $\sim 0.6$  pc befindet. Die Bestimmung der Grösse des Nebels erfolgt durch Berechnung des Radius, in dem sich 68% der Emissionen befinden. Dafür wird die Intensität durch Integration der inversen Compton-Emissivität entlang der Sichtlinie berechnet. Das Modell mit konstantem Magnetfeld reproduziert die Synchrotronemissionen gut, aber es unterschätzt den IC-Fluss im HE-Regime. Ausserdem versagt es, darin, die Grösse des Nebels bei Beobachtung im Gammastrabereich zu beschreiben, besonders zwischen Energien von 5-20 GeV. Dies könnte am Vorhandensein von Elektronen aus der äusseren Hülle des Nebels liegen, welche zum niedrigerenergetischen IC-Fluss beitragen würden. Daher ist eine detailliertere Behandlung der magnetischen Feldstruktur vonnöten, um sowohl den IC-Teil der spektralen Energieverteilung als auch die Grösse im Gammabereich des Krebsnebels zu erklären. Ein realistischerer Ansatz wird benutzt, um das Magnetfeld mit einer Stufenfunktion zu modellieren. Unter

der Annahme, dass sich die Elektronen am äusseren Rand des Nebels in einer Winkelausdehnung von  $\sim 0.2$  deg befinden, kann eine untere Schranke für den niedrigerenergetischen IC-Fluss, der von im Radionebel eingeschlossenen Elektronen erzeugt wird, abgeschätzt werden. Unter Berücksichtigung dessen werden in einem Stufenmodell die besten Parameter für dieses Magnetfeld bestimmt. Der IC-Fluss wird neu berechnet und es wird gezeigt, dass die Daten besser durch ein variiertes Magnetfeld beschrieben werden. Die IC-Komponente des Energiespektrums des Krebsnebels wird benutzt, um die Messungen des Flusses von Fermi-LAT mit bodengestützten Flussmessungen querzukalibrieren. Es wird gezeigt, dass die relative Verschiebung der Energieskala unter bodengestützten Teleskopen kleiner ist als die geschätzte systematische Unsicherheit der Instrumente (15%).



# Contents

<b>Abstract</b>	<b>iii</b>
<b>Kurzfassung</b>	<b>v</b>
<b>1 Introduction</b>	<b>1</b>
1.1 The Crab Nebula . . . . .	2
1.1.1 Supernovae . . . . .	2
1.1.2 Components of the Supernova Remnant SN1054 . . . . .	3
1.2 Observations from the Crab Nebula . . . . .	7
1.2.1 Spectral Energy Distribution . . . . .	9
1.2.2 Morphology . . . . .	12
1.3 Modelling Pulsar Wind Nebulae . . . . .	12
1.3.1 Radiative models of PWNe . . . . .	13
1.3.2 Acceleration in supernovae remnants (SNRs) . . . . .	15
1.3.3 Relevant radiation processes . . . . .	22
1.3.4 Dynamics of a supernova remnant . . . . .	29
<b>2 Non-thermal emission model of the Crab Nebula</b>	<b>33</b>
2.1 Synchrotron and Inverse Compton emission from the Crab Nebula . . . . .	34
2.1.1 Synchrotron emission from the Crab Nebula . . . . .	34
2.1.2 Inverse Compton emission . . . . .	35
2.2 Relativistic electrons in the Crab Nebula . . . . .	35
2.2.1 Two populations of electrons . . . . .	35
2.2.2 Estimation of the electrons spatial distribution from observations . . . . .	36
2.2.3 Maximum value of the magnetic field . . . . .	41
2.2.4 Modeled electron Energy spectrum . . . . .	42
2.3 Seed photon fields in the Nebula . . . . .	43
2.3.1 Scattering of IR photons from heated dust . . . . .	44
2.3.2 Synchrotron self-Compton scattering . . . . .	47
2.3.3 Scattering of the 2.7 K cosmic microwave background . . . . .	50
<b>3 Spectral Energy Distribution and Energy-dependent Gamma-ray Morphology of the Crab Nebula in a constant magnetic field model</b>	<b>51</b>

---

3.1	Spectral energy distribution . . . . .	51
3.1.1	Best value of the the average magnetic field . . . . .	52
3.1.2	Electron spectra . . . . .	55
3.2	Extension . . . . .	59
3.2.1	Definition of the Intensity . . . . .	59
3.2.2	Calculation of the intensity . . . . .	63
3.2.3	Verification of the model . . . . .	65
3.2.4	Comparison with the Data . . . . .	70
3.3	Conclusion . . . . .	73
<b>4</b>	<b>Modelling of the Crab Nebula with a varying magnetic field</b>	<b>74</b>
4.1	Magnetic field structure . . . . .	74
4.2	Best fitting parameters for the varying magnetic field . . . . .	77
4.3	Cross calibration of IACTs and Fermi . . . . .	80
4.4	Conclusion . . . . .	83
<b>5</b>	<b>Summary and conclusion</b>	<b>84</b>
<b>A</b>	<b>Derivation of the expression of the spectral number density</b>	<b>86</b>
<b>B</b>	<b>Chandra images of the Crab Nebula in different energy bands</b>	<b>88</b>
<b>C</b>	<b>Program</b>	<b>92</b>
<b>D</b>	<b>Acronyms</b>	<b>97</b>
<b>E</b>	<b>Definition of the 68% containment radius</b>	<b>98</b>
	<b>List of Figures</b>	<b>100</b>
	<b>List of Tables</b>	<b>106</b>
	<b>Bibliography</b>	<b>107</b>
	<b>Acknowledgements</b>	<b>130</b>



*Dedicated to my parents and my brothers . . . .*



# Chapter 1

## Introduction

Cosmic rays are omnipresent in our Galaxy and display a power-law spectrum in their energy distribution up to a “knee” at around  $10^{15}$  eV, where the power law steepens. One century after their discovery, cosmic-rays still raise many questions. Developing an adequate theory for the origin of cosmic rays (CRs hereafter) is a problem that relies on two fundamental parts that, coupled together may present a consistent description of what we observe: a model of particle acceleration in a class (or more than one class) of sources and a model for transport of these particles from their sources to Earth. Supernova remnants are extremely important for understanding our galaxy because they are believed to be responsible for the acceleration of Galactic cosmic rays.

The Crab Nebula is one of the most observed Galactic sources and is studied in almost every branch of astrophysics. Thanks to the wealth of measurements covering an energy range of more than 15 orders of magnitude, and high resolution X-ray imaging, it is possible to develop a detailed model of the broad band spectrum of the nebula as well as its morphology in different energy bands. The combination of measurements and numerical codes has opened new avenues of investigation and exciting progress in the recent years. The spatial and spectral structure of the non-thermal synchrotron emission is known in exceptional detail while the emission from the nebula in the GeV-TeV energies has just recently been spatially resolved. Furthermore, recent measurements in the GeV-TeV range demonstrate that state of the art models of the Crab Nebula do not describe well the IC component anymore [[Aleksić et al. \(2015\)](#)]. Moreover, the Crab Nebula still raises many questions. The acceleration mechanism, the functioning of the pulsar wind, and pulsar magnetosphere that powers pulsar wind nebulae (PWNe) are still not well understood. The origin of its birth is also a long-standing problem.

This work therefore presents an updated model for the non-thermal emission of the Crab Nebula, as well as description of its gamma ray morphology. First, the Crab Nebula

and its different components are introduced. Then, the data set used in this work for the modelling of the broad band emission is presented. Finally, the key concepts for the understanding of PWNe modelling are discussed.

## 1.1 The Crab Nebula

Located at a distance of  $d \approx 2$  kpc [Trimble (1968)], the Crab Nebula is the remnant of a supernova explosion which occurred on the 4th of July 1054 (SN1054). Many historical sources describing the event have been found. In particular, Chinese and Japanese records provide the 4th of July as the explosion date [Ho et al. (1972)]. For the first time, the work of Duyvendak (1942) and Mayall and Oort (1942) authenticate the Crab Nebula as being the remnant of SN1054. After the nebula was rediscovered by the English astronomer John Bevis in 1731, it was observed by Charles Messier which, in 1758, recorded it as the first object in his catalog of astronomical objects [Hester (2008)]. SN1054 had a luminosity and light curve which are approximately consistent of those of a core-collapse supernova [Chevalier (1977)]. The presence of a generous amount of hydrogen also strongly suggests a core-collapse origin.

### 1.1.1 Supernovae

**Core-collapse supernova:** Very massive stars having masses in the range of  $8M_{\odot} - 10M_{\odot}$ <sup>1</sup> are fusing in their core elements up to nickel ( $^{56}\text{Ni}$ ) and iron ( $^{56}\text{Fe}$ ) [Unsöld and Baschek (2002)]. When further energy production by nuclear fusion reaches a limit, the center of the star can no longer oppose the radiation pressure to its own gravity and it comes to a gravitational collapse. This is followed by an outward propagating shockwave which heats up the shell of the core and propel it outward. This explosion, called a *supernova*, releases energy of  $\approx 10^{53}$  erg. About 99% of the energy is emitted in the form of neutrinos, the remaining percent is converted into kinetic energy in the shell and electromagnetic radiation.

**Neutron star:** Depending on the mass of the predecessor star, gravitational collapse can lead to the formation of a neutron star, which was already discussed by Baade and Zwicky (1934). The pressure in such a star is so high that neutrons are created through the inverse  $\beta$  decay by the process  $e^{-} + p \rightarrow n + \nu_e$ . The resulting neutrons are stable because all the states in the phase space are occupied by the high number of electrons in the star. The occupancy of each infinitesimal volume element  $d\Omega = d^3x d^3p$  of this 6-dimensional space is determined by the Pauli principle for fermions: each unit cell

<sup>1</sup> $M_{\odot}$  stands for the solar mass and is  $\simeq 1.989 \cdot 10^{33}$ g.

can be occupied maximally with two electrons (one for each spin orientation). This is described by Fermi-Dirac statistics. In the neutron star, the densities are so high that all volume elements are filled to a certain energy, which is greater than the maximum allowed energy of the electrons at  $\beta$ -decay. Thus, the decay is suppressed. Note, that the neutron star does not collapse into a black hole due to the Pauli principle. Inside the star, the density of the strongly incompressible neutron matter is estimated to be  $\rho \gtrsim 10^{14} \text{ g cm}^{-3}$  [Unsöld and Baschek (2002)]. The radii of neutron stars are typically expected to be on the order of  $\mathcal{O}(10)$  km which, assuming conservation of the angular momentum of the parent star, results in a very fast rotation of the star. Such fast rotating neutron stars are called *pulsars* because they emit radiation of radio to gamma energies in a collimated beam similar to that of a lighthouse. The star in the center of the Crab Nebula is such a pulsar. The individual components of the supernova remnant (SNR) will be presented below. In particular, the radiation fields in the Crab Nebula are discussed, since these are of considerable importance in the modelling of the spectrum.

### 1.1.2 Components of the Supernova Remnant SN1054

**The Crab Pulsar (PSR B0531 + 21)** has been first detected in the radio range by Staelin and Reifenstein (1968) and Comella et al. (1969). It lies at the center of the nebula and emits radiation up to GeV energies. Since its discovery, it has been intensely studied in all accessible wavelengths from radio to gamma-rays. The Crab pulsar is fastly rotating with a period of 33 ms, decreasing at a rate of  $\dot{P} = 4.21 \times 10^{-13}$  (all numbers in this subsection are taken from Hester (2008)). Therefore, the pulsar loses energy, which is referred to as the spin-down luminosity  $L_{spin}$ . On the assumption that the pulsar is a uniform sphere with a 10 km radius and a mass of  $1.4M_{\odot}$ , the spin-down luminosity of the pulsar can be written:

$$L_{spin} = 5 \times 10^{38} \text{ erg s}^{-1} \frac{I}{10^{45} \text{ g cm}^2} \left( \frac{\dot{P}}{4 \times 10^{-13}} \right) \left( \frac{P}{33 \text{ ms}} \right)^{-3}, \quad (1.1)$$

where  $I$  stands for the moment of inertia. The average spin-down luminosity over the lifetime of the nebula is estimated to be approximately  $1.2 \times 10^{39} \text{ ergs s}^{-1}$ . The pulsar releases its energy in the form of an ultrarelativistic wind as well as magnetic field. The wind is an ultrarelativistic cold plasma of electrons, positrons and possibly ions. It terminates in a shock with the ambient medium. By crossing the shock front, the particles gain energy (supposedly via the so-called *Fermi acceleration*, discussed in Section 1.3.1).

**The synchrotron nebula** It is assumed that the cold ultrarelativistic wind from the pulsar is terminating in a standing shock, which is created by the transition between the cold fast wind from the pulsar and the plasma filling the nebula. At the shock,



FIGURE 1.1: Color composite of the Crab synchrotron nebula showing a Chandra X-ray image in blue and white, a visible light image taken with HST in purple, and a Spitzer infrared image in pink. The pulsar is seen as the white blue point source at the center of the image. It can be seen that the emission is brightest near the center of the nebula close to where the high-energy electron are injected. Moving outward through the nebula, the emission becomes fainter owing to adiabatic and radiative losses as almost only low-energy electrons survive long enough to reach the edge of the nebula.

The picture is taken from <http://chandra.harvard.edu/photo/2018/crab/>.

positrons and electrons are pitch-angle isotropized and are accelerated up to  $\sim 10^4$  TeV with a power-law spectrum (see section 1.3.3). Downstream of the shock, the magnetized relativistic plasma radiates away synchrotron emission. High spatial resolution Chandra observations [Weisskopf et al. (2000)] suggest that the shock should be located at a distance of  $r_s = (0.14 \pm 0.01)$  pc from the pulsar, whereas the previously assumed value was 0.10 pc [Kennel and Coroniti (1984), Rees and Gunn (1974)]. The position of the shock front is often associated with fine structures [Rees and Gunn (1974)], the so-called *wisps* [Scargle (1969)], see also the central region of Fig. 1.1. The volume filled by the synchrotron nebula is roughly ellipsoidal, with a major axis of 4.4 pc and a minor axis of 2.9 pc. Such remnants “filled in” with radio emission and whose energy source is a pulsar, are commonly referred to as *plerions* [Weiler and Panagia (1978)]. The integrated luminosity injected by the pulsar in the nebula is about  $L_{spin} \simeq 5 \times 10^{38}$  erg s $^{-1}$  (see Eq 1.1). About 26% of the pulsar power is converted into synchrotron emission, whereas a similar fraction goes into PV (pressure-volume) power done in the filaments.

Figure 1.2 shows a color composite image of the Crab synchrotron nebula. An apparent feature is the difference in the spatial extent of the nebula when viewed at different energies. The size of the nebula shrinks with increasing energy and reflects cooling processes, since high-energy particles injected into the nebula at the wind shock undergo both synchrotron loss and adiabatic energy loss due to expansion as they move outward through the nebula. The synchrotron nebula presents an abundance of fine-scale structures that can be extremely dynamic, varying greatly on timescales of days. These

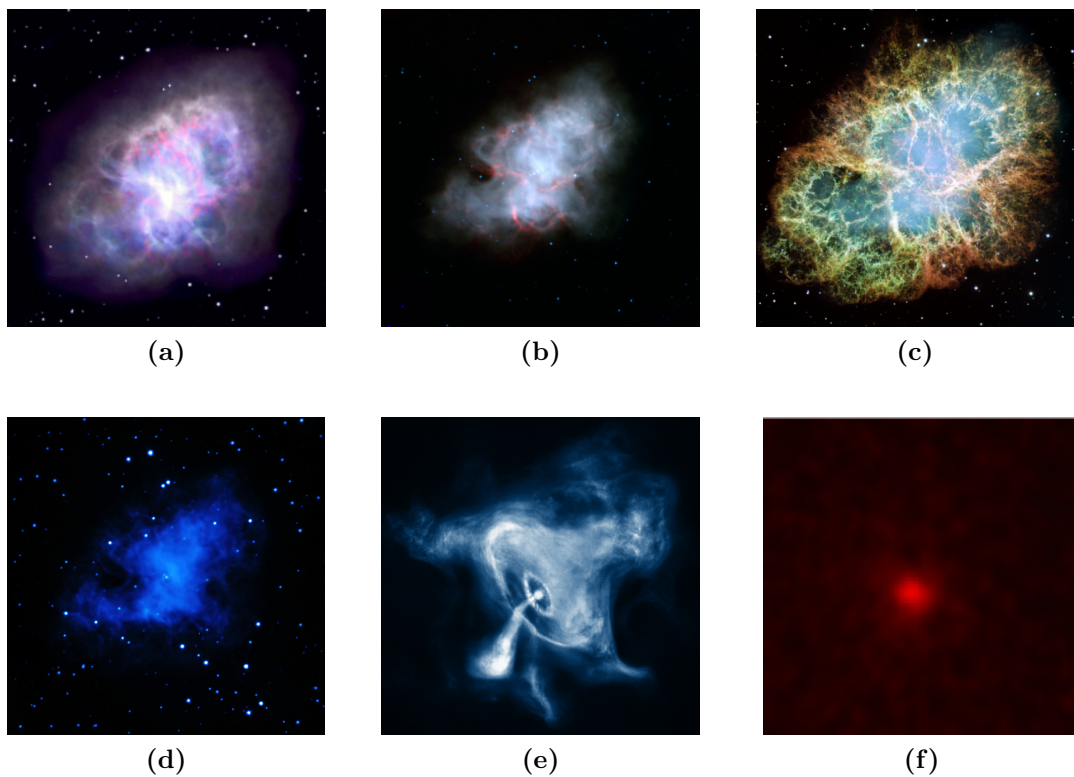


FIGURE 1.2: The Crab Nebula seen in different energy bands: (a) radio <https://public.nrao.edu/gallery/crab-nebula/> (b) infrared <https://public.nrao.edu/gallery/crab-nebula/> (c) optical <https://www.spacetelescope.org/images/heic0515a/> (d) UV [https://www.esa.int/spaceinimages/Images/2018/03/Crab\\_Nebula\\_in\\_ultraviolet](https://www.esa.int/spaceinimages/Images/2018/03/Crab_Nebula_in_ultraviolet) (e) X-ray <https://www.spacetelescope.org/images/potw1720f/> (f) gamma-rays <https://svs.gsfc.nasa.gov/cgi-bin/details.cgi?aid=10767>.

features are often referred to as *wisps*, while the term *filaments* is reserved for features seen in thermal emission from ejecta.

**The filaments and the dust** In addition to the synchrotron emission, the Crab Nebula also presents line emission in optical and thermal radiation in the infrared/sub-millimetre wavelength ranges. The line emission comes from the filaments, finger-like structures that expand and enclose the synchrotron nebula (see Fig. 1.3). Most of the emission from the filaments is the result of photoionization of the ejected material by the high-energy synchrotron radiation. The line emission has its origin in the photoionization: the high-energy synchrotron radiation ionizes the ejected material of the supernova and recombination of the ions emits light at optical and UV energies [Davidson and Fesen (1985b)]. Furthermore, submillimeter thermal emission from heated dust can be also seen in extinction against the synchrotron background. The dust appears to be concentrated mainly in regions of high gas density. The ratio of dust to gas in the

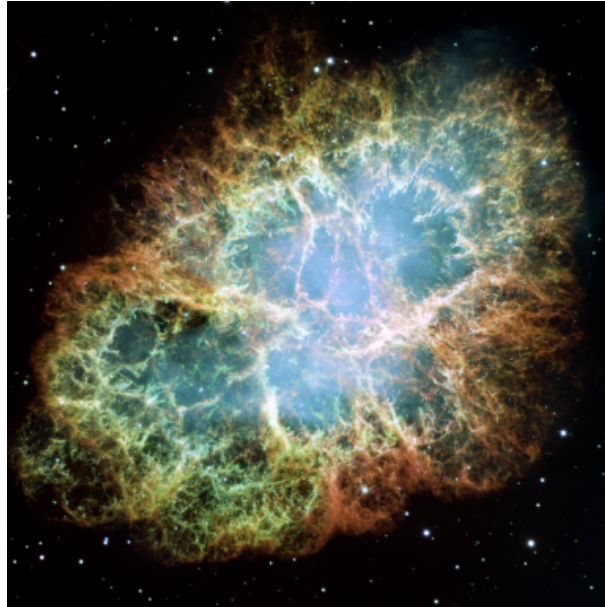


FIGURE 1.3: Overlaying images of various optical wavelength observations from HST. The filaments are formed by line emission of atoms that have been ionized by the synchrotron radiation. Shown are the forbidden lines of oxygen and silicon. [O III]  $\lambda$  5007 is shown in red, [S II]  $\lambda\lambda$  6717,6731 in green, and [O I]  $\lambda$ 6300 in blue. The synchrotron continuum filling the nebula is shown in light blue. The X-ray emitting torus from Fig. 1.1 is in the center of this picture. The image is taken from Hester (2008).

nebula vary approximately between 1.5% to 0.02%, and is up to 10% in the filaments [Hester (2008)].

**Outer shock** The Crab Nebula is believed to have been produced by a core collapse supernova. Its luminosity and light curve were consistent with those of a core-collapse supernova. The presence of an important amount of hydrogen is also a strong manifestation of this supernova type [Lundqvist et al. (1986)]. The total mass in the observed ejecta is estimated to be 2-5  $M_{\odot}$  [Davidson and Fesen (1985a), Fesen et al. (1997)], and the pulsar’s mass is thought to be of about 1.4  $M_{\odot}$  [Davidson and Fesen (1985a)]. This is much less than the total mass of 8-13  $M_{\odot}$  [Nomoto (1985), Nomoto (1987), Kitauro et al. (2006)] expected to be in the star before the explosion. The missing mass of the Crab Nebula is a long standing problem, and could possibly be explained by a freely expanding ejecta from the supernova forming an outer shell outside the visible edge of the nebula. However, neither X-ray nor radio searches have indicated any evidence such a shell. Smith (2013) discussed about the possibility that the event which gave birth to the Crab Nebula was a type of under-luminous supernova.

A sketch of the nebula with its central pulsar is shown in Figure 1.4. The term “unshocked” wind reflects the fact that particles have not yet been accelerated by crossing the shock front. In the synchrotron nebula, inelastic collisions of the electrons (and

positrons) with the surrounding photon gas occur. This can produce photons to very high energies. The theory of this process is the so-called *inverse Compton scattering* (IC scattering) and is explained in Section 3.1. [Weekes et al. \(1989\)](#) were the first to probe the IC very high energy radiation (Very High Energy, VHE) coming from the Crab Nebula.

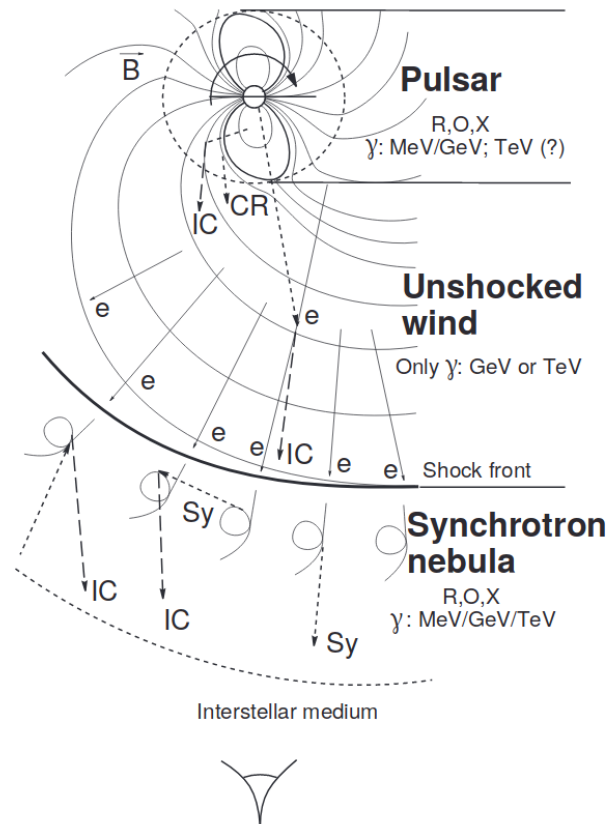


FIGURE 1.4: Sketch of the interior of the supernova remnant SN1054 showing the sites and radiation mechanisms of non thermal emission associated with rotation powered pulsars. (i) the region within the light cylinder where the magnetospheric pulsed radiation from radio to  $\gamma$ -rays is produced; (ii) the relativistic wind of positrons and electrons terminates at a shock front, where the wind of cold relativistic plasma meets the surrounding material of the supernova remnant. The wind emits GeV and TeV  $\gamma$ -rays through the IC mechanism; (iii) the surrounding synchrotron nebula which emits broadband electromagnetic radiation from radio to multi-TeV  $\gamma$ -rays through the synchrotron and IC processes. Source of illustration: [Aharonian and Bogovalov \(2003\)](#).

## 1.2 Observations from the Crab Nebula

The Crab Nebula provides exceptionally bright non-thermal emission across the entire wavelength from radio to the most energetic photons (see Fig.1.2). Its large angular size (of 7 arcmin) provides a well resolved spatial structure in the radio to X-rays, allowing studies of small-scale structural variability.

Frequency range	Instrument	Reference
Radio	Dwingeloo Radio Telescope  WMAP Planck for the HFI instrument	(Baars and Hartsuijker, 1972) Weiland et al. (2011) Planck Collaboration et al. (2016)
Submillimeter to far infrared	MPiR Bolometer on the IRTF & UH Telescope MPiR Bolometer am IRAM Telescope Iso & Scuba Spitzer Herschel WISE	Mezger et al. (1986) Bandiera et al. (2002) Green et al. (2004) Temim et al. (2006) Gomez et al. (2012) Gomez et al. (2012)
Optical Continuum and Filaments	Palomar Telescope IDS (Mount Lemmon Observatory) Palomar 5m Hale Telescope RCA CCD at the 1.2m Telescope  of the Observatoire de Haute Provence Collection of data	Kirshner (1974) Davidson (1987) Hester et al. (1990) Veron-Cetty and Woltjer (1993)  Davidson and Fesen (1985a)
near UV and UV radiation	UIT, ANS	Hennessy et al. (1992)
X-ray to $\gamma$ -ray	ROSAT HRI, BeppoSAX LECS, MECS, PDS, COMPTEL, EGRET XMM-Newton SPI on board of INTEGRAL  IBIS/ISGRI on board of INTEGRAL BATSE  Fermi/LAT	Kuiper et al. (2001) Kirsch et al. (2005) Jourdain and Roques (2008) Jourdain et al. (2008) Ling and Wheaton (2003) Buehler et al. (2012) Yeung and Horns (2019)
VHE	HEGRA  H.E.S.S. VERITAS MAGIC Tibet  HAWC	Aharonian et al. (2004a) Holler et al. (2015) Meagher (2015) Aleksić et al. (2015) Amenomori et al. (2019) Abeysekara et al. (2019)

TABLE 1.1: Compilation of observations of the Crab Nebula from radio to very high energies.

### 1.2.1 Spectral Energy Distribution

The *spectral energy distribution* (SED) can be expressed by different quantities. In this work the *spectral flux density*,  $\nu f_\nu$  and the *specific luminosity* (total energy output per frequency per time) times the frequency,  $\nu L_\nu$  are used to represent the SED. The spectral flux density  $f_\nu$  is the energy  $dE_\nu$  that crosses a unit area  $dA$  per frequency interval  $d\nu$  and time  $dt$ :

$$f_\nu = \frac{\int d\Omega E_\nu}{d\nu dA dt}. \quad (1.2)$$

It is linked to the differential number of photons arriving at the observer, per energy interval per time and per unit area ( $dN/dE$ ) by:

$$\nu f_\nu = E^2 \frac{dN}{dE}. \quad (1.3)$$

The spectral flux density  $\nu f_\nu$  is usually expressed in the units of  $\text{ergs s}^{-1} \text{cm}^{-2}$ . The luminosity per frequency interval is related to the isotropic radiation flux density by:

$$L_\nu = 4\pi d^2 f_\nu, \quad (1.4)$$

where  $d$  is the distance between the source and the observer. The specific luminosity  $L_\nu$  is usually in the units of  $\text{ergs s}^{-1} \text{Hz}^{-1}$ . The measurements range from radio to VHE emission. The data are taken from Meyer et al. (2010) and are replaced or completed by new observations of the instruments WMAP, Planck, Herschel, Fermi/LAT, MAGIC, VERITAS, Tibet, H.E.S.S. and HAWC.

The complete data set is displayed in Fig. 1.5 and is summarized in Table 1.1. Instead of single data points, XMM-Newton, IBIS/ISGRI, and SPI X-ray observations are given as power laws with envelopes, corresponding to their statistical errors. As it will be seen in the next sections, the SED for radiation processes responsible for the X-ray emission of the nebula can be determined by power laws in energy such that:

$$\frac{dN}{dE} \propto E^{-\Gamma}, \quad (1.5)$$

where  $\Gamma$  is called a photon index. In a double-logarithmic representation, the photon index of a power law equals the slope of the function, while normalization determines the intercept with the y-axis.

The synchrotron spectrum extends up to  $\sim 10^{22}$  Hz ( $\sim 10^{15}$  eV) and presents four breaks. The last break, however is rather interpreted as a cut-off. In the radio band, the spectral index is  $\alpha_r = 0.3$  and is homogeneous over the nebula [Bietenholz et al. (2004)]. In the optical, the spectrum softens to  $\alpha_o \sim 0.6$ . There is a peak in the infrared around  $10^{14}$ ,

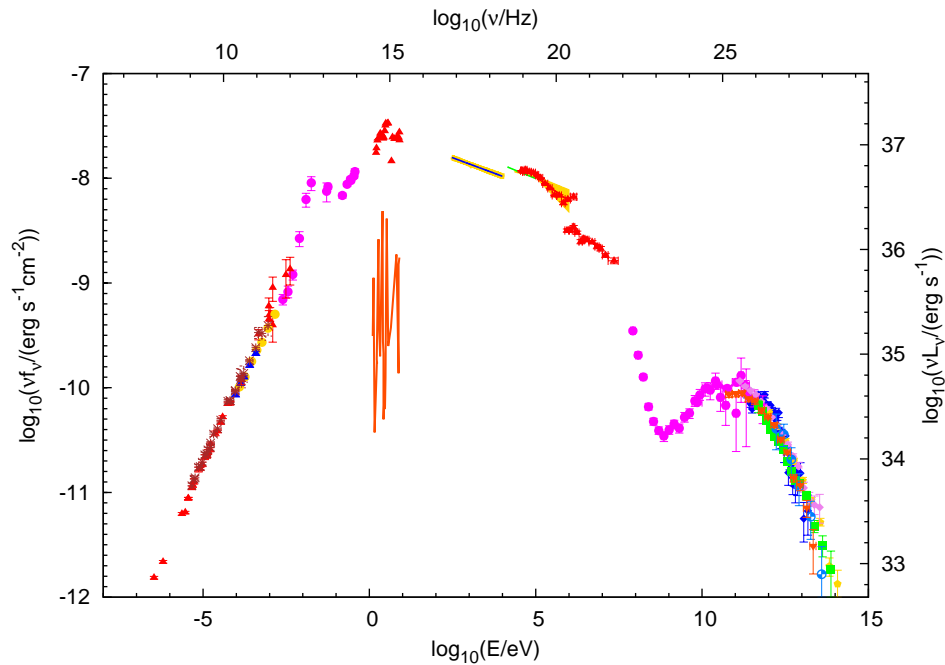


FIGURE 1.5: SED of the Crab Nebula with the different measurements used in this work. The optical line emission from thermal filaments is shown in orange line.

attributed to the change between two different electron populations (see next section for more details). The large thermal component from the filaments complicates the analysis and complicates the accurate determination of the infrared. An additional feature is present in the hard X-ray spectrum, and shows a softening at  $\sim 130$  keV [Meyer et al. (2010)]. The origine of this feature in the electron spectrum must be related to the acceleration and/or injection of the particles (see Chapter 3, subsection 3.1.2). The IC spectrum starts from  $\sim 10^{22}$  Hz to  $\sim 10^{29}$  Hz and presents a peak around  $10^{25} - 10^{26}$  Hz. More details about the IC spectrum are given in Chapter 2.

Since the work of Meyer et al. (2010), roughly nine more years of Fermi-LAT observations are available. The statistical uncertainty on the flux above 100 GeV has been reduced by a factor of three. The updated instrumental response function of Fermi-LAT extends the high energy reach from formerly 300 GeV to 500 GeV. The systematic uncertainties have been (greatly) reduced from previously  $\Delta E/E = \begin{smallmatrix} +5\% \\ -10\% \end{smallmatrix}$  [see e.g. Abdo et al. (2009)] to  $\Delta E/E = \begin{smallmatrix} +2\% \\ -5\% \end{smallmatrix}$  [Ackermann et al. (2012)].

Yeung and Horns (2019) analysed the LAT data accumulated over  $\sim 9.1$  years with a properly refined model for the Crab pulsar's spectrum. They obtain a  $> 5$  GeV spectrum of FL8Y J0534.5+2201i (the PWN component) which essentially matches the off-pulse spectrum reported by Buehler et al. (2012). The spectral model assigned to the Crab

pulsar is not expected to introduce any obvious bias in their analysis for energies above 20 GeV, due to its minor contribution of flux.

The MAGIC collaboration has published an updated energy spectrum of the Crab nebula with improved overlap and reduced uncertainties in the low energy regime below 100 GeV [Aleksić et al. (2015)]. The MAGIC measurements flux from the Crab Nebula, spans for the first time from 50 GeV to 30 TeV.

Very recently, the HAWC Collaboration has presented measurements which are the highest-energy observation of a gamma-ray source to date [Abeysekara et al. (2019)]. In their analysis, they use two independent energy-estimation methods which take into account extensive air shower variables such as the core position, shower angle, and shower lateral energy distribution. Whereas their previously published HAWC energy spectrum roughly estimated the shower energy with only the number of photomultipliers triggered. The new methodology they have been using yields to a better energy resolution over the previous analysis and extends HAWC's capacity to accurately measure gamma-ray energies well beyond 100 TeV.

In its Second Planck Catalogue of Compact Sources, the Planck Collaboration has recently published the total intensity and polarized flux densities for the Crab Nebula measured from the Planck full-mission maps at 30 to 353 GHz [Planck Collaboration et al. (2016)]. The improvements in the data processing and calibration of the frequency channel maps supersedes the previous versions of the catalogue. The Second Planck Catalogue of Compact Sources is a list of discrete objects detected in single-frequency maps and has been produced using the Planck full mission data, superseding previous versions. The catalogue records sources detected in total intensity in each of its nine frequency bands between 30 and 857 GHz and polarization measurements at the positions of these sources for seven of the frequencies between 30 and 353 GHz.

Weiland et al. (2011) present WMAP seven-year observations of bright sources. The Crab Nebula (and nine other objects) are studied in five frequency bands (23-94 GHz), with an absolute calibration uncertainty of 0.2%.

Recently, the Tibet collaboration has found an upper limit above 140 TeV, after they searched for continuous gamma-ray emission from the Crab Nebula above  $\sim 100$  TeV. They have been using the data collected by the Tibet AS array and the 100 m<sup>2</sup> muon detector constructed under the Tibet AS array.

The High Energy Stereoscopic System (H.E.S.S.) collaboration has presented their results of H.E.S.S. phase II observations of the Crab Nebula. The H.E.S.S. phase I instrument was an array of four 100 m<sup>2</sup> mirror area Imaging Atmospheric Cherenkov Telescopes (IACTs) that has successfully mapped the sky at photon energies above 100

GeV. The construction of H.E.S.S. II started in 2005 and consists of the addition of a 600  $m^2$  telescope to the centre of the existing array, which can be operated either in stand alone mode or jointly with the four other telescopes. The large telescope lowers the energy threshold for gamma-ray observations to several tens of GeV, making the array sensitive at energies where the Fermi-LAT instrument statistics becomes poorer.

Finally, the VERITAS collaboration reported on the results of six years of Crab observations with VERITAS comprising 115 hours of data taken between 2007 and 2013.

### 1.2.2 Morphology

The measurements of the size of the Crab Nebula seen in different energy bands are presented in Chapter 2, subsubsec. 2.2.2, and Chapter 3, sec. 3.2.

## 1.3 Modelling Pulsar Wind Nebulae

Pulsar Wind Nebulae (PWNe) are usually described as expanding bubbles of relativistic plasma that form when the pulsar wind is confined by the SNR or the interstellar medium (ISM). Modelling of PWNe requires the description of an acceleration mechanism responsible for producing the observed non-thermal particles distribution function, and a dynamical model describing the advection and evolution of the flow. Relativistic particles within the nebula are thought to be accelerated to a power-law distribution either via a Fermi-like acceleration mechanism occurring at the termination shock (TS) [Arons and Tavani (1994) and references therein] or via shock-driven reconnection in a striped wind [Pétri and Lyubarsky (2007), Sironi and Spitkovsky (2011)]. Lyutikov et al. (2019) outlined a model of the Crab Pulsar Wind Nebula with two different populations of synchrotron emitting particles, originating from Fermi-I acceleration for the first one and from acceleration at reconnection layers in the bulk of the turbulent Nebula for the second one. The downstream flow interacts with the surrounding magnetic and photon fields, creating the PWN. Although the acceleration problem is still unsolved, there is however a general agreement that X-ray emitting particles are accelerated at the wind termination shock, while the origin of radio emitting ones remains currently debated [Lyubarsky (2005)].

The non-thermal radiation of the Crab Nebula from radiowavelengths to hard X-rays, is strongly linearly polarized and is therefore interpreted as synchrotron emission from relativistic electrons being accelerated up to  $10^{16}$  eV energies [Kennel and Coroniti (1984), de Jager and Harding (1992)]. Whereas the TeV gamma-ray emission from

the PWNe is interpreted as being due to synchrotron self-Compton (SSC) process, according to which relativistic leptons inside the nebula produce “soft” synchrotron photons. These seed photons are later up-scattered by the same leptons, to gamma-ray energies via inverse Compton (IC) process. Photon fields of different nature are also up-scattered by these leptons to gamma-ray energies: the cosmic microwave background radiation (CMB) and infrared or optical radiation.

### 1.3.1 Radiative models of PWNe

Two comprehensive types of PWN models have been used to describe the observed broad band emission from the Crab Nebula. There are the models which consider the magnetohydrodynamics (MHD) solution of the downstream flow [Rees and Gunn (1974), Kennel and Coroniti (1984), de Jager and Harding (1992), Atoyan and Aharonian (1996a), de Jager et al. (1996), Del Zanna et al. (2006), Volpi et al. (2008), Meyer et al. (2010)], and the more simple “single-zone” models, either with a constant and isotropic magnetic field in a static framework [Hillas et al. (1998), Aharonian et al. (2004b), Meyer et al. (2010)] or investigating the temporal evolution of the PWN [Torres et al. (2014), Bednarek and Bartosik (2003), Martín et al. (2012)]. Furthermore, these different models can also present a multidimensional description of the Crab Nebula [Porth et al. (2014), Del Zanna et al. (2006)]. While ions may be present in the pulsar wind [e.g. Spitkovsky and Arons (2004)], most models assume that the relativistic electrons and positrons dominate the particles injected into the PWN. Table 1.2 gives a summary of the models introduced in that section and compare their different features.

**Single-zone Models** simplify the description of the PWN by considering it as an uniform object with a given size, and being eventually time-dependant. The basic assumptions underlying this approach are [Reynolds and Chevalier (1984)]:

- the PWN is powered by the rotational energy of the pulsar,
- the bulk of the pulsar’s rotational energy is injected into the PWN in the form of relativistic particles and magnetized plasma,
- the PWN is a spherical and homogeneous bubble filling the SNR produced by the progenitor SN explosion.

This last feature differentiates the one-zone models from the more complex multidimensional models. Although they all differ from each other, the one-zone models all include:

- the injection of particles and magnetic fields into the PWN,
- the evolution of the particles and magnetic field inside the PWN,
- and the interaction between the PWN and its surrounding SNR.

The global observed properties of these systems are fairly well reproduced, and they also recover satisfactorily the duration and timescale of the various phases of interaction with the SNR. However, more precise models need to be used to describe the high-energy X-ray properties, that depend on the post shock flow. However, the lack of scope of measurements for most PWNe is such that, one-zone models are often the only reasonable approach for the description of these objects. Furthermore, they also constitute a good base for more accurate, multidimensional analysis.

Multidimensional models for PWNe were developed mostly in the past ten years, and were mainly motivated by high-resolution optical and X-ray images from HST, CHANDRA and XMM-Newton. While these multidimensional models, by necessity, assumed steady-state conditions [Kennel and Coroniti (1984)], the one zone models incorporated both the evolution of the pulsar and the SNR. Time-dependent models solve the diffusion-loss equation numerically without any approximation, taking into account synchrotron, IC and Bremsstrahlung energy losses. The Klein-Nishina cross section is used to describe the IC losses. Particles escaping the nebula due to Bohm diffusion are also considered. In a study of Torres et al. (2013a), the 1D uniform magnetic field is modeled by solving the magnetic field energy conservation, including its work on the environment.

**MHD models** are motivated by a more physical approach, which is to describe the magnetohydrodynamic (MHD) plasma in the (assumed) spherical nebula in which the evolution of the magnetic field and the particles in the nebula can be calculated. Firstly developed by Rees and Gunn (1974), Kennel and Coroniti (1984) were being able to predict the synchrotron emission of the nebula. Later, [Atoyan and Aharonian (1996a)] extended it to describe the high-energy part of the spectrum. In the MHD description, the magnetic field can be determined as a function of the distance to the shock front at which the relativistic particle wind of the pulsar is terminated and the particles are accelerated. The MHD calculation requires two additional parameters in addition to the number of particles  $n(\gamma)$  per unit volume and energy interval  $[\gamma, \gamma + d\gamma]$ : the distance of the shock front from the center,  $r_s$  and the magnetization parameter,  $\sigma$ , which is equal to the ratio of Poynting flux to particle energy flux. Rees and Gunn (1974) assumed a shock distance of  $r_s = 0.10$  pc, whereas Chandra observations indicate a distance from the shock front  $r_s = (0.14 \pm 0.01)$  pc. Meyer et al. (2010), for a value of  $\sigma = 0.0045$  and the most recent value of  $r_s$ , have attempted to adapt their model to the compilation of

data based on the work of [Atoyan and Aharonian \(1996a\)](#). For the assumed value of  $\sigma$ , the calculated value of the magnetic field agrees well with the spatially averaged field of  $160 \mu\text{G}$ . However, [Meyer et al. \(2010\)](#) can not satisfactorily describe the observed spectrum, the data is instead better described by the simplified *constant B-field model*. It has the advantage that the calculation requires relatively little computation time but with more free parameters. First introduced by [Meyer et al. \(2010\)](#), it follows the approach suggested by [Hillas et al. \(1998\)](#) and [Aharonian et al. \(2004b\)](#). The crab nebula is assumed to be filled with an homogeneous and constant magnetic field and two distinct electron populations. Following [Hillas et al. \(1998\)](#), the spatial distributions of both the seed photons and pulsar wind electrons are described by Gaussian distributions in distance to the nebula's center, whereas the relic electrons are uniformly distributed throughout nebula.

However, the MAGIC collaboration has published an updated energy spectrum of the Crab Nebula with improved overlap and reduced uncertainties below 100 GeV [[Aleksić et al. \(2015\)](#)]. The broad band energy spectrum is recalculated based on the work of [Meyer et al. \(2010\)](#) for the MHD and constant  $B$ -field model, and [Torres et al. \(2013b\)](#), [Torres et al. \(2013a\)](#), [Martín et al. \(2012\)](#) for a a time-dependent, leptonic spectral model. [[Aleksić et al. \(2015\)](#)] show that the shape of the spectrum is not well described anymore by the constant  $B$ -field model, as well as the MHD model. The time-dependant model describes well the SED but does not treats the morphology of the Crab Nebula at different frequencies.

Therefore, theoretical refinements on the Crab Nebula modelling need to be done to simultaneously fit the observed morphology and the spectral energy distribution. The broad-band IC spectrum can also be used to investigate the spatial structure of the magnetic field. More realistic models have failed so far to describe satisfactorily the energy spectrum of the Crab Nebula. In this work, the constant  $B$ -field model is reexamined. The spatial distribution of the photons coming from the thermal emission is included for the first time in detail. The spatial overlap between the seed photons and the electrons are calculated with a spatial overlap of the distributions. The electron distribution is inferred from observations. The magnetic field is left free. It is first taken as constant (and static), and is further considered with a more realistic approach. The particle losses are considered with a phenomenological approach.

### 1.3.2 Acceleration in supernovae remnants (SNRs)

It was generally assumed that the particle acceleration in the Crab Nebula was taking place at the wind termination shock, supposedly via the *Fermi first-order* mechanism

Model	D	B	Radiation	particle transport	temporal evolution
Single-zone	1	fixed	fixed	none	none
<a href="#">Rees and Gunn (1974)</a>	1	MHD	Sync	MHD	none
<a href="#">Kennel and Coroniti (1984)</a>	1	MHD	Sync	MHD	none
<a href="#">de Jager and Harding (1992)</a>	1	MHD	Sync+IC	MHD	none
<a href="#">Atoyan and Aharonian (1996a)</a>	1	MHD	Sync+IC <sub>CMB</sub>	MHD	none
<a href="#">Torres et al. (2013b)</a>	1	fixed	Sync+IC	convection +diffusion	yes
<a href="#">Porth et al. (2014)</a>	2,3	MHD	Sync	MHD	none
<a href="#">Del Zanna et al. (2006)</a>	2D (axisymmetric)	MHD	Sync	convection	none
our model	1	free	Obs.	Phen.	none

TABLE 1.2: Different models used for modelling the Crab Nebula. **D** represents the number of spatial dimension used in the model. **B** indicates the treatment of the magnetic field. “Obs.,” “Sync.” and “Phen.” stands for “Observations”, “Synchrotron” and “Phenomenology” respectively.

[[Rees and Gunn \(1974\)](#), [Kennel and Coroniti \(1984\)](#)]. Fermi acceleration is one of the most widely discussed theory explaining the particle acceleration at shock fronts. Fermi’s original idea was that charged particles could be accelerated through encounters with irregularities in the Galactic field. Fermi demonstrated that the random movement of these “magnetic clouds” was responsible for particles to be statistically accelerated by scattering. The resulting net acceleration occurs at a speed which depends on whether the scattering centers move in a random or regular trend, leading to two distinct Fermi acceleration processes: the *first-order* and *second-order* processes. References to this section are based on the work of [Longair \(2011\)](#) and [Ferrand \(2008\)](#).

### Fermi acceleration

Imagine a cloud moving at a speed  $\mathbf{V}$  along the vector normal to the cloud surface, with the corresponding Lorentz factor  $\gamma(V) = (1 - V^2/c^2)^{-1/2}$ . The particle enters the cloud with an angle  $\theta$  and with an initial momentum  $p_{in} \cos \theta$ . The recoil of the cloud due to the encounter with the particle is negligible. In the cloud frame, the energy  $E'_{in}$  and impulsion  $\mathbf{p}'_{in}$  of the particle are given by the Lorentz transforms:

$$\begin{cases} E'_{in} = \gamma(E_{in} - V p_{in\parallel}) \\ p'_{in\parallel} = \gamma(p_{in\parallel} - \frac{V}{c^2} E_{in}), \end{cases} \quad (1.6)$$

where  $p_{\parallel}$  denotes the component of  $\mathbf{p}$  along  $\mathbf{V}$ . From energy and momentum conservation, it follows that the energy before the impact is equal to the energy after the impact  $E'_{out} = E'_{in}$ , but the parallel component of the momentum changes its sign  $p'_{out\parallel} = -p'_{in\parallel}$ .

Another Lorentz transformation into the laboratory system after scattering yields the result:

$$E_{out} = \gamma(E'_{out} + Vp'_{out\parallel}). \quad (1.7)$$

Combining equations 1.6 and 1.7, gives the energy change  $\Delta E = E_{out} - E_{in}$  in second order in  $V/c$ :

$$\frac{\Delta E}{E} = 2\gamma^2 \frac{(\mathbf{V} - \mathbf{v}) \cdot V}{c^2} = \frac{2vV \cos \theta}{c^2} + 2 \left( \frac{V}{c} \right)^2, \quad (1.8)$$

where  $v$  is the particle's velocity. Through a collision with a magnetic cloud, a particle changes its energy:

- for head-on collisions ( $\mathbf{v} \cdot \mathbf{V} < 0$ ), the particle gains energy ( $\Delta E > 0$ )
- for overtaking collisions ( $\mathbf{v} \cdot \mathbf{V} > 0$ ), the particle loses energy ( $\Delta E < 0$ )

For relativistic particles with  $v \simeq c$ , the probability of a collision is given by  $\gamma_V(1 + (V/c) \cos \theta)$  [Longair (2011)]. If the clouds move randomly, one can average over all possible angles  $\theta \in [0; \pi]$ . With  $x = \cos \theta$  one obtains

$$\langle 2\beta_V \cos \theta \rangle = 2 \left( \frac{V}{c} \right) \frac{\int_{-1}^1 x[1 + (V/c)x]dx}{\int_{-1}^1 [1 + (V/c)x]dx} = \frac{2}{3} \left( \frac{V}{c} \right)^2. \quad (1.9)$$

Thus, the total energy gain is given by  $\langle \Delta E/E \rangle = 8/3(V/c)^2$ , and is therefore of second order in  $V/c$ . For this reason, this process is referred as *second-order* Fermi acceleration. The particles are accelerated during a characteristic time  $\tau_{acc}$  while they are in the acceleration region. The time  $\tau_{acc}$  is thus associated with the probability  $P$  that the particles remain in the acceleration region after scattering. If, in addition, the mean energy of a particle after scattering is given by:  $E = \alpha E_0$ , with  $\alpha \propto \Delta E$ , it can be seen that the resulting spectrum follows a power law. After  $k$  collisions there are still  $N_{el} = N_0 P^k$  particles with energies  $E = E_0 \alpha^k$  in the acceleration region. Eliminating  $k$  supplies:

$$\frac{\ln(N_{el}/N_0)}{\ln(E/E_0)} = \frac{\ln P}{\ln \alpha} \Leftrightarrow N_{el} = N_0 \left( \frac{E}{E_0} \right)^{\ln P / \ln \alpha}. \quad (1.10)$$

Accordingly, the particle distribution in the energy follows the function

$$\frac{dN_{el}}{dE} \propto E^{-1 + \ln P / \ln \alpha}. \quad (1.11)$$

The great merit of the Fermi mechanism is that it naturally produces a power law spectrum, in accordance with what is observed in astrophysical sources or in interstellar medium (ISM). However, two major issues remain. First, no prediction is made about the values of  $\kappa$  or  $P$ . Second, especially for  $V \ll c$ , the acceleration is very inefficient.

Looking at the equation 1.8, it is clear that for frontal collisions, the energy gain is linear in  $V/c$  (also called *first-order Fermi acceleration*). Thus, such collisions would be more effective to achieve faster high accelerations. This scenario is actually realized when accelerating to shock fronts.

### Acceleration in strong shock waves

Shocks are omnipresent in the universe: they are observed at all scales, and in all kind of environments. A shock wave is created when a disturbance is propagating in a medium faster than the speed of sound in that medium. A shock front appears, at which the physical quantities are discontinuous. The strength of the shock is given by the ratio of its proper speed  $V_s$  over the local sound speed  $c_s$ :

$$M_s = \frac{V_s}{c_s}, \quad (1.12)$$

called the *Mach number*. A very simple sketch of a non-relativistic planar shock is given in figure 1.6a. The shock is represented as a discontinuity, separating upstream (marked with the index “-”) and downstream (noted with the index “+”) states. The velocities are measured here in the shock rest frame, so that the upstream flow falls on the shock at a velocity  $v_- = V_s$ , and leaves the shock with a downstream velocity  $v_+$ . Thus, the corresponding Lorentz factor  $\Gamma_{\pm} = (1 - v_{\pm}^2/c^2)^{-1/2}$  can be defined. The upstream and downstream states are linked by the jump conditions (so called *Rankine-Hugoniot* relations) and express simply the continuity of the mass, momentum and energy fluxes at the shock interface (in its rest frame):

$$r = \frac{v_-}{v_+} = \frac{\rho_+}{\rho_-} \longrightarrow \frac{\gamma + 1}{\gamma - 1}, \quad (1.13)$$

$$\frac{P_+}{P_-} \longrightarrow \frac{2\gamma}{\gamma + 1} M_s^2, \quad (1.14)$$

$$\frac{T_+}{T_-} \longrightarrow \frac{2\gamma(\gamma - 1)}{(\gamma + 1)^2} M_s^2, \quad (1.15)$$

where  $r$  is the compression ratio of the shock. The formulas on the right are obtained in the limit of strong shocks ( $M_s \gg 1$ ). For a usual polytropic index  $\gamma = 5/3$ , strong shocks have a compression ratio of  $r = 4$  (and the downstream pressure and temperature can grow without limits). Both the upstream and the downstream medium see the opposite side coming against them and at the same speed:

$$\Delta V = \frac{r - 1}{r} V_s \left( = \frac{3}{4} V_s \text{ if } r = 4 \right). \quad (1.16)$$

The different situations are shown in Figure B.3. The figure B.3b shows the rest system of the plasma upstream. According to equation 1.16, the plasma flows downstream from the shock front, with the velocity  $v'_+ = -3/4v_-$  in the upstream rest frame. Similarly, the upstream plasma arrives in the direction of the shock front (see Fig. B.3a), with the velocity  $v'_- = 3/4v_-$  in the downstream rest frame. Shock wave provides a configuration in which only face-on encounters occur. Therefore, when a high energy particle crosses the shock, it gains a small increase in energy-in the non-relativistic case- of order  $\Delta E/E \sim V_s/c = v_-/c$  (see Eq. 1.8). A precise calculation shows that  $\langle \Delta E/E \rangle = (2/3)(v_-/c)$  applies on average. Due to their diffusion via magnetic turbulences, the cosmic-rays are pitch-angle isotropized on each side of the shock. Since the same situation prevails on both sides of the shock, a particle for the round trip wins the energy  $\langle \Delta E/E \rangle = (4/3)(v_-/c)$ . Therefore,

$$\alpha = \frac{E}{E_0} = 1 + \frac{4V}{3c}. \quad (1.17)$$

To calculate the escape probability  $P$ , one can follow the argument of Bell (1978). According to classical kinetic theory, the rate of particles crossing the shock from either direction is  $(1/4)nc$ , where  $n$  is the particles number density. The upstream particles are swept into the shock, so that particle losses can be neglected. However, downstream of the shock, particles are swept away from the shock at a rate of  $nv'_- = (1/4)nV_s$ . The fraction of particles lost per unit time is then  $1/4nV_s/1/4nc = V_s/c$ , such that the fraction of particles remaining after one cycle is  $P = 1 - V_s/c$ . The exponents of Equation 1.11 therefore translates as:

$$-1 + \frac{\ln P}{\ln \kappa} = -1 + \frac{\ln(1 - v_-/c)}{\ln(1 + v_-/c)} \approx -1 - 1 = -2, \quad (1.18)$$

with the use of the serie expansion of  $\ln(1 + x)$ . However, the termination shock in the Crab Nebula is a relativistic shock front. In this case, the assumption of an isotropic pitch-angle distribution does not hold anymore, since the Lorentz transformation from one rest system to the other then greatly alters the angular distribution. Achterberg et al. (2001b) for example, have shown that in the case of ultrarelativistic shocks, particles with an angle  $\theta_c = 1/\Gamma_s$  (with  $\Gamma_s$  the Lorentz factor of the shock) in the rest system of the upstream plasma, are scattered upwards across the shock current, and the scattering process changes  $\theta_c$  only by  $\Delta\theta \approx \theta_c$ , before the particles cross the shock again.

The energy gain is, in this case, dependent on the pitch angle distribution, and for the momentum distribution of the particles a diffusion equation has to be solved. For a pitch-angle  $\theta$ , the diffusion coefficient  $D_{xx}$  (usually measured in area per time), with  $x = \cos \theta$  is dependent on its distribution. For an isotropic distribution,  $D_{xx} \propto 1 - x^2$ . The particles are scattered by wave irregularities. Considering the wavenumber  $k$ , its

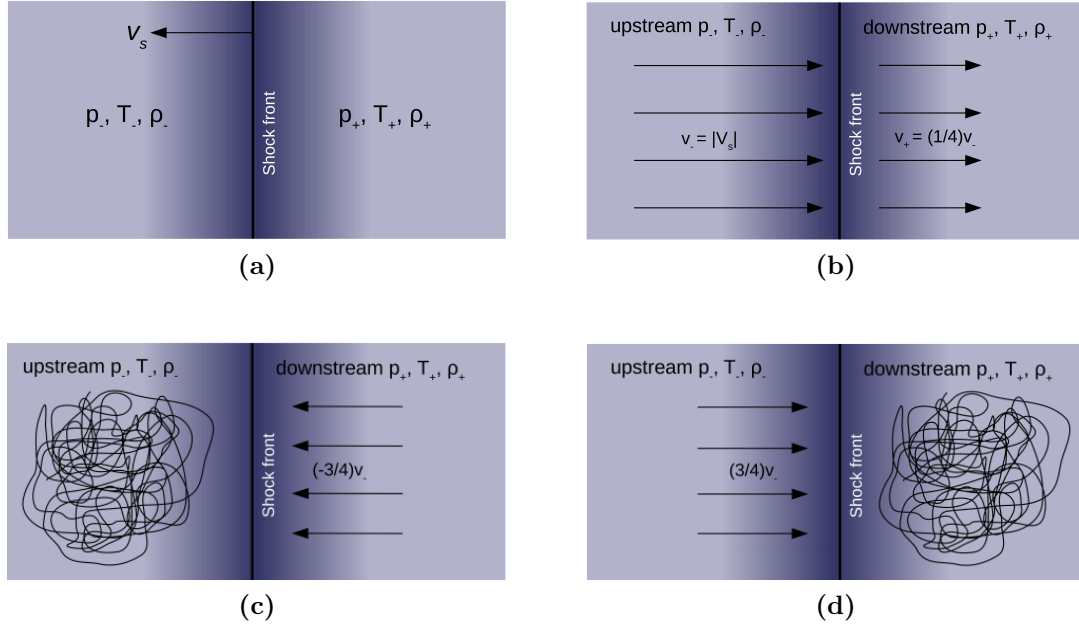


FIGURE 1.6: **(a)** A planar shock wave propagating at a supersonic velocity,  $V_s$  through a stationary medium with density  $\rho_1$ , pressure  $p_1$  and temperature  $T_1$  **(b)** rest system of the shock wave. In the non-relativistic case, it follows from the shock conditions that, for a strong shock, the velocities of the plasmas upstream and downstream are linked by  $v_+ = 1/4v_-$  **(c)** rest system of the upstream plasma. The particles velocity is isotropized and the plasma downstream flows toward the shock at the speed of  $3/4v_-$  **(d)** rest system of the plasma downstream. It shows the same situation as in (b). The figures are based on Longair (2011).

component parallel to the undisturbed magnetic field is given by  $k_{\parallel} = qB/(p|x|)$ , with  $p$  the momentum of the particle of charge  $q$ , the diffusion coefficient is of the form  $D_{xx} \propto k_{\parallel}\varepsilon(k_{\parallel})$  [Heavens and Drury (1988)]. In the case of a plot of the form  $\varepsilon(k_{\parallel}) \propto k_{\parallel}^{5/3}$  one speaks of a Kolmogorov spectrum. By solving numerical solutions of the diffusion equation, Ballard and Heavens (1992) for example, find spectral indices between 2.0 and 2.4. Achterberg et al. (2001a) find in their simulations consistent values between 2.2 and 2.3.

## Particles cooling

During injection of high energy electrons into the nebula, energy is lost through various processes. The evolution of the number of electron,  $N_{el}$ , is described by a diffusion energy loss equation [Longair (2011), Manolakou et al. (2007)]:

$$\frac{\partial N_{el}(\gamma, t)}{\partial t} - \frac{\partial}{\partial \gamma} [\dot{\gamma}(\gamma)N_{el}(\gamma, t)] - \nu_{esc}(\gamma)N(\gamma, t) = Q(\gamma, t). \quad (1.19)$$

The function  $Q$  describes the rate at which the electrons are injected in the nebula, and  $\nu_{esc}(\gamma)dt$  is the probability for each electron of escaping the source by diffusion in a time interval  $dt$ . The number of particles per unit time that are cooling with the Lorentz factor  $\gamma$  is given by  $[\dot{\gamma}(\gamma)N_{el}(\gamma, t)]$ . Each electron in the source loses energy, according to  $\partial\gamma/\partial t = \dot{\gamma}$ , that can be due to several contributions [Longair (2011), Chapter 19]:

- *ionization losses*: due to the ionization (collisions) of the surrounding medium, electrons lose energy with  $\dot{\gamma} \propto N$ , with  $N$  the number density of the hydrogen atoms.
- *Bremsstrahlung*: the electrons lose energy due to the deceleration by electrostatic fields of ion and atomic nuclei, with  $\dot{\gamma} \propto N$ .
- *Adiabatic losses*: in an expanding medium, the electrons lose energy through the outward convection. If the change in the volume of the nebula is determined by the velocity field  $\mathbf{v}(\mathbf{r})$ , the energy loss is given by  $\dot{\gamma} = (1/3)(\nabla \cdot \mathbf{v})\gamma$  [Longair (2011), Chapter 11].
- *Synchrotron losses* by emitting synchrotron radiation, the electrons lose their energy according to equation 1.28.
- *Inverse Compton scattering*: inverse Compton scattering causes an energy loss which is described by Equation 1.41.

Strictly speaking, the equation of diffusion 1.19 is only valid for a steady loss of energy and thus is not valid in the extreme Klein-Nishina case. For a homogeneous source, the diffusion can be neglected. Furthermore, if the energy losses and the escape time are independent of time, the diffusion equation can be solved by the Laplace transforms [Manolakou et al. (2007)] and references there). Let us consider the case where the injection rate follows a power law (as in the case of Fermi acceleration):  $Q(\gamma, t) = Q_0\gamma^{-p}$ , and  $Q$  is non null only within a range such that:

$$\begin{cases} Q = Q_0\gamma^{-p} & \text{for } \gamma_{min} \leq \gamma \leq \gamma_{max} \\ 0 & \text{else.} \end{cases}$$

In the case where the radiative cooling is only due to synchrotron losses :  $\dot{\gamma} = b_s\gamma^2$ , and no escaping term is present ( $\nu_{esc} = 0$ ), the solution of equation 1.19 is [Manolakou et al. (2007)]:

$$N(\gamma, t) = \frac{Q_0\gamma^{-p}}{(p-1)b_s\gamma} \cdot \begin{cases} [1 - (1 - b_s\gamma t)^{p-1}] & \text{for } 0 \leq b_s\gamma t \leq 1, \\ 1 & \text{for } b_s\gamma t > 1. \end{cases} \quad (1.20)$$

Equation 1.3.2 implies that the electron spectrum steepens from  $\gamma^{-S}$  for  $b_s\gamma t \ll 1$  to  $\gamma^{-(S+1)}$  for  $b_s\gamma t \simeq 1$ , with a spectral break at  $\gamma \approx 1/b_s t$ . From Table 1.3, it can be seen that the synchrotron spectrum will soften from  $\nu L_\nu \propto \nu^{-\delta}$  to  $\nu L_\nu \propto \nu^{-(\delta+1)}$ . That effect is called the *spectral ageing* effect, which is due to the short synchrotron-emitting lifetime of particles with higher Lorentz factor. It depends on the particle energy and the strength of the magnetic field. The cooling break in the synchrotron spectrum is expressed by [Chevalier (2000)]:

$$\nu_c(\text{GHz}) = 1.187 B^{-3}(\text{G})t^{-2}(\text{yr}), \quad (1.21)$$

where  $\nu_c$  is the cooling break frequency,  $B$  the magnetic field and  $t$  the age of the nebula.

In summary, Fermi acceleration at shock fronts causes power laws for the spectral distribution of the electrons whose spectral indices are typically in the range between 2.0 and 2.4. If cooling effects are also taken into consideration and if synchrotron cooling dominates, the spectral index is around 1. Further variations may also occur as the particles move in turbulent plasmas.

### 1.3.3 Relevant radiation processes

Electromagnetic radiation can be either thermal or non thermal radiation, depending on the energy distribution of the light emitting particles. Thermal light sources are usually in thermodynamical equilibrium, so the light emitting particles produce a Maxwellian distribution. The radiation is due to energy transitions of bound electrons, and for multiple transitions, this gives a blackbody spectrum. While this process is well understood, some of the more unusual objects in space such as supernovae, pulsars, radio galaxies, etc produce a type of emission that can not be described as “blackbody radiation” or “thermal radiation”. Non-thermal radiation is produced by charged particles interacting with electromagnetic fields, i.e. by the synchrotron and inverse Compton processes. The relativistic electrons in nearly all synchrotron sources have power-law energy distributions, so they are not in local thermodynamic equilibrium. Consequently, synchrotron sources are often called “non-thermal” sources. However, a synchrotron source with a relativistic Maxwellian electron-energy distribution would be a thermal source, so “synchrotron” and “non-thermal” are not completely synonymous.

## Synchrotron emission

Let us consider an electron of energy  $E = \gamma mc^2$ , with velocity  $v$  in a magnetic field spiraling along the magnetic field lines with an angle  $\theta = \widehat{(\mathbf{B}, \mathbf{v})}$  (usually referred to as the *pitch angle*), and with the angular frequency:

$$\Omega = \frac{eB}{\gamma mc}, \quad (1.22)$$

with  $B = \|\mathbf{B}\|$ . Any accelerated charged particle emits electromagnetic radiation, which is called *cyclotron* radiation when  $v \ll c$ , and *synchrotron* radiation for relativistic particles with  $v \sim c$ . In the case of synchrotron radiation, two relativistic effects are affecting the Larmor's equations: the length contraction and the Doppler shifting.

**Emitted power of an electron** To calculate the total synchrotron losses, let us consider the rest frame of the particle (in that frame,  $v$  is zero but the acceleration is not). The *emitted* power  $P'_e = dE'/dt'$  is a Lorentz invariant:<sup>2</sup>

$$P_e = P'_e = \frac{2e^2}{3c^3} a'^2 = \frac{2e^2}{3c^3} [a'^2_{\perp} + a'^2_{\parallel}], \quad (1.23)$$

with the electric charge being also a relativistic invariant  $e = e'$ . By applying the Lorentz transform to the acceleration component  $a'_{\perp}$  and  $a'_{\parallel}$ , one obtains for the generalization of the Larmor formula:

$$P_e = P'_e = \frac{2e^2}{3c^3} [a'^2_{\perp} + a'^2_{\parallel}] = \gamma^4 [\gamma^2 a^2_{\perp} + a^2_{\parallel}]. \quad (1.24)$$

The term  $\gamma^2 a^2_{\perp}$  is negligible since for relativistic particles  $v \sim c$ , so the acceleration in the same direction of the velocity is very small. A particle moving in a magnetic field will have a helical trajectory of radius  $r_L$  (the Larmor radius). In the absence of electric field, the only acting force is the (relativistic) Lorentz force:

$$\mathbf{F}_L = \frac{d}{dt}(\gamma m \mathbf{v}) = \frac{e}{c} \mathbf{v} \times \mathbf{B}. \quad (1.25)$$

The parallel and perpendicular components are given by:

$$\begin{aligned} F_{L\parallel} &= \gamma m \frac{dv_{\parallel}}{dt} \longrightarrow a_{\parallel} = 0, \\ F_{L\perp} &= \gamma m \frac{dv_{\perp}}{dt} = e \frac{v_{\perp}}{c} B \longrightarrow a_{\perp} = \frac{evB \sin \theta}{\gamma mc}. \end{aligned} \quad (1.26)$$

---

<sup>2</sup> $P \equiv \frac{dE}{dt} = \frac{dE}{dE'} \frac{dE'}{dt'} \frac{dt'}{dt} = \gamma^{-1} P' \gamma = P'$ .

Substituting  $a_{\perp}$  in the generalized Larmor formula (Eq. 1.24):

$$P = \frac{2e^4}{3m^2c^3} B^2 \gamma^2 \beta^2 \sin^2 \theta. \quad (1.27)$$

The power is usually rewritten in terms of the Thomson cross section  $\sigma_T \equiv 8\pi/3 (e^2/m_e c^2)^2$ , the magnetic energy density,  $U_B = B^2/8\pi$  (in Gaussian units), and  $\beta = v/c$ . In the case of an isotropic distribution of pitch angles, the term  $\sin^2 \theta$  can be averaged over the solid angle by is  $2/3$ . This gives the average synchrotron power per electron:

$$\langle P \rangle = \frac{4}{3} \sigma_T \beta^2 \gamma^2 c U_B. \quad (1.28)$$

Relativistic effects boost the average radiated power by a factor of  $\gamma^2$  compared with the non-relativistic ( $\gamma = 1$ ) case. The backward lobe of the synchrotron pattern is redshifted by Doppler effect, whereas the frontward lobe is blueshifted. As  $v$  approaches  $c$ , the power pattern of Larmor radiation is relativistically beamed in the electron frame sharply along the direction of motion in the observer's frame (see Fig. 1.7).

**Emission spectrum from a single electron** An observer at rest sees the emitted radiation confined to a very narrow beam of width  $\sim 2/\gamma$  (see Fig. 1.7). The duration of the observed pulse is even shorter than the time the electron needs to cover  $1/(\pi\gamma)$  of its orbit, because the electron is moving toward the observer with a speed approaching  $c$  and so is covering some distance between two photon emissions. Thus; a plot of the power received as a function of time is a very spiky series of widely separated narrow pulses. The observed synchrotron power spectrum is the Fourier transform of this time series of pulses and is given by:

$$P(\nu) = \frac{\sqrt{3}e^3 B \sin \theta}{m_e c^2} F(\nu/\nu_c), \quad (1.29)$$

$$F(\nu/\nu_c) = \left(\frac{\nu}{\nu_c}\right) \int_{\nu/\nu_c}^{\infty} K_{5/3}(x) dx. \quad (1.30)$$

It gives the total instantaneous power emitted by an electron, where  $K_{5/3}$  is a modified Bessel function of fractional order  $5/3$ , and  $\nu_c$  is the critical frequency:

$$\nu_c = \frac{3e}{4\pi m c} B \sin \theta \gamma^2. \quad (1.31)$$

The function  $F$  peaks at  $\nu \sim 0.29\nu_c$ . Therefore, the approximation that most of emission occurs at  $\nu \sim \nu_c$  is often made, and the function  $F$  is then replaced by a delta

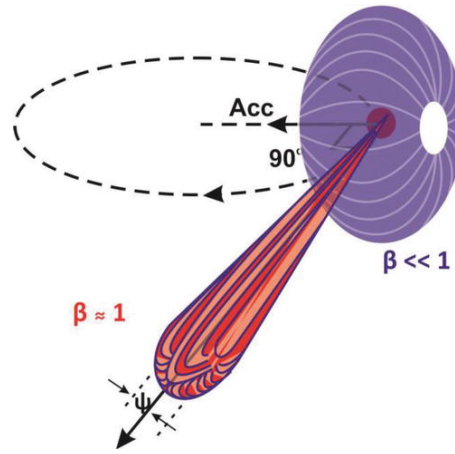


FIGURE 1.7: Radiation pattern of charged particles moving in a circular path: blue ( $\beta \ll 1$ ) and red ( $\beta \approx 1$ ) give ref. The opening angle of the frontward lobe is  $\psi \sim 2/\gamma$  whereas the backward lobe is smashed. Source of illustration: <https://www.intechopen.com/books/synchrotron-radiation-useful-and-interesting-applications/fundamental-of-synchrotron-radiations>

approximation:

$$F(\nu/\nu_c) = \left(\frac{\nu}{\nu_c}\right) \int_{\nu/\nu_c}^{\infty} K_{5/3}(x) dx = \delta(\nu - \nu_c). \quad (1.32)$$

**Synchrotron spectrum from a distribution of electrons** If a synchrotron source having any arbitrary distribution of electron energies is optically thin, its spectrum is the superposition of the spectrum from individual electrons. Assuming a spatially averaged differential distribution of the number of electrons,  $dN_{el}/d\gamma$ , which is also isotropic in the pitch angle, the total synchrotron luminosity is:

$$L_{\nu}^{Sy} = \int_1^{\infty} \mathcal{L}_{\nu}^{Sy} \frac{dN_{el}}{d\gamma} d\gamma, \quad (1.33)$$

where  $\mathcal{L}_{\nu}^{Sy}$  represents the luminosity of a single electron. The lower limit integral represents the energy of the electrons in their rest frame, for which the Lorentz factor  $\gamma = 1$ . The energy distribution of electrons in most synchrotron sources is approximately a power law:

$$\frac{dN_{el}}{d\gamma} = N_0 \gamma^{-S} \quad , \quad \gamma_1 \leq \gamma \leq \gamma_2,$$

where  $N_0$  is the normalization and  $S$  is called the spectral index. In the approximation that  $\nu_c(\gamma_1) \ll \nu \ll \nu_c(\gamma_2)$ , the integral of Equation 1.33 can be calculated analytically [Westfold (1959)] and one obtains:

$$L_{\nu}^{Sy} \propto B^{(S+1)/2} \nu^{-(S-1)/2}. \quad (1.34)$$

Described quantity	$dN_{el}/d\gamma$	$L_\nu$	$\nu f_\nu, \nu L_\nu$	$dN/dE$
Spectral and photon Index	S	$\alpha$	$\alpha'$	$\Gamma$
$S$		$2\alpha + 1$	$2\alpha' + 3$	$2\Gamma - 1$
$\alpha$	$(S - 1)/2$		$\alpha' + 1$	$\Gamma - 1$
$\alpha'$	$(S - 3)/2$	$\alpha - 1$		$\Gamma - 2$
$\Gamma$	$(S + 1)/2$	$\alpha + 1$	$\alpha' + 2$	

TABLE 1.3: Summary of the relations of the spectral and photon indices. Each line gives the respective index depending on the index of the respective column.

This result implies an important feature, since from a spectrum  $L_\nu$ , with a spectral index  $\alpha$ , one can deduce the spectral index of the underlying electron spectrum.

As it can be confusing to know which index describes what quantity, in this work,  $S$  will always designate the spectral index of the electrons, while the index of the measured spectrum  $\alpha$  will be linked to the quantity  $L_\nu$  (but not to  $\nu L_\nu$  or  $\nu f_\nu$ ). The relationships between these different quantities can be found by considering Eq. 1.3 and Eq. 1.5, and are summarized in Table 1.3

**Synchrotron cooling time** The typical synchrotron cooling time can be estimated by dividing the energy of the electrons by the rate at which they are radiating away their energy [Ghisellini (2013)]:

$$t_{syn} = \frac{E}{\langle P \rangle} = \frac{\gamma m_e c^2}{(4/3)\sigma_T c U_B \gamma^2 \beta^2} \sim \frac{7.75 \times 10^8}{B^2 \gamma} s = \frac{24.57}{B^2 \gamma} yr. \quad (1.35)$$

The rate at which an electron loses energy to synchrotron radiation is proportional to  $E^2$ , so higher-energy electrons will be depleted more rapidly.

### Inverse Compton scattering

Synchrotron radiation can generate photons up to a maximum theoretical energy of  $h\nu_{max} \sim \kappa 68$  MeV with  $\kappa \sim 1 - 3$  [Aharonian et al. (2004b)]. Thus, it can not explain the high energy part of the Crab Nebula spectrum ( $E \gtrsim 100$  MeV). Another non-thermal mechanism that can produce highly energetic photons is *inverse Compton scattering*. It describes the scattering of photons of energy  $\varepsilon$  on relativistic particles of energy  $E$ . The discussion is limited again to the case of electrons. Two limits cases have to be mentioned:

- *Thomson-Limit*: the photon energy  $\varepsilon'$  in the system where the electron is at rest is much lower than the rest mass energy of the electron,  $\varepsilon' \ll mc^2$ .

- *Klein-Nishina-Limit*: the photon energy  $\varepsilon'$  in the system where the electron is at rest is much greater than the rest mass energy of the electron,  $\varepsilon' \gg mc^2$ .

In the case of the Crab Nebula, at energies larger than a few 100 GeV, inverse Compton scattering starts to enter in the Klein-Nishina regime, but are not expected to dominate in the low-energy part ( $E \lesssim 500$  GeV) [Yeung and Horns (2019)]. We will adopt the following notations: quantities marked with an apostrophe “'” refer to the rest system of the electron. The initial energy of the photons is denoted by  $\varepsilon$ . Quantities after the interaction are given by the index “1”. Let us choose the electron momentum to be along the x-axis of the coordinate system  $p^\mu = (E, p_x, 0, 0)$ , then  $\theta$  denotes the angle between the photon momentum  $k^\mu = (\varepsilon, k \cos \theta, k \sin \theta, 0)$ , and the  $x$ -axis (in this notation,  $\theta$  should not be confounded with the pitch angle). The following calculations can be found with more details in Blumenthal and Gould (1970).

**Energy loss rate in Thomson limit** Suppose a highly relativistic electron moving through an isotropic photon gas. The electron will lose energy through the inverse Compton process. In the Thomson limit, the energy of the scattered photon in the laboratory system,  $K$ , is much greater than its energy before scattering, which can therefore be neglected. The scattering is *elastic* and the energy loss of the electron is then:

$$-\frac{dE}{dt} = \frac{dE_1}{dt}, \quad (1.36)$$

where  $E_1$  is the energy of the photon gas after scattering. The energy variation  $dE_1/dt$  is Lorentz invariant<sup>3</sup>, since it behaves like a Lorentz transformation as the ratio  $k_0/x_0^*$ . Furthermore, in the Thomson-Limit and in the rest system of the electron  $K', \varepsilon'_1 \sim \varepsilon'$ . Then the energy loss rate of the electron can be rewritten:

$$-\frac{dE}{dt} = \frac{dE'_1}{dt'} = \sigma_T c U', \quad (1.37)$$

with  $U'$  the total energy density of the photon gas in  $K'$ ,  $U' = \int \varepsilon' dn'$ , where  $dn'$  represents a differential photon number density. The electron will take from the incident radiation the amount of power flowing through the area  $\sigma_T$  and reradiate that power over the doughnut-shaped pattern given by Larmor's equation. The energy density of the photon distribution  $U$  in the laboratory system is obtained in the following way:

<sup>3</sup>For a photon,  $ds^2 = dt^2 - (dx)^2 = 0 = k_\mu k^\mu$ . It follows that  $k_0/x_0 = k_i/x_i$ . With this relation and a Lorentz transformation,  $\frac{k_0}{x_0} = \frac{\Lambda_{0\mu} k'^\mu}{\Lambda_{0\nu} x'^\nu} = \frac{\Lambda_{00} k'^0 + \Lambda_{0i} k'^i}{\Lambda_{00} x'^0 + \Lambda_{0i} x'^i} = \frac{k'_0}{x'_0} \frac{\Lambda_{00} + \Lambda_{0i} k'^i/k'_0}{\Lambda_{00} + \Lambda_{0i} x'^i/x'^0} = \frac{k'_0}{x'_0}$  and thus  $k_0/x_0$  is Lorentz-invariant.

similarly to  $dE_1/dt$ ,  $dn/\varepsilon$  is also Lorentz-invariant<sup>4</sup>. Furthermore, the photon energy  $\varepsilon'$  in  $K'$ , is obtained by a Lorentz transform in the  $x$ -direction:

$$\varepsilon' = \gamma\varepsilon(1 - \beta \cos \theta). \quad (1.39)$$

Thus, the energy density of the photons can be calculated in the laboratory system, where the approximation  $\beta \rightarrow 1$  can be made:

$$U' = \int (\varepsilon')^2 \frac{dn'}{\varepsilon'} = \gamma^2 \int (1 - \cos \theta)^2 \varepsilon dn. \quad (1.40)$$

For an isotropic distribution, one can average over theta, so that  $\langle (1 - \cos \theta)^2 \rangle = 4/3$ . In the laboratory system, the energy loss of the electron is given by

$$-\frac{dE}{dt} = \frac{4}{3} \sigma_T c \beta \gamma^2 U_{iso}. \quad (1.41)$$

Let us notice the simple ratio of IC to synchrotron losses:

$$\frac{P_{IC}}{P_{sync}} = \frac{U_{rad}}{U_B}. \quad (1.42)$$

For an isotropic gas, the mean energy of the scattered photon  $\langle \varepsilon_1 \rangle$  is, in the Thomson limit:

$$\langle \varepsilon_{IC} \rangle = \frac{4}{3} \gamma^2 \langle \varepsilon \rangle, \quad (1.43)$$

where  $\langle \varepsilon \rangle$  is the mean energy of the photon gas before scattering, and  $\langle \varepsilon_{IC} \rangle$  is the mean energy of the photon after scattering.

**Inverse-Compton energy spectrum** In order to calculate the spectrum produced by an electron scattering off the initial photon distribution, the process is again considered in the rest system of the electron  $K'$ . The distribution of scattered photons in energy and solid angle, per time per electron and within  $d\varepsilon'$  is

$$\frac{d^4 N_{\gamma, \varepsilon}}{dt' d\varepsilon'_1 d\Omega'_1 d\varepsilon'} = dn'(\varepsilon', \varepsilon) c \frac{d^2 \sigma}{d\varepsilon'_1 d\Omega'_1}, \quad (1.44)$$

with  $dn'(\varepsilon', \varepsilon)d\varepsilon'$ , the differential photon density in  $K'$ , within  $d\varepsilon'$ , resulting from the photons within the interval  $d\varepsilon$  in  $K$ . The differential cross section can be calculated

<sup>4</sup>The differential number of particles  $dN$ , together with the volume element  $dV$ , give the differential number of particles per volume  $dn = dN/dV$ . The three-dimensional volume element can be expressed by the Lorentz-variant four-volume  $d^4x$ , so that applies

$$dn = \frac{dN}{dV} = \frac{dN}{d^4x} dx_0 \quad (1.38)$$

thus  $dn$  transforms like  $x_0$  and  $dn/\varepsilon$  is Lorentz-invariant.

using classical electrodynamics. The scattered photon distribution in the laboratory system is obtained by integration of Eq. 1.44:

$$\frac{d^2 N_{\gamma,\varepsilon}}{dt d\varepsilon_1} = \int \int \frac{d^4 N_{\gamma,\varepsilon}}{dt' d\varepsilon'_1 d\Omega'_1 d\varepsilon'} \frac{dt'}{dt} \frac{d\varepsilon'_1}{d\varepsilon_1} d\varepsilon' d\Omega'_1. \quad (1.45)$$

Again, the detailed calculations of this integral can be found in [Blumenthal and Gould \(1970\)](#). In the general case, and in the Klein Nishina limit, the derivation of the photon distribution is similar, but the recoil of the electron must be taken into account:

$$\frac{d^2 N_{\gamma,\varepsilon}}{dt d\varepsilon_1} = \frac{3}{4} \frac{\sigma_{Tc}}{\gamma^2} \frac{n(\varepsilon) d\varepsilon}{\varepsilon} f_{IC}(\varepsilon, \varepsilon_1, \gamma), \quad (1.46)$$

with  $n$  the photon density averaged over  $\theta$  and  $f_{IC}$  radiation distribution function

$$f_{IC}(\varepsilon, \varepsilon', \gamma) = 2q \ln q + 1 + q - 2q^2 + \frac{1}{2} \frac{\left(\frac{4\varepsilon\gamma}{mc^2} q\right)^2}{1 + \frac{4\varepsilon\gamma}{mc^2} q} (1 - q), \quad (1.47)$$

with the kinematic variable  $q$ :

$$q = \frac{h\nu}{4\varepsilon\gamma^2 [1 - h\nu/(\gamma mc^2)]}, \quad \text{with } h\nu = \varepsilon_1. \quad (1.48)$$

The photon distribution  $n$  scattering the electron, is often referred to as the seed-photon field  $n_{seed}$  and represents the number of photons per time and frequency interval within  $dV$  and  $d\varepsilon$ . Finally, the luminosity of a single electron is obtained by integration over all incident photon energies  $\varepsilon$ ,

$$\mathcal{L}_\nu^{IC} = h^2 \nu \int_{h\nu/(4\gamma^2)}^{h\nu} \frac{d^2 N_{\gamma,\varepsilon}}{dt d\nu} d\varepsilon. \quad (1.49)$$

From the kinematics of the scattering process, the restrictions  $1 \gg (1/4)\gamma^2 \leq q \leq 1$  are obtained. This also results in the integration limits of the above equation. If the electron population has a power-law distribution of index  $-S$ , the resulting IC spectrum is also described by a power law. In the Thomson regime, the photon spectrum index is related to that of the electrons by  $L_\nu \propto \nu^{-(S-1)/2}$ , similarly to the case of synchrotron radiation. In the Klein-Nishina regime, the resulting photon spectrum becomes steeper:  $L_\nu \propto \nu^{-S}$ .

### 1.3.4 Dynamics of a supernova remnant

This subsection presenting the evolution of SNRs was written with the help of the work from [Ferrand \(2008\)](#). A spherical point-source explosion such as a supernova produces

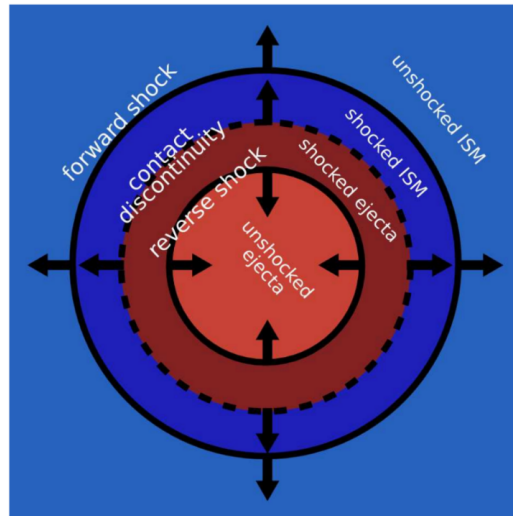


FIGURE 1.8: Waves structure for a spherical shock. The ejecta are shown in red and the interstellar medium is represented in blue. Shocked material is in dark color and undisturbed material is in light colors. The illustration is from [Ferrand \(2008\)](#)

a particular three waves structure (see Fig. 1.8):

- **The forward shock** moves forward in the upstream undisturbed medium (and accelerates it).
- **The contact discontinuity** isolates the ejecta from the supernova and matter from the interstellar medium.
- **The reverse shock**, which propagates back in the ejecta (and slow them down).

Four distinct phases are characterizing the evolution of a supernova remnant, from its explosion to its dilution in the ISM [see [Chevalier \(1977\)](#), [Truelove and McKee \(1999\)](#)]. The main physical parameters are the supernova energy  $E_{sn}$  (typically  $10^{51}$  erg), the ejecta mass  $M_{ej}$  (typically a few solar masses  $M_{\odot} = 2 \times 10^{30}$  kg), and the interstellar medium density  $n_{ism}$  (typically 1 particle per  $\text{cm}^3$ ).

**Free expansion phase** During its first hundred of years, the SNR evolution is governed by the ejecta: its radius evolves as

$$R_{snr}(t) = v_s t, \quad (1.50)$$

where the constant  $v_s$  is the expansion speed and is obtained from energy conservation:

$$E_{sn} = \frac{1}{2} M_{ej} v_s^2. \quad (1.51)$$

The ejecta being supersonic, it creates a shock wave in the ISM. The shocked interstellar medium is pushed by the ejecta and swell up between the contact discontinuity and the forward shock (see Fig. 1.8).

**Sedov-Taylor phase** The ejecta expand freely until they have accumulate a mass of ISM roughly equal to their own mass. This happens after a time

$$t_{ST} \simeq 210 \text{ yr} \left( \frac{E_{sn}}{10^{51} \text{ erg}} \right)^{-1/2} \left( \frac{M_{ej}}{1 M_{\odot}} \right)^{5/6} \left( \frac{n_{ism}}{1 \text{ cm}^3} \right)^{-1/3}, \quad (1.52)$$

corresponding to a radius  $R_{ST}$  and a velocity  $v_{ST}$ . After that, the SNR evolution is ruled by the swept-up shell of shocked ISM, so that energy conservation is now given by:

$$E_{sn} = \frac{1}{2} \left( \frac{4}{3} \pi R_s^3 \rho_{ism} \right) v_s^2. \quad (1.53)$$

A reverse shock develops from the contact discontinuity towards the core of the remnant, heating and slowing down the ejecta. This shock rebounds at the SNR center, and gradually dissipates. The contact discontinuity itself gets unstable and consequently breaks. The SNR is then a hot expanding bubble.

**Pressure-driven phase** During the first two phases, the cooling time of the very hot gas is so long (regarding the SNR dynamics), that radiative energy losses are negligible. But after  $\sim 10000$  years, the accumulated ISM starts cooling and quickly collapses to form a thin and cold outer shell. The transition takes place after a time

$$t_{PD} \simeq 29000 \text{ yr} \left( \frac{E_{sn}}{10^{51} \text{ erg}} \right)^{4/7} \left( \frac{n_{ism}}{1 \text{ cm}^3} \right)^{-9/17}, \quad (1.54)$$

corresponding to a radius  $R_{PD}$ :

$$R_{PD} \simeq 18 \text{ pc} \left( \frac{E_{sn}}{10^{51} \text{ erg}} \right)^{5/17} \left( \frac{n_{ism}}{1 \text{ cm}^3} \right)^{-7/17}. \quad (1.55)$$

The hot core then pushes the shell, the SNR expansion is supported by its own pressure  $P_{snr}$  so that:

$$\frac{d}{dt}(M_{snr} v_s) = 4\pi R_{snr}^2 P_{snr}, \quad (1.56)$$

from which one derives

$$R_{snr}(t) \propto t^{2/7}. \quad (1.57)$$

**Momentum-driven phase** When the SNR pressure finally matches the ISM pressure, the shell no longer undergoes any force and moves inertially.

$$\frac{d}{dt}(M_{snr}v_{snr}) = 0, \quad (1.58)$$

from which one derives:

$$R_{snr}(t) \propto t^{1/4}. \quad (1.59)$$

Cosmic-ray acceleration is mostly efficient in the early phases of the SNR evolution [Lagage and Cesarsky (1983)], with maximum energies probably achieved at the beginning of the Sedov-Taylor phase.



## Chapter 2

# Non-thermal emission model of the Crab Nebula

In this chapter, the model and framework used in the computation of the non-thermal emission from the Crab Nebula are introduced. Using the equations of non-thermal radiation processes, a model for the broad band emission from the Crab Nebula can now be applied. The following assumptions are made within our model:

- For simplifying, the nebula is assumed to be spherically symmetric.
- The nebula is filled with an electron and positron distribution (abbreviated to electrons), which is represented by a volume-averaged spectral distribution of the number of electrons  $dN_{el}/d\gamma$ .
- The dust is contained in a shell of thickness  $\sim 0.6$  pc surrounding the synchrotron nebula.
- At first assumption, the magnetic field prevailing in the nebula is described by a volume averaged  $B$  field value, hence the term *constant B field model*. It is also assumed, that the pitch angle of the electrons is given by an isotropic distribution, which averages the contributions of the form  $\sin \theta$  to  $\sqrt{2/3}$ .

As discussed in Chapter 1, the non-thermal emission from the Crab Nebula can be explained by synchrotron and inverse Compton processes. In this chapter, the spatially-dependent equations used in the model is introduced. Then, the spatial and spectral modelling of the relativistic electrons in the nebula is presented in more details. Finally, the different seed photons fields involved in the IC process are presented.

## 2.1 Synchrotron and Inverse Compton emission from the Crab Nebula

In addition to the non-thermal emission, there are further contributions to the SED coming from the thermal emission of the dust,  $L_\nu^{dust}$ , and the optical emission from the filaments of the nebula,  $L_\nu^{optical}$ . The total luminosity is the sum of the individual components,

$$L_\nu = L_\nu^{nt} + L_\nu^{dust} + L_\nu^{optical}. \quad (2.1)$$

The total luminosity of the non-thermal radiation  $L_\nu^{nt}$ , is given by

$$\begin{aligned} L_\nu^{nt} &= \int_V d^3r \int_1^\infty d\gamma n_{el}(\gamma, r) (P_\nu^{Sy}(\gamma, r) + P_\nu^{IC}(\gamma, r)) \\ &= \int_\gamma d\gamma \frac{dN_{el}}{d\gamma} (\mathcal{L}_\nu^{Sy}(\gamma) + \mathcal{L}_\nu^{IC}(\gamma)), \end{aligned} \quad (2.2)$$

with  $[L_\nu] = \text{erg s}^{-1} \text{ Hz}^{-1}$ .  $\mathcal{L}_\nu^{Sy}$  and  $\mathcal{L}_\nu^{IC}$  for synchrotron and IC represent the single-particle emission functions and are given in Chapter 1 and in the next subsections. The IC or synchrotron emissivities are given by  $j(r, \nu) = \int_\gamma d\gamma n_{el}(\gamma, r) P_\nu(\gamma, r)$ , in units of  $\text{erg s}^{-1} \text{ Hz}^{-1} \text{ cm}^{-3}$ .  $P_\nu$  is the power radiated by a single electron of energy  $\gamma mc^2$ , located at a distance  $r$  from the center of the nebula. The electron-number volume density  $n_{el}$  is defined as the number of electrons between  $\gamma$  and  $d\gamma$  per unit volume ( $\text{cm}^{-3}$ ):

$$n_{el}(\gamma, r) = n_0(\gamma) \frac{dN_{el}}{d\gamma} e^{-\frac{r^2}{2\rho(\gamma)^2}}, \quad (2.3)$$

where  $dN_{el}/d\gamma$  is the energy spectrum of the electrons and is given in the subsection 2.2.4. The spatial distribution of electrons is taken as a Gaussian of scale length  $\rho$ , and the constant  $n_0$  is determined by integrating  $n_{el}$  over the volume of the nebula (see subsection 2.2.2 for more details).

### 2.1.1 Synchrotron emission from the Crab Nebula

The previous chapter (see Eq. 1.29) presented the specific (per unit wavelength) pitch-angle averaged power spectrum emitted by a single electron (in Gaussian units):

$$\mathcal{L}_\nu^{Sy} = \sqrt{\frac{2}{3}} \frac{\sqrt{3}e^3}{mc^2} \frac{\nu}{\nu_c} \int_{\nu/\nu_c}^\infty K_{5/3}(x) dx. \quad (2.4)$$

The critical frequency  $\nu_c$  (see Chapter 1, Eq. 1.31) is defined as

$$\nu_c = \sqrt{\frac{2}{3}} \frac{3e}{4\pi mc} B \gamma^2 = \nu_0 \gamma^2. \quad (2.5)$$

$\nu_c$  can be written as:

$$\nu_c = 4.199 \times 10^2 \gamma^2 \sqrt{\frac{2}{3}} \left( \frac{B}{10^{-4} G} \right) \text{ Hz}. \quad (2.6)$$

The *specific luminosity* from a distribution of electrons is obtained by summing the contribution from each electron and integrating over the volume of the nebula:

$$\begin{aligned} L_\nu^{Sy} &= \int_V d^3r \int_\gamma d\gamma n_{el}(\gamma, r) P_\nu^{Sy}(\gamma, r) \\ &= \int_V d^3r \int_\gamma d\gamma n_{el}(\gamma, r) \sqrt{\frac{2}{3}} \frac{\sqrt{3} e^3 B \nu}{mc^2 \nu_c} \int_{\nu/\nu_c}^\infty K_{5/3}(x) dx. \end{aligned} \quad (2.7)$$

### 2.1.2 Inverse Compton emission

In Chapter 1 (see Eq. 2.8), the IC specific (per unit wavelength) power spectrum emitted by a single electron (In Gaussian units) was derived :

$$\mathcal{L}_\nu^{IC} = \nu \int_{h\nu/(4\gamma^2)}^{h\nu} \frac{d^2 N_{\gamma, \varepsilon}}{dt d\nu} d\varepsilon = \frac{3}{4} \frac{\sigma_{TC} n(\varepsilon) d\varepsilon}{\gamma^2 \varepsilon} f_{IC}(\varepsilon, \nu, \gamma). \quad (2.8)$$

The total inverse Compton spectrum is obtained by integrating the scattered photon spectrum per electron over  $\gamma$  and  $\varepsilon$  and over the total volume of the Crab Nebula:

$$\begin{aligned} L_\nu^{IC} &= \int_V d^3r \int_\gamma d\gamma n_{el}(\gamma, r) P_\nu^{IC}(\gamma, r) \\ &= \int_V d^3r \int_\gamma d\gamma \frac{3}{4} \frac{\sigma_{TC}}{\gamma^2} h^2 \nu \int_{h\nu/(4\gamma^2)}^{h\nu} \frac{d\varepsilon}{\varepsilon} f_{IC}(\varepsilon, \nu, \gamma) n_{seed}(r, \varepsilon) n_{el}(\gamma, r). \end{aligned} \quad (2.9)$$

The spectral photon number density  $n_{seed}$  is defined in the section 2.3 and is defined as the number of photons per energy interval per volume and has units of  $\text{cm}^{-3} \text{ erg}^{-1}$ .

## 2.2 Relativistic electrons in the Crab Nebula

### 2.2.1 Two populations of electrons

Two different populations of relativistic electrons are needed to explain the observed synchrotron spectrum:

(1) the population of newly accelerated electrons with energies  $E \gg E_{cool}$ , which are injected downstream of the wind shock (hereafter the *wind* electrons),

(2) the population of lower energy electrons responsible for the radio emission,  $E \ll E_{cool}$ , which are supposedly ‘relic’ and (hereafter the *radio* electrons). As seen in Chapter 1 (see Eq. 1.35), the synchrotron lifetime of a relativistic electron is :

$$t_{syn} = \frac{E}{\langle P \rangle} = \frac{\gamma m_e c^2}{(4/3)\sigma_T c U_B \gamma^2 \beta^2}. \quad (2.10)$$

Assuming an average value for the magnetic field,  $B_0 \simeq (2-3) \times 10^{-4}$  G and a time period  $\Delta t \simeq 1000$  yr since the explosion of the Crab Nebula, it follows that the relativistic electrons in the nebula could be cooled down only to energies  $E_{cool} = \gamma_{cool} m_e c^2 \sim 200$  GeV, corresponding to synchrotron frequencies of  $\nu \simeq 10^{14}$ . This shows that the *wind* electrons are responsible for the synchrotron emission of the Crab Nebula starting from the near-IR/optical frequencies,  $\nu \gtrsim 10^{14}$  Hz, while the synchrotron radiation from radio to FIR wavelengths is due to the *radio* electrons.

There is an other argument in favor of the existence of two electron populations: for frequencies  $\nu$  such that  $10^7 \lesssim \nu \lesssim 10^{14}$ , the differential photon spectrum is well described by a single power-law  $L_\nu \propto \nu^{-\alpha_r}$ , with  $\alpha_r \simeq 0.3$  [Bietenholz et al. (1997)]. Then, the spectrum significantly softens in the near-IR/optical band  $L_\nu \propto \nu^{-\alpha_{opt}}$ , with  $\alpha_{opt} \sim 0.6$  [Lyutikov et al. (2019)]. Under the assumption that there is only one electron population injected at the termination shock and cooling down for energies greater than  $E_{cool}$ , a break in the synchrotron spectrum should be observed, with the spectral index softening from  $\alpha_r = 0.3$  to  $\alpha_r + 1/2 = 0.8$  (see Chapter 1, Eq. 1.3.2), which is different from 0.6. Therefore, a single electron population alone cannot explain the observed synchrotron spectrum.

### 2.2.2 Estimation of the electrons spatial distribution from observations

As seen in the previous chapter, it is often assumed that most of the synchrotron emission is emitted at  $\nu \sim \nu_c$ , with  $\nu_c = \nu_0 \gamma^2$ . The approach here is to infer the scale length of the electrons,  $\rho$ , from the spatial extension of the synchrotron emission.

#### Observations of the synchrotron extension

The intensity at the projected angular distance from the center of the nebula is well described by a Gaussian distribution (see de Jager and Harding (1992), Hillas et al. (1998)).

Figure 2.1 shows measurements of characteristic extensions (defined as the standard deviation  $\sigma_{1D}$ ) of the synchrotron emission as well as the function that describes the data best. The Chandra data points <sup>1</sup> are determined with DS9 by taking the 68% containment radius  $R_{68}$  of the Crab Nebula for different energy bins (see Fig. 2.2). The choice of defining the extension as 68% containment radius  $R_{68}$  is made for comparison with the available data [Yeung and Horns (2019)]. No background subtraction is performed because there is virtually none. The available energy band [0.3 – 10 keV] of the image is linearly divided in 10 energy bins. For each energy bin, the centroid (intensity weighted) position of the image along the horizontal and vertical directions is calculated.

The 68% containment radius  $R_{68}$  is then determined by adjusting the radius of the circle having for center the centroid of the image until it matches 68% of the total integrated intensity. The circle of radius  $R_{68}$  and its center are overlaid in Fig 2.2. The standard deviation is deduced from the 68% containment radius  $R_{68}$  by the relation (see Appendix E):

$$\sigma_{1D} = \frac{R_{68}}{1.509}. \quad (2.11)$$

In figure 2.1, it can be seen that the characteristic extension in the radio band,  $\theta_{radio} = 78 \pm 4$  arcsec is constant up to a frequency  $\nu_{break} = (1.2 \pm 0.3) \times 10^{14}$  Hz. This corresponds to the synchrotron radiation supposedly due to the *radio electrons* (see subsection 2.2.1), and associated to the optical peak  $\nu_{opt}$  seen in the synchrotron spectrum. The value of 78 arcsec is simply determined by averaging the two radio data points. The uncertainty  $\Delta\theta_{radio} = 4$  arcsec is given by the difference between these two points divided by two (if the two measurements have equal chances to be true). The observed characteristic extension  $\theta$ , between  $\nu_{break}$  and  $\nu_{obs,max} = 1.4 \times 10^{19}$  Hz (maximal observed frequency) is shrinking with the photon energy with a power-law index of  $\alpha = 0.125 \pm 0.004$ . Thus,  $\theta$  can be written as a function of the photon frequency as:

$$\theta = \theta_{radio} \left( \frac{\nu}{\nu_{break}} \right)^{-\alpha}. \quad (2.12)$$

The synchrotron size is decreasing with the frequency, reflecting the cooling of the electrons as they propagate outward the nebula. The values of  $\nu_{break}$ ,  $\alpha$  and their associated uncertainties  $\Delta\nu_{break}$  and  $\Delta\alpha$  have been obtained by fitting three different power law functions of the form  $\theta_i(\nu) = \theta_{radio}^i (\nu/\nu_{break}^i)^{-\alpha_i}$ , with  $i \in \{1, 2, 3\}$  to the measurements. The different functions are associated with  $\theta_{radio}^1 = \theta_{radio} = 78$ ,  $\theta_{radio}^2 = \theta_{radio} - \Delta\theta_{radio} = 74$  and  $\theta_{radio}^3 = \theta_{radio} + \Delta\theta_{radio} = 82$ . The uncertainties of  $\nu_{break}$  and  $\alpha$  are obtained by adding in quadrature the uncertainties of  $\Delta\nu_{break}^i$  and  $\Delta\alpha_i$  obtained for each of the three fitting:

<sup>1</sup>[ivo://ADS/Sa.CX0#obs/13154](https://ivo://ADS/Sa.CX0#obs/13154) (Chandra ObsId 13154).

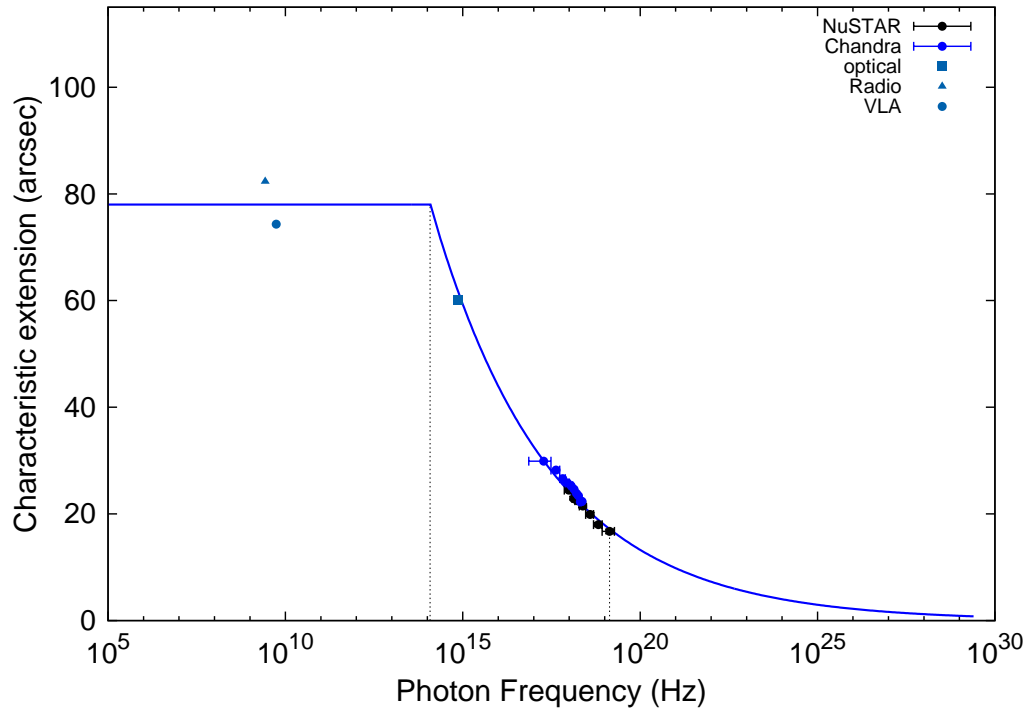


FIGURE 2.1: Characteristic extensions (defined as the standard deviation  $\sigma$ ; assuming the intensity to have a Gaussian profile) in different energy-segments, from the radio band to the X-ray band. The radio data are based on a VLA (5.5 GHz) image (published in [Bietenholz et al. \(2004\)](#)) and on the map of total intensity at 2.7 GHz in [Wilson \(1972\)](#). The optical data are from [Grindlay and Hoffman \(1971\)](#) and [Scargle \(1969\)](#). The Chandra characteristic extensions are determined within this work (see text for more details). The NuSTAR measurements are provided by [Madsen et al. \(2015\)](#). The blue line is the function which best describes the dependency between the characteristic extension and the photon energy. The left vertical dashed line represents the frequency  $\nu_{break} = (1.2 \pm 0.2) \times 10^{14}$  Hz at which the synchrotron extension starts to depend upon the frequency. The right dashed line indicates the frequency of the last data point:  $\nu_{obs,max} = (1.4 \pm 0.5) \times 10^{19}$ .

$$\Delta\nu_{break} = \sum_{i=1}^3 \sqrt{(\Delta\nu_{break}^i)^2}, \quad (2.13)$$

$$\Delta\alpha = \sum_{i=1}^3 \sqrt{(\Delta\alpha_i)^2}. \quad (2.14)$$

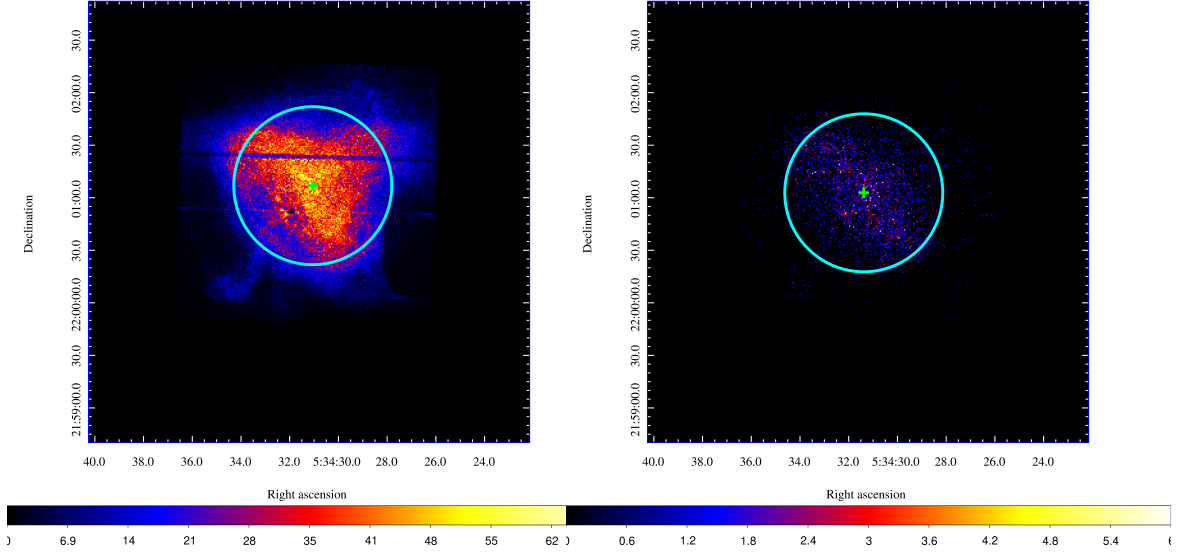


FIGURE 2.2: Chandra images of the Crab Nebula in the energy band 7.09-8.06 keV (right panel) and 0.3-1.27 keV (left panel). The light blue circle represents the 68% containment radius and the green cross the center of the circle and the centroid of the image (see text). The central blacked out region is the pulsar location and the horizontal line departing from it is the read-out of pulsed emission which spilled over. The Chandra images come from [ivo://ADS/Sa.CX0#obs/13154](http://ivo://ADS/Sa.CX0#obs/13154).

### Determination of the spatial distribution of the electrons

Under the assumption of a constant magnetic field, a spherical Gaussian function is assumed for the spatial distribution of the electrons responsible for the synchrotron emission. The electron-number volume density,  $n_{el}$ , has been defined previously by the Eq. 2.3. The constant  $n_0$  is simply determined by integrating  $n_{el}$  over the volume of the nebula and requiring:

$$4\pi \int_0^\infty r^2 n_0(\gamma) \frac{dN_{el}}{d\gamma} e^{-\frac{r^2}{2\rho(\gamma)^2}} dr = \frac{dN_{el}}{d\gamma}. \quad (2.15)$$

One gets:

$$n_0(\gamma) = \frac{1}{2\sqrt{2}\pi^{3/2}\rho(\gamma)^3}. \quad (2.16)$$

The scale length of the electrons,  $\rho$ , is inferred from the synchrotron extension. Considering that most of the synchrotron emission is emitted at  $\nu \sim \nu_c$  and that the critical frequency is defined as  $\nu_c \propto \gamma^2$ , thus  $\theta \propto \nu^\alpha \propto \gamma^{2\alpha}$ . The scale length of the electrons is related to the angular distance  $\theta$  by the relation:  $\rho = d \tan \theta \approx d\theta$  in the small-angle approximation. With  $d = 2$  kpc, the distance from us to the Crab Nebula, the following

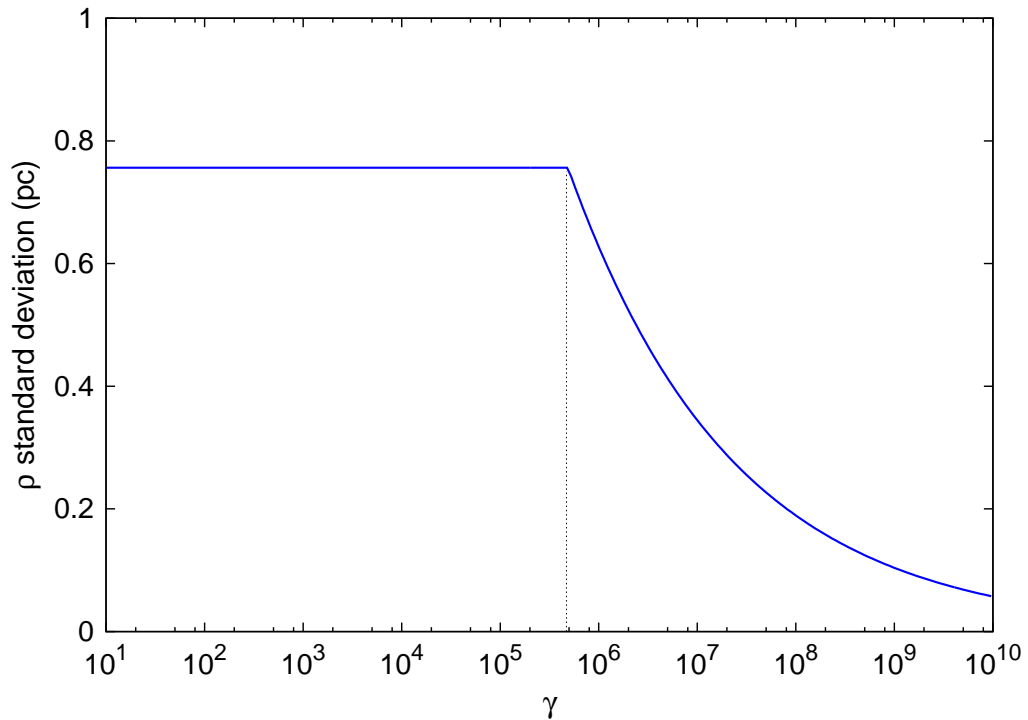


FIGURE 2.3: Scale length  $\rho$  of the electron distribution as a function of the Lorentz factor  $\gamma$ . The dashed line represents the parameter  $\gamma_{break}$  such that for  $\gamma < \gamma_{break}$ ,  $\rho$  is a constant.

expression for  $\rho$  is obtained:

$$\rho(\gamma) = \begin{cases} d \tan(\theta_{radio}) & \text{if } \gamma < \gamma_{break} = \sqrt{\frac{\nu_{break}}{\nu_0}} \\ d \tan\left(\theta_0 \left(\frac{\nu}{\nu_{break}}\right)^{-\alpha}\right) = d \tan\left(\theta_0 \left(\frac{\gamma}{\gamma_{break}}\right)^{-2\alpha}\right) & \text{else.} \end{cases} \quad (2.17)$$

Note that in the above expression, the angles should be expressed in degrees. The scale length  $\rho$  of the electrons is represented in Fig 2.3. The parameter  $\gamma_{break} = \sqrt{\nu_{break}/\nu_0} = (4.6 \pm 0.6) \times 10^5$  depends upon the value of the magnetic field inside the nebula (see Fig 2.3). The width of the electron distribution estimated from the observed synchrotron flux is shrinking with the electron energy with a power-law index of  $-2\alpha$  due to the cooling of the electrons.

The electron number density  $n_{el}$  is represented in fig 2.4. It can be seen that the scale length of the electron decreases with the Lorentz factor, but remains constant ( $\rho = \rho_{radio} = d \tan \theta_{radio}$ ) for lower energies electrons  $\gamma$ , such that  $10^2 \lesssim \gamma \lesssim \gamma_{break}$ .

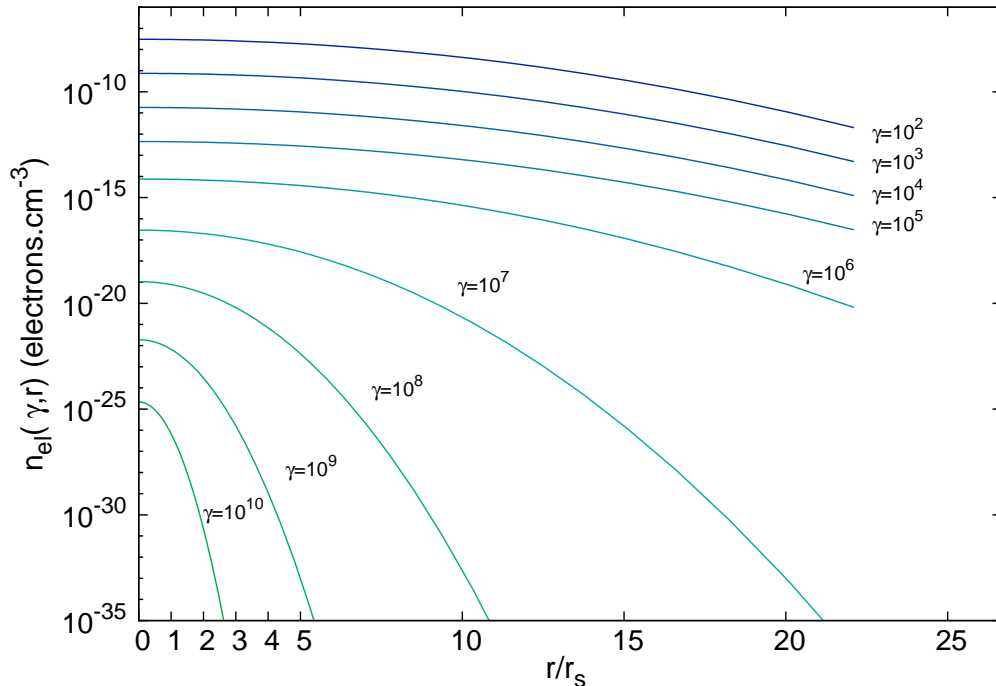


FIGURE 2.4: Electron number density  $n_{el}$ , as a function of the ratio  $r/r_s$  for different values of the Lorentz factor  $\gamma$ ,  $r$  is the distance to the center of the Crab Nebula and  $r_s$  is the termination shock radius. The radius of the nebula,  $R_{PWN}$  corresponds to  $r/r_s \approx 20$ .

Indeed, high-energy particles injected into the nebula at the wind shock experience both synchrotron cooling and energy loss owing to adiabatic expansion as they move outward through the nebula. Therefore, electrons with high Lorentz factor are located near the pulsar because they deplete more rapidly due to synchrotron losses, whereas lower energies electrons propagating outward the nebula undergo only adiabatic energy losses due to the convection of the wind flow.

### 2.2.3 Maximum value of the magnetic field

A maximum value for the magnetic field,  $B_{max}$ , can be derived by considering that the minimum energy to which the wind electrons are cooled,  $E_{cool}$ , cannot be smaller than the minimal energy of the radio electrons  $\nu_{opt}^{inf}$ . Let  $\nu_{opt}$  be the exact value at which there is a transition in the spectrum between the radio and wind electrons. As discussed earlier, the value of  $\nu_{opt}$  is not exactly known. Let  $\nu_{opt}^{inf}$  and  $\nu_{opt}^{sup}$  be the limit values of  $\nu_{opt}$ :  $\nu_{opt}^{inf} \leq \nu_{opt} \leq \nu_{opt}^{sup}$ , with  $\nu_{opt}^{inf} = 10^{13}$  and  $\nu_{opt}^{sup} = 10^{14}$ . It can be noted

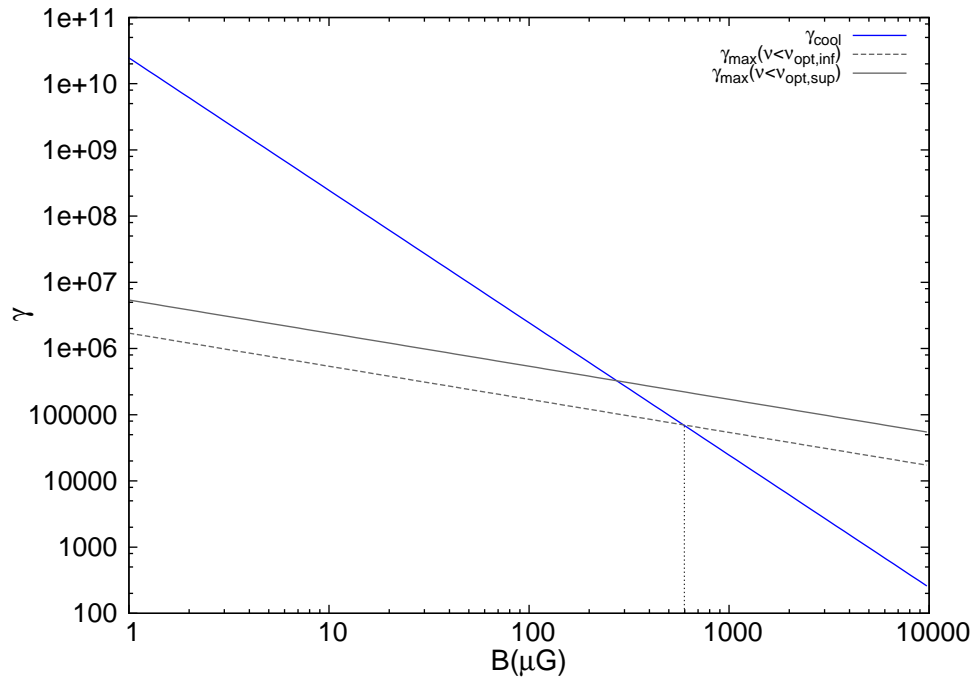


FIGURE 2.5: Lorentz factor  $\gamma$  as a function of the magnetic field  $B$  corresponding to the synchrotron cooling frequency  $\gamma_{cool}$ , to the upper  $\nu_{opt}^{sup}$  and lower  $\nu_{opt}^{inf}$  limits of the break frequency  $\nu_{opt}$ .

that  $\nu_{opt}^{sup} = 10^{14}$  might be higher (see the value obtained for  $\nu_{break}$  above) but here the constraint on the magnetic field is given by  $\nu_{opt}^{inf}$ . The Lorentz factor  $\gamma_{max}$  corresponding to  $\nu_{opt}$  is such that

$$\nu_{opt}^{inf} \lesssim \sqrt{\frac{2}{3}} \frac{3e}{4\pi mc} B \gamma_{max}^2 \lesssim \nu_{opt}^{sup}. \quad (2.18)$$

$\gamma \propto (\nu/B)^{1/2}$  is represented in fig. 2.5 for  $\nu_{opt}^{inf} = 10^{13}$ ,  $\nu_{opt}^{sup} = 10^{14}$  and  $\gamma \propto (\nu/B)^2$  for  $\nu_{cool}$ . The requirement  $\gamma_{opt}^{inf} \leq \gamma_{cool}$  gives an upper limit for the magnetic field:  $B_{max} = 597 \mu\text{G}$ .

#### 2.2.4 Modeled electron Energy spectrum

There are usually two different methods for the derivation of the electrons energy spectrum  $dN_{el}/d\gamma$ . The first method uses the observed synchrotron radiation spectrum to extract the spectrum of the electrons, assuming some distribution of the magnetic field. The second method relies on calculations for a given model of electron propagation in the nebula and an injection spectrum which would explain the observed synchrotron nebula and the intensity profile. In this work, the first method is used. The assumed

electron spectra for the radio and wind electron are similar to Meyer et al. (2010). The radio electrons, are assumed to follow a simple power law:

$$\frac{dN_{el}^r}{d\gamma} = \begin{cases} N_0^r \gamma^{-S_r} & \text{for } \gamma_{min}^r \leq \gamma \leq \gamma_{max}^r, \\ 0 & \text{else} \end{cases}$$

The spectrum of wind electrons also follows a power law, which, on the one hand has a “kink”, and on the other has a superexponential cut-off at lower energies:

$$\frac{dN_{el}^w}{d\gamma} = N_0^w \left\{ \begin{array}{ll} \left( \frac{\gamma}{\gamma_{break}^w} \right)^{-S_w} & \text{for } \gamma \leq \gamma_{break}^w, \\ \left( \frac{\gamma}{\gamma_{break}^w} \right)^{-S_w + \Delta S} & \text{for } \gamma_{break}^w \leq \gamma \leq \gamma_{max}^w, \\ 0 & \text{for } \gamma > \gamma_{max}^w, \end{array} \right\} \exp \left( - \left[ \frac{\gamma_{min}^w}{\gamma} \right]^\beta \right).$$

In contrast to the radio electrons spectrum, which breaks sharply at low energies, a super-exponential cut-off is chosen for the wind electrons. This is necessary to explain the maximum of the SED at optical wavelengths and the steep decay to infrared wavelengths (especially for the Spitzer measurements). The upper super-exponential cut-off of the spectrum can be explained by the fact that particles can only be accelerated to maximum energy. At very high energies, the particles of the shock front acceleration region escape very quickly, crossing the shock only a few times. The synchrotron spectrum is then used to find the parameters that best describes the data (see Chapter 3, subsection 3.1.2). The electron spectrum used in our model is represented in figure 2.6.

## 2.3 Seed photon fields in the Nebula

In order to calculate the inverse Compton spectrum (see Eq. 2.9), the spectral photon number density,  $n_{seed}$  needs to be determined. Assuming an isotropic volume emissivity  $j$  (in  $4\pi$  solid angle) in a spherical source, the *spectral number density* of photons at a distance  $r$  to the center of the nebula is [(Atoyan and Aharonian, 1996b)]:

$$n_{seed}(r, \varepsilon) = \frac{1}{h\varepsilon} \frac{1}{2c} \int_{r_{min}}^{r_{max}} \frac{r_1}{r} j(r_1, \varepsilon) \ln \left( \frac{r + r_1}{|r - r_1|} \right) dr_1. \quad (2.19)$$

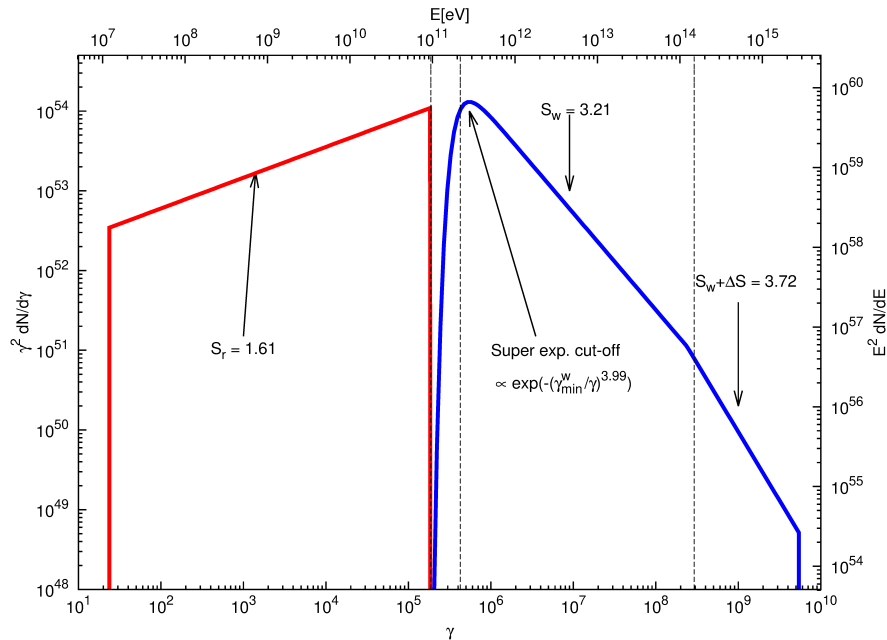


FIGURE 2.6: The two components of the electron spectrum used to calculate the broad band SED of the Crab Nebula in the constant B-field model. The radio electrons are showed in red solid line, while the wind electrons are represented by the blue solid line. The black dashed lines indicate the minimum, maximum and break energies.

The unit of  $n_{seed}$  is  $\text{eV}^{-1} \text{cm}^{-3}$ . See Appendix A for more details about the derivation of the spectral number density. The three main seed photon fields contributing to the IC scattering of the relativistic electrons in the Crab Nebula are: (i) the synchrotron radiation; (ii) the FIR ‘excess’ radiation which is attributed to the dust emission; (iii) the 2.7K cosmic microwave background radiation (CMB).

### 2.3.1 Scattering of IR photons from heated dust

Observations at sub-millimeter and far-infrared wavelengths [Marsden et al. (1984); Temim et al. (2006)] show an excess of the flux that can not be explained by the synchrotron continuum alone. The thermal-emission of the dust is responsible for that emission. The dust grains are swept-up by the supernova explosion and heated by radiations. The dust emission is concentrated in the filaments which are forming a shell of thickness  $\sim 0.6$  pc [Owen and Barlow (2015)] around the synchrotron nebula. A Heaviside function is then assumed for modelling the dust emissivity such that:

$$\begin{cases} j(r_1, \varepsilon) = j(\varepsilon) & \text{if } r_i < r < r_o \\ 0 & \text{else .} \end{cases}$$

The inner  $r_i$  and outer  $r_o$  radius of the dust shell are chosen such that  $r_i = 1.7$  pc and  $r_o = 2.3$  pc [Owen and Barlow (2015)]. The dust is heated to a temperature  $T_d$  by the

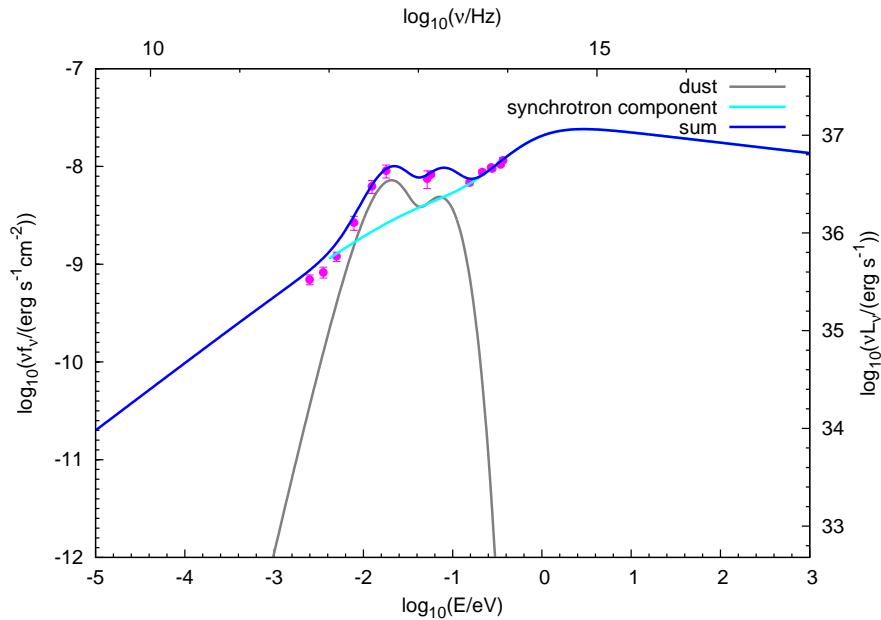


FIGURE 2.7: The contribution of dust emission from the filaments and synchrotron emission in the FIR-sub-mm range is shown in magenta points, the gray solid line represents the two-temperature-blackbody model used to fit the data and the light blue line represents the modelled synchrotron emission. The dark blue line is the total flux obtained from summing the synchrotron and the two dust components. The data are taken from [Gomez et al. \(2012\)](#).

radiation fields in the nebula. This produces a thermal emission that can be described by a so-called *gray body* spectrum. It follows essentially the Planck distribution of a blackbody, however, an additional normalization parameter,  $N_d$ , is left free to account for factors such as the dust distribution in the nebula or the shape of the dust grains. The gray body flux of thermal photons through a unit area at the surface of the emission region is given by:

$$f_\nu = \frac{8\pi N_d \nu^2}{c} \frac{1}{e^{h\nu/(k_B T_d)} - 1}. \quad (2.20)$$

After removing the contribution from line emission and synchrotron component (see Fig 2.7), the thermal emission observed in the FIR can be described by the sum of two grey bodies coming from a warm ( $T_w = 172.6$  K) and a cool ( $T_c = 47.6$  K) component:

$$f_\nu = \frac{8\pi N_d^c \nu^2}{c} \frac{1}{e^{h\nu/(k_B T_d^c)} - 1} + \frac{8\pi N_d^w \nu^2}{c} \frac{1}{e^{h\nu/(k_B T_d^w)} - 1}. \quad (2.21)$$

Although there might be a more complex temperature distribution of the dust in the

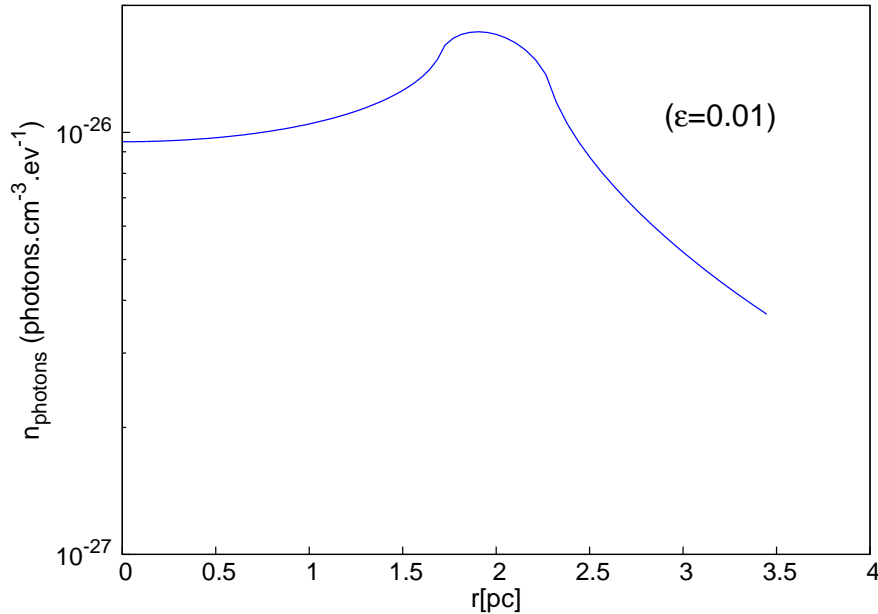


FIGURE 2.8: Dust photon number density in photons per cm<sup>3</sup> per eV (for an energy of  $\varepsilon = 0.01$  eV). Most of the photons are located in the area between  $1.7 \text{ pc} \lesssim r \lesssim 2.3 \text{ pc}$ .

remnant, a two-temperature component fit is enough for a first-order approach in modelling the SED. The photon number density can then be rewritten as

$$n_{seed}(\varepsilon, r) = \frac{1}{h\varepsilon} \frac{1}{2c} \int_{r_i}^{r_o} \frac{r_1}{r} \ln \frac{r+r_1}{|r-r_1|} j(\varepsilon) dr_1 = j(\varepsilon) \frac{1}{h\varepsilon} \frac{1}{2c} \int_{r_i}^{r_o} \frac{r_1}{r} \ln \frac{r+r_1}{|r-r_1|} dr_1, \quad (2.22)$$

with  $\varepsilon = h\nu$  and  $j(\varepsilon) = f_\nu 4\pi d^2 / V_{shell}$ . The integral over  $r_1$  can be calculated analytically. The dust photon number density is represented in Fig 2.8 and has a maximum value between  $r = 1.7 \text{ pc}$  and  $r = 2.3 \text{ pc}$ .

Fig 2.9 represents the spatial overlap between the dust photons and the electrons. There is a little “kink” observed at  $r \lesssim 2$ , for  $\gamma = 10^2$  and  $\gamma = 10^2$ . This is expected, as the radio electrons have a greater characteristic extension, they are scattering with more photons from the dust. The wind electrons, having higher energy are located near the center of the nebula and therefore are almost not interacting with the dust located in the shell.

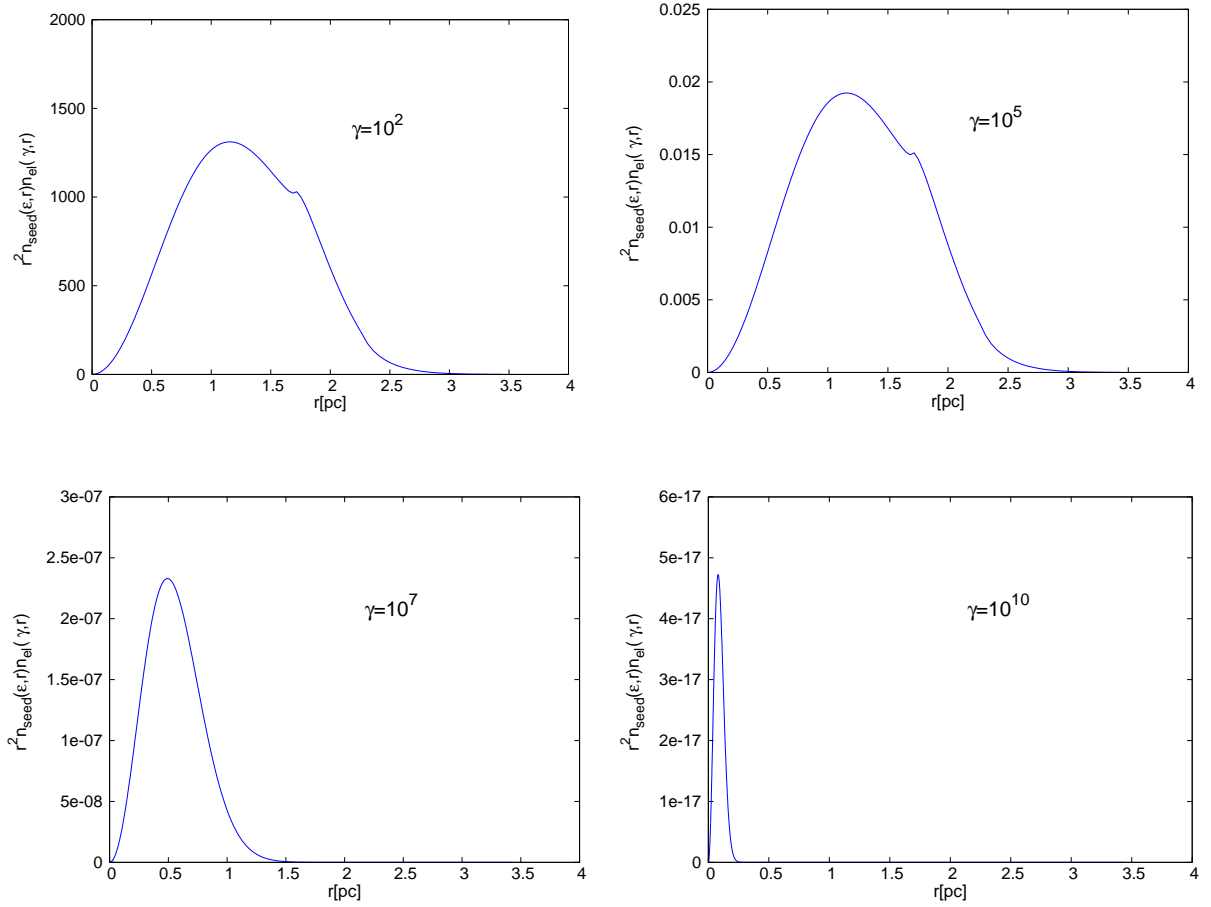


FIGURE 2.9: Spatial overlap between the electrons and dust photons  $n_{seed}(\varepsilon, r)n_{el}(\gamma, r)$  multiplied by  $r^2$ , for  $\varepsilon = 0.01$  and for different values of  $\gamma$ .

### 2.3.2 Synchrotron self-Compton scattering

The SSC describes the mechanism by which the photons emitted by synchrotron radiation are scattered off by the same electron population that produce them:

$$L_{\nu}^{IC} = \int_V d^3r \int_{\gamma} \frac{3}{4} \frac{\sigma_{TC}}{\gamma^2} h^2 \nu d\gamma \int_{h\nu/4\gamma^2}^{h\nu} \frac{d\varepsilon}{\varepsilon} \frac{1}{2c} \frac{1}{h\varepsilon} f_{IC}(\varepsilon, \nu, \gamma) \int dr_1 \frac{r_1}{r} \ln \frac{r+r_1}{|r-r_1|} j_{sync}(r_1, \tilde{\nu}) n_{el}(\gamma, r), \quad (2.23)$$

$$j_{sync}(r_1, \tilde{\nu}) = \frac{1}{4\pi} \int_{\gamma'} d\gamma' n_{el}(\gamma', r_1) \frac{\sqrt{3}e^3 B \sin \theta}{mc^2} \frac{\tilde{\nu}}{\nu_c} \int_{\tilde{\nu}/\nu_c}^{\infty} K_{5/3}(x) dx, \quad (2.24)$$

with  $j_{sync}$  the synchrotron emissivity. As seen in Chapter 1, Eq. 1.43, for Thomson-type inverse-Compton scattering:

$$\langle \varepsilon_{IC} \rangle = \frac{4}{3} \gamma^2 \langle \varepsilon \rangle. \quad (2.25)$$

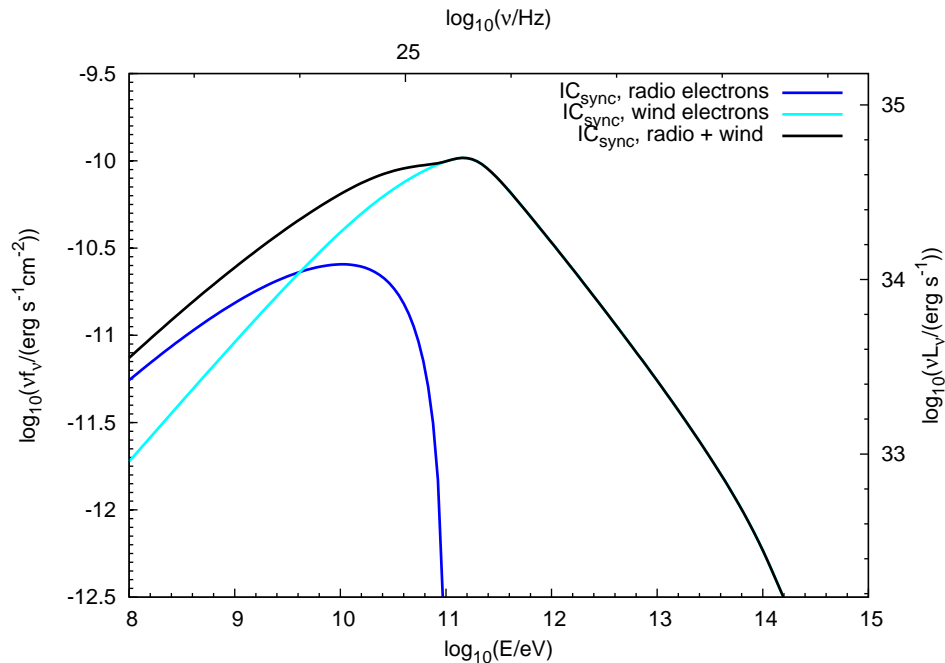


FIGURE 2.10: SSC flux from the Crab Nebula, calculated in the frame of the constant  $B$ -field model.

From this equation, it is possible to infer which electrons are scattering off which photons to produce the observed IC spectrum. The radio electrons contribute to IC frequencies  $\nu_{IC}$ , such that  $10^{23} \lesssim \nu_{IC} \lesssim 10^{25}$ , whereas the wind electrons are mostly producing photons with frequencies  $10^{24} \lesssim \nu_{IC} \lesssim 10^{28}$ , as it can be seen in Fig. 2.10. In the low-energy regime ( $E \lesssim 500$  GeV), the shape of the SSC spectrum is described by a power law of index  $(S - 1)/2$ , if the electron population has a power-law distribution of index  $-S$ . In the Klein-Nishina regime, the resulting photon spectrum becomes steeper:  $F(\nu) \propto \nu^{-S}$ .

For  $\nu_{IC} = 10^{23}$ , for example, the radio electrons ( $10^2 \lesssim \gamma_{radio} \lesssim 10^5$ ) are scattering off soft photons with frequencies  $\nu_{seed}$  such that  $10^{13} < \nu < 10^{19}$ . The function  $g_\gamma$  is defined such that:

$$g_\gamma(\varepsilon) = \frac{3}{4} \frac{\sigma_{TC}}{\gamma^2} h^2 \nu d\gamma \frac{d\varepsilon}{\varepsilon} \frac{1}{2c} \frac{1}{h\varepsilon} f_{IC}(\varepsilon, \nu, \gamma) \int_V d^3r n_{seed}(r, \varepsilon) n_{el}(\gamma, r), \quad (2.26)$$

where  $\varepsilon$  is defined as  $\varepsilon = h\nu_{seed}$ . The function  $g_\gamma$  represents the IC flux coming from the synchrotron seed photons for a fixed value of  $\gamma$ . It is represented for  $\nu = 10^{23}$  in Fig. 2.11 (for  $\gamma = 10^3$ ) and in Fig. 2.12 ( $\gamma = 10^5$ ). It can be seen that for fixed values of  $\nu$  and  $\gamma$ , the contribution to the IC flux is very peaked. Furthermore, only a narrow range

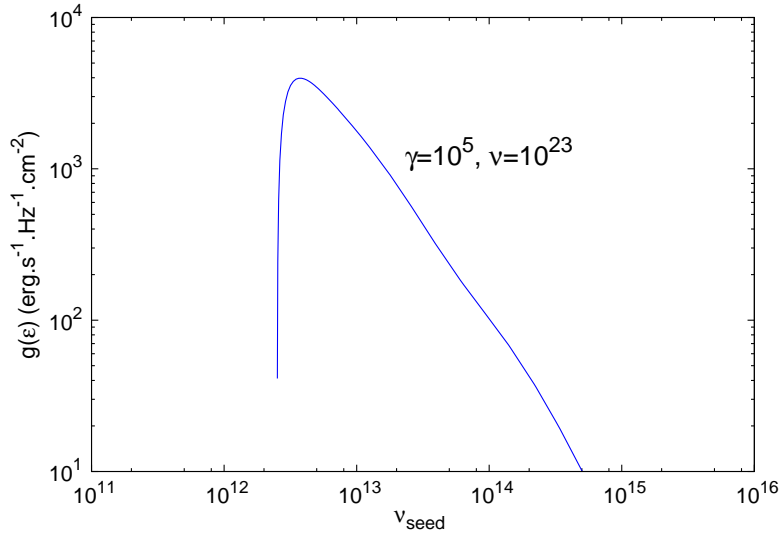


FIGURE 2.11: IC flux coming from the synchrotron seed photons for  $\gamma = 10^5$  and  $\nu = 10^{23}$ .

of  $\gamma$  values actually contribute to the IC emission. Indeed, the radio electrons number density is the highest for values around  $\gamma = 10^5$  (see fig. 2.6). Consequently, for IC frequencies such that  $10^{23} \lesssim \nu_{IC} \lesssim 10^{25}$ , electrons having  $\gamma = 10^5$  are mostly scattering off soft photons with frequencies in the infrared peak such that  $10^{13} \lesssim \nu_{IC} \lesssim 10^{15}$ . Therefore, even for the lowest frequency of the IC spectrum, radio electrons are almost not scattering the photons that they produce via synchrotron radiation.

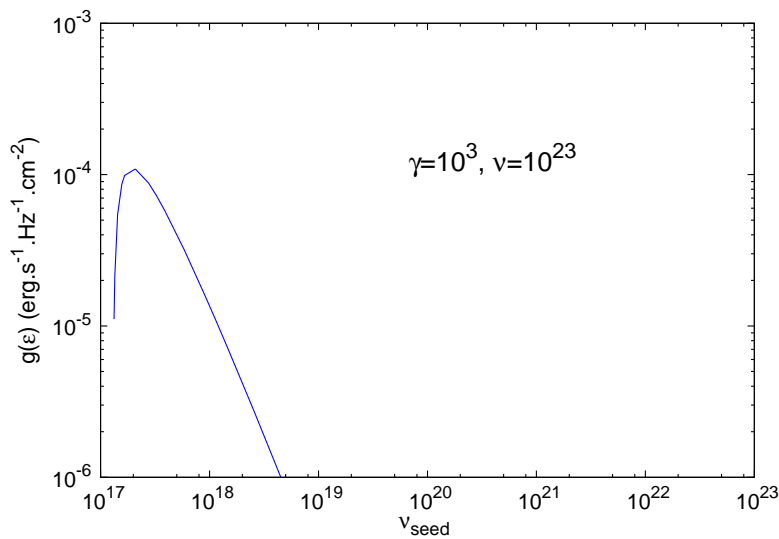


FIGURE 2.12: IC flux coming from the synchrotron seed photons for  $\gamma = 10^3$  and  $\nu = 10^{23}$ .

### 2.3.3 Scattering of the 2.7 K cosmic microwave background

The photons from the CMB are uniformly distributed within the nebula. The photon number density of the CMB,  $n_{cmb}$ , is calculated from a black body with a temperature of  $T = 2.726$  K (see Fig 2.13). When integrating over the energy, the expected number of photons per volume element is found to be:

$$\int_0^\infty n_{cmb}(\varepsilon, r) d\varepsilon \sim 411 \text{ photons cm}^{-3}. \quad (2.27)$$

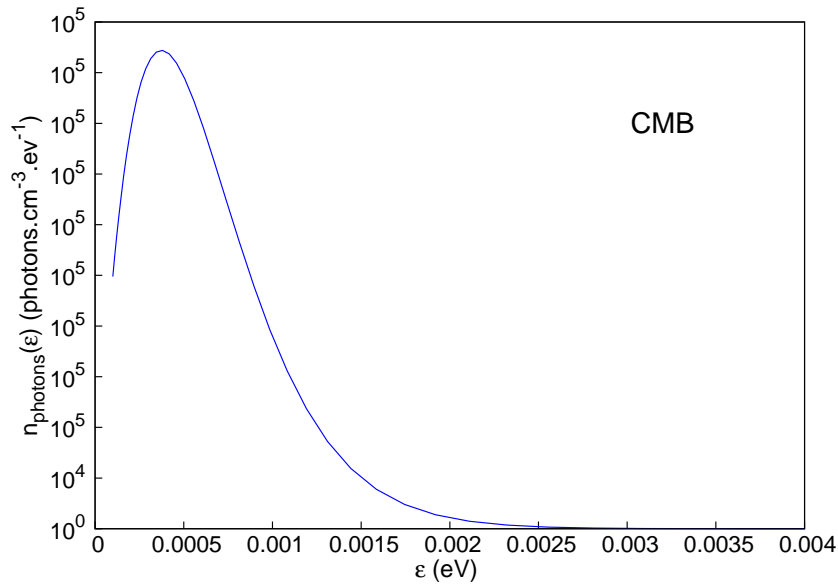


FIGURE 2.13: photon number density from the CMB in photons per cm<sup>3</sup> eV<sup>-1</sup>.



## Chapter 3

# Spectral Energy Distribution and Energy-dependent Gamma-ray Morphology of the Crab Nebula in a constant magnetic field model

In this chapter, the nebula is assumed to be homogeneously filled with a constant magnetic field. Based on the model introduced in the Chapter 2 and [Meyer et al. \(2010\)](#), the best value for the volume-averaged magnetic field is derived by fitting both the synchrotron and IC components. The magnetic field value and the electron spectra allows to calculate the resulting broad band SED of the Crab Nebula, as well as the gamma-ray morphology of the Crab Nebula in the HE-VHE range.

### 3.1 Spectral energy distribution

In that section, the calculation of the SED with a constant magnetic field model is reviewed. First, the best value of the averaged magnetic field is determined by fitting the model to the Fermi/LAT measurements. For that particular value of the magnetic field, the best parameters describing the electron spectrum are calculated.

### 3.1.1 Best value of the the average magnetic field

The synchrotron spectrum alone does not allow to infer both the energy of the electrons and the magnetic field value: a modification of the synchrotron flux induced by a variation of the magnetic field can be compensated by a change in the electron spectrum. Indeed, if  $B$  increases (respectively decreases), the synchrotron emission also increases (respectively decreases), but one can decrease (respectively increase) the electron energy such, that the synchrotron flux remain constant. If one suppose that the electron spectrum is a power law of the form:

$$\frac{dN_{el}}{d\gamma} = N_0 \left( \frac{\gamma}{\gamma_0} \right)^{-S}. \quad (3.1)$$

Equation 1.34 shows, that  $L_\nu \propto B^{(S+1)/2}$ . If the magnetic field is changed such, that  $B \rightarrow B'$ , the luminosity changes to  $L'_\nu \propto B'^{(S+1)/2}$ . However, if the normalization of the electron spectrum is modified such that

$$N_0 \rightarrow N'_0 = N_0 \sqrt{\frac{B'}{B}} \quad \text{and} \quad \gamma_0 \rightarrow \gamma'_0 = \gamma_0 \sqrt{\frac{B'}{B}}, \quad (3.2)$$

then the electron spectrum also changes like  $dN'_{el}/d\gamma = (B/B')^{(S+1)/2} dN_{el}/d\gamma$ , and the synchrotron luminosity remains constant. While the synchrotron energy depends on both the electron energy and the magnetic field strength, the IC flux depends only on the electron energy. Modelling of both emission components thus provides the magnetic field strength.

Similarly to Meyer et al. (2010), the magnetic field is determined by a  $\chi^2$  fit of the IC flux to the Fermi/LAT measurements. Fermi-LAT is better calibrated than the ground experiments, since it was absolutely calibrated with test beams at CERN before launch [Atwood et al. (2009)], whereas there is no test beam for the IACT technique. For a given magnetic field strength, the parameters of the electron spectra were derived from the fit to the synchrotron spectrum. The best-fitting parameters are determined by a least squares optimization (using the Levenberg-Marquardt method) and are shown in table 3.1. The number of degrees of freedom (d.o.f) is defined as

$$d.o.f = \text{number of data points} - \text{number of fit parameters}. \quad (3.3)$$

The resulting  $\chi^2/d.o.f = 210.6/219 \approx 0.96$  is below unity after a relative systematic uncertainty of 7% [Meyer et al. (2010)] is added in quadrature to the statistical error of the data:

$$\sigma = \sqrt{\sigma_{stat}^2 + \sigma_{sys}^2}. \quad (3.4)$$

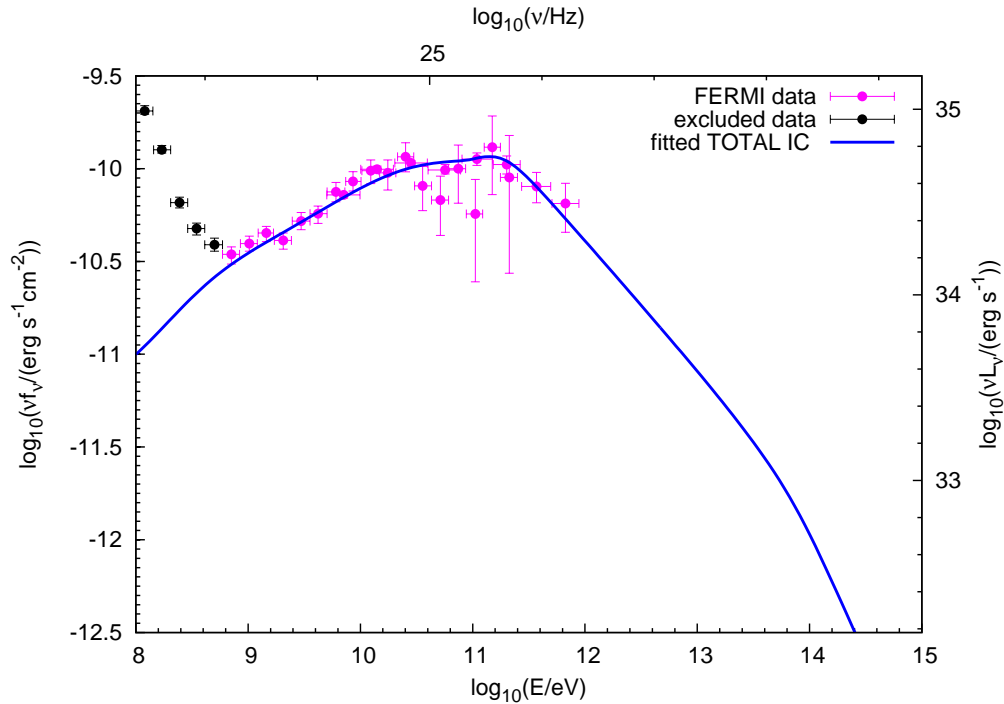


FIGURE 3.1: The predicted IC spectrum above 700 MeV used to calculate  $\chi^2(B)$  for a range of  $B$  field values using only the Fermi data. Here the IC spectrum is represented for  $B = 167 \mu\text{G}$ .

The value of  $\chi^2/d.o.f \approx 0.96$  indicates that the synchrotron emission is well described by the model. The minimization procedure is not sensitive to the particular choice of starting values and it converges reliably. Only the Fermi measurements above 700 MeV are used in the minimization procedure in order to exclude the contribution from synchrotron emission (see Fig. 3.1). A variable parameter  $B$ , and 26 data points ranging from 0.5 GeV to 671 GeV are used, resulting in a total of 25 degrees of freedom (d.o.f). The values of  $\chi^2/d.o.f$  depending on the  $B$  field are shown in Fig. 3.2. The 68.3% error (corresponding to one standard deviation) of the fit is calculated from an increase of the minimum  $\chi^2_{min}$  by  $\Delta\chi^2 = 1$ . The calculated statistical error on the  $B$  field value does not include the uncertainties resulting from the electron spectrum fitting to synchrotron data. The systematic uncertainty of the Fermi energy scale, which is assumed to be  $\Delta E/E = \begin{smallmatrix} +2\% \\ -5\% \end{smallmatrix}$  [Ackermann et al. (2012)], also results in a systematic error on the  $B$  field. Furthermore, the error depends on the chosen model, since it can not be ruled out that another model provides an equally good description. The best resulting value for the magnetic field is:

$$B = (167 \pm 6 \text{ (stat.)}_{-6}^{+15} \text{ (sys.)}) \mu\text{G}. \quad (3.5)$$

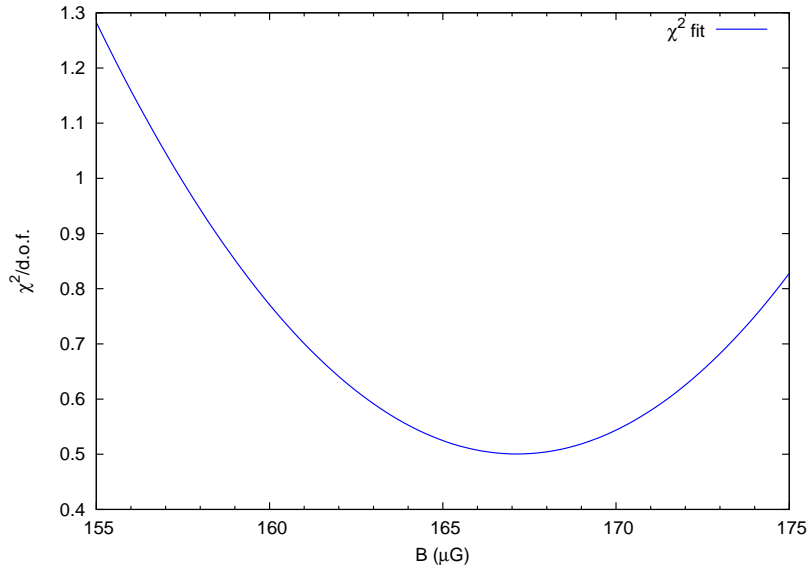


FIGURE 3.2:  $\chi^2$  minimization of the IC flux fit to the Fermi/LAT measurements by variation of the magnetic field.

The reduced  $\chi^2/d.o.f. = 12.48/25 \approx 0.50$  indicates that the statistical errors on the Fermi flux might be overestimated, the IC peak being not well described by the model.

Figure 3.3 displays the complete set of data points of the SED along with the model. The SED is plotted in double logarithmic representation as a function of the energy in eV and the frequency in Hz. The black solid line shows the entire model as the sum of its individual components. The gray solid line describes the contribution of the thermal radiation of the dust in the filaments, while the orange solid line represents the optical emission of the filaments. The red and blue dashed lines show synchrotron radiation contribution of two different electron spectra. The inverse Compton spectrum including the different seed photon fields is displayed in details in Fig. 3.4. As it can be seen, the IC flux in the high energy part ( $E \gtrsim 100$  GeV) is slightly underestimated. A  $\chi^2$ -fit of the IC flux to the Fermi/LAT and HEGRA measurements gives a reduced  $\chi^2/d.o.f. \simeq 1.13$ .

The IC flux coming from the dust is  $\sim 15$  times lower in the present model than in Meyer et al. (2010) model. This is expected, since here the dust is assumed to be located only in the outer nebula shell, whereas Meyer et al. (2010) made the assumption, that the dust follows a gaussian distribution. The lowered flux causes the magnetic field strength to be higher than the value found in Meyer et al. (2010) in order to match the Fermi data.

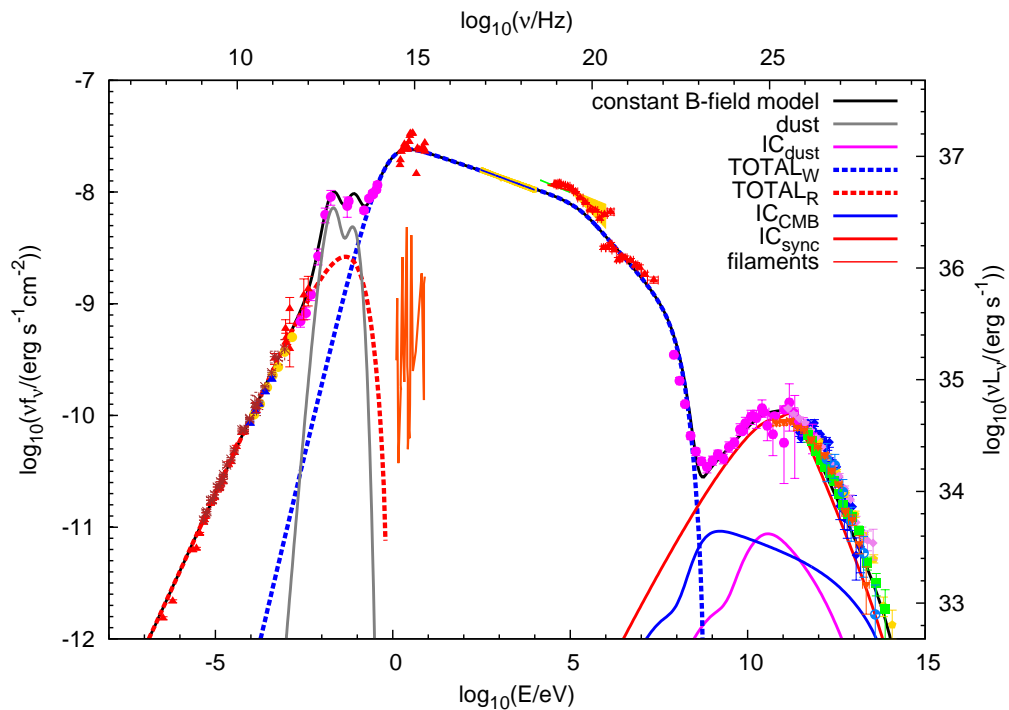


FIGURE 3.3: SED of the Crab Nebula calculated in the framework of the constant  $B$ -field model (black line). The total contribution of radio electrons to the synchrotron flux is shown (dashed red line), as well as the contribution from the wind electrons (dashed blue line). The non-thermal emission coming from the dust (gray line) and from the filaments (thin orange line) are also represented.

### 3.1.2 Electron spectra

The values of the best fit parameters of both electron populations are summarized in Table 3.1, and the spectra are shown in Fig. 3.5. The resulting covariance matrix (see Table 3.2) allows for an estimation of the correlations between different parameters. The fit-parameters are very similar to the ones obtained by Meyer et al. (2010), except for two parameters describing the wind electrons: the super exponential cut-off  $\beta$  and the wind spectral index after the break  $S + \Delta S$ . Meyer et al. (2010) previously found  $\beta = 2.80$ , and  $S + \Delta S = 3.76$ .

As expected, the radio electrons parameters are correlated with each other, especially the normalization with the spectral index ( $N_0^r; S_r$ ), and the high-energy cut-off with the normalization ( $N_0^r; \gamma_{max}^r$ ). These parameters are also correlated with the low energy cut-off of the wind electrons ( $\gamma_{max}^r; \gamma_{min}^w$ ), ( $N_0^r; \gamma_{min}^w$ ), ( $S_r; \gamma_{min}^w$ ).

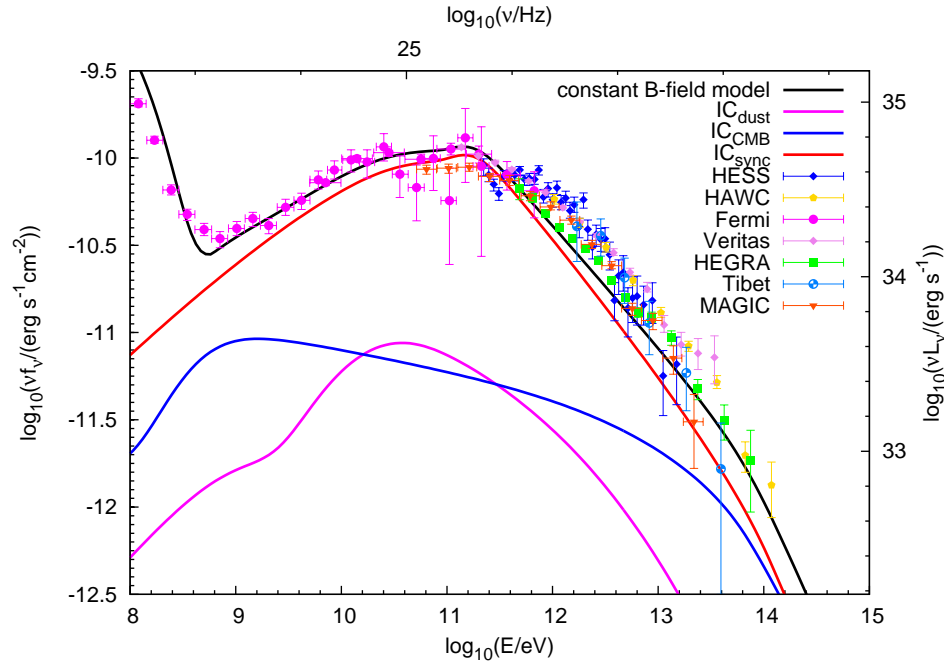


FIGURE 3.4: Contributions to the flux of inverse Compton scattering: the synchrotron radiation (red line), the thermal emission of the dust (magenta), and the CMB (blue line). The black line represents the total emission calculated in the constant  $B$ -field model.

Parameters		Radio	Wind
Normalization constant	$\ln(N_0)$	119.8	79.0
Low energy cut-off	$\ln(\gamma_{min})$	3.1	12.92
Super exponential cut-off parameter	$\beta$	-	3.99
Break position	$\ln(\gamma_{break})$	-	19.3
High energy cut-off	$\ln(\gamma_{max})$	12.2	22.5
Spectral index	$S$	1.61	3.21
Spectral index (after break)	$S + \Delta S$	-	3.72

TABLE 3.1: Parameters of the electron spectra used in the constant  $B$ -field model. At the energy  $\gamma_{min}$ , the radio electron spectrum cuts off sharply whereas the wind electrons cut off superexponentially. The energy  $\gamma_{max}$  denotes a sharp cut-off for the radio and wind electrons.

	$S_r$	$\ln(N_0^r)$	$\ln(\gamma_{max}^r)$	$\ln(\gamma_{min}^w)$	$\ln(\gamma_{break}^w)$	$\ln(\gamma_{max}^w)$	$\beta$	$S_w$	$S_w + \Delta S$	$\ln(N_0^w)$
$S_r$	1	-1.00	-0.58	-0.30	-0.02	0.01	-0.13	-0.04	-0.01	-0.02
$\ln(N_0^r)$		1	0.57	0.29	-0.02	-0.01	0.13	0.03	0.01	0.02
$\ln(\gamma_{max}^r)$			1	0.69	-0.09	-0.03	0.44	0.17	0.05	0.09
$\ln(\gamma_{min}^w)$				1	0.21	0.06	0.09	-0.35	-0.11	-0.21
$\ln(\gamma_{break}^w)$					1	0.46	0.40	-0.67	-0.83	-1.00
$\ln(\gamma_{max}^w)$						1	-0.11	-0.19	-0.67	-0.45
$\beta$							1	0.72	0.22	0.41
$S_w$								1	0.37	0.69
$S_w + \Delta S$									1	0.82
$\ln(N_0^w)$										1

TABLE 3.2: The correlation coefficients between the fit-parameters of the synchrotron spectrum. Since the matrix is symmetric, the lower trigonal part is not shown.

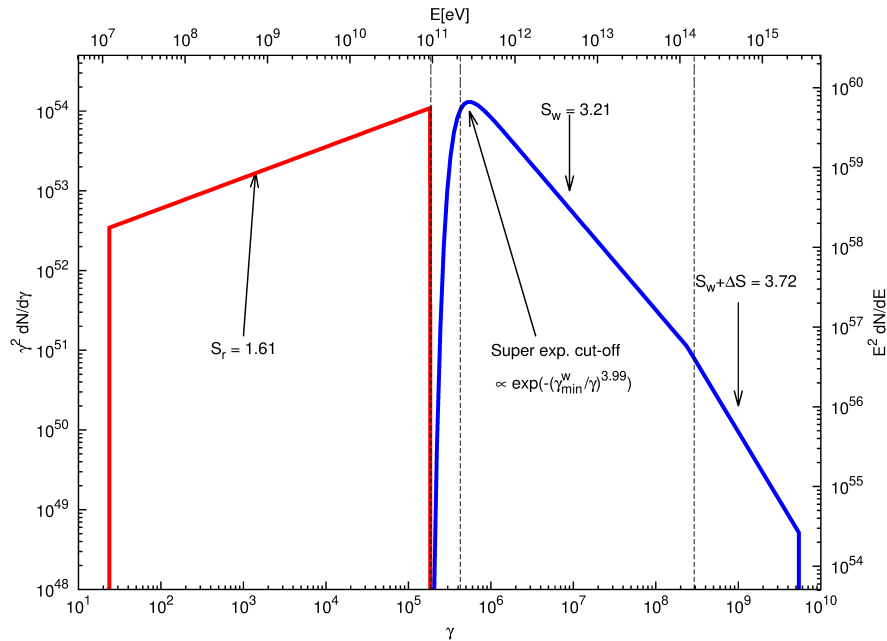


FIGURE 3.5: The two components of the electron spectrum used to calculate the broad band SED of the Crab Nebula in the constant B-field model. The radio electrons (red line) and the wind electrons (blue line) are represented. The black solid line indicates the value for the minimum, maximum and break energies.

For the wind electron spectrum, the spectral index  $S_w$  is most strongly correlated with the kink energy  $\gamma_{break}^w$ , the cut-off energy  $\gamma_{max}^w$  and the super-exponential cut-off  $\beta$ .  $S_w + \Delta S$  is most strongly correlated with  $\gamma_{break}^w$  and  $\gamma_{max}^w$ . The normalization  $N_0^w$  is most strongly correlated with the spectral indices. This is not surprising since a very similar spectrum can be modeled by adjusting these pairs of parameters to nearly equalize changes.

## Radio electrons

The spectral index of  $S_r = 1.61$  is not well compatible with the predictions of Fermi-I acceleration models, which usually have a spectral index  $p \geq 2$  (e.g. [Blandford and Eichler \(1987\)](#)). However, as seen in the previous chapter, it can be ruled out that two population of electrons are accelerated at the shock front. The mean Lorentz factor of the radioelectron is  $\bar{\gamma}_r = 3.53 \times 10^4$ , whereas the mean Lorentz factor of the wind electron is  $\bar{\gamma}_w = 2.02 \times 10^6$ . These averaged values are calculated by averaging the electron energy distribution over  $\gamma$ :

$$\bar{\gamma} = \frac{\int_{\gamma_{min}}^{\gamma_{max}} \gamma \frac{dN_{el}}{d\gamma} d\gamma}{\int_{\gamma_{min}}^{\gamma_{max}} \frac{dN_{el}}{d\gamma} d\gamma} \quad (3.6)$$

From the conservation of energy and particle flux across the shock, it follows, that the Lorentz factor of the wind electrons upstream of the shock,  $\gamma_*^w \sim 10^6$  [e.g. [Kundt and Krotscheck \(1980\)](#), [Kennel and Coroniti \(1984\)](#), [Arons \(1996\)](#)], must be approximately equal to the mean Lorentz factor of the wind  $\bar{\gamma}^w$  downstream of the shock. The Lorentz factor of the radio electrons is too low to fulfil that requirement, therefore [Atoyan \(1999\)](#) concluded, that the radioelectrons represent relic electrons, which were injected into the nebula in an early phase of high spin-down luminosity of the pulsar. The electrons lose their energy not only by synchrotron radiation, but also by adiabatic cooling, as the nebula expands further. Neglecting that contribution, the termination of the radio electron spectrum at high energies occurs only by synchrotron cooling. However, the cutoff  $\gamma_{max}^r = 1.98 \times 10^5$  is difficult to determine, since in this region, both synchrotron emissions of both electron populations and the thermal emission from the dust overlap. The lower sharp break at  $\gamma = 22.5$  (which corresponds to an energy of  $10^7$  eV) was chosen for faster calculation of the spectrum and contains no physical implications. Photons emitted by synchrotron radiation at this energy have frequencies in the range of 0.1 MHz (see Eq 1.31) for  $\langle \sin \theta \rangle = \sqrt{2/3}$ , but are not observed (see Fig. 3.3).

## Wind electrons

The wind electrons are thought to be continuously injected at the shock front into the nebula and produce, by synchrotron radiation, the major part of the spectrum beyond the submillimeter and infrared energy range. The wind electrons contribution to the synchrotron spectrum can be seen in Figure 3.3. Their electron spectrum (blue curve in Figure 3.5) exhibits a spectral index of  $S_w = 3.21 = 2.21 + 1$ , up to the kink in the spectrum at  $\gamma_{break}^w = 2.41 \times 10^8$ . This leads to a spectral index of  $\alpha = 0.61$  in the

synchrotron spectrum, and a photon index of  $\Gamma = 2.11$  (see Table 1.3) in accordance with the index measured by XMM-Newton [Kirsch et al. (2005)]. The spectral index agrees well with the predictions of the Fermi 1st order acceleration section of an ultrarelativistic shock with subsequent synchrotron cooling.

The kink at  $\gamma = \gamma_{break}^w$  corresponds to the change of the spectrum at hard X-rays, at  $\sim 130$  keV, the spectral index changes by  $\Delta S = 0.53$ . The origin of this feature in the electron spectrum must be related to the acceleration and/or injection of the particles. It can hardly be attributed to an energy-dependent escape of the particles from the nebula, since the electrons in the X-ray region lose their energy by synchrotron radiation, well before escaping the nebula.

## 3.2 Extension

Until recently, the morphology of the Crab Nebula was only resolved up to energies of about 80 keV [Hester (2008), Madsen et al. (2015)]. At higher energies, no spatial extension could be determined, mostly due to the insufficient angular resolution of the instruments. For a telescope like H.E.S.S. for example, the expected size of the Crab Nebula in the high energy range is several times smaller than the point spread function (PSF) of the instrument. In such a case, the extension of the source broadens the signal only slightly as compared to the PSF, which itself greatly depends on the current observations and instrument conditions. The H.E.S.S. [?] and Fermi collaborations [Ackermann et al. (2018)] have recently published estimates of the angular size of the nebula in the VHE energy range. H.E.S.S. unveiled, that the Crab Nebula is extended at TeV  $\gamma$ -ray energies with a root-mean-square width of  $52''$ . The Fermi collaboration found the 68% containment radius ( $R_{68}$ ) of the Crab Nebula to be  $R_{68} = (0.030 \pm 0.003 \text{ (stat)} \pm 0.007 \text{ (sys)}) \text{ deg}$ . Using the Fermi/LAT and H.E.S.S. measurements, Yeung and Horns (2019) estimated  $R_{68} = (0.0330 \pm 0.0025 \text{ (stat)}_{-0.0075}^{+0.0012} \text{ (sys)}) \text{ deg}$ . They found the energy-dependent Crab Nebula's  $\gamma$ -ray extension to be  $R_{68} \propto E_{IC}^{-\alpha}$ , with  $\alpha = 0.155 \pm 0.035 \text{ (stat)} - 0.037 \text{ (sys)}$ . Here, the modelling of the angular extension of the Crab Nebula is compared to the actual measurements.

### 3.2.1 Definition of the Intensity

In this subsection, the definition of the intensity is introduced and it is explained how this quantity allows to infer the angular size of the nebula. The *specific intensity*  $I_\nu$  is

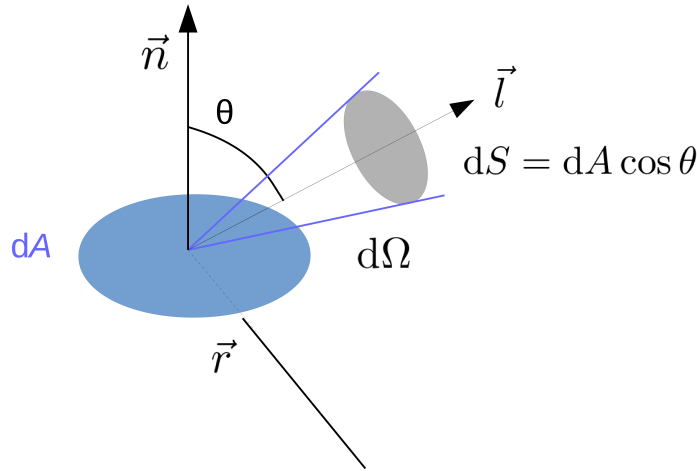


FIGURE 3.6: Representation of the quantities used to define the intensity (see text for more details).

defined as the proportionality coefficient  $I_\nu$  in:

$$dE_\nu \equiv I_\nu(\vec{r}, \vec{l}, t)(\vec{l} \cdot \vec{n})d\nu dA dt d\Omega = I_\nu(x, y, z, \theta, \varphi, t)d\nu dt dA \cos\theta d\Omega, \quad (3.7)$$

where  $dE_\nu$  is the quantity of energy transported through the surface  $dA$  with  $\vec{n}$  the normal to  $dA$ , at the location  $\vec{r}$ , between times  $t$  and  $t + dt$ , in the frequency band between  $\nu$  and  $\nu + d\nu$ , and in the solid angle  $d\Omega$  along the direction  $\vec{l}$  (see Fig. 3.6). The total intensity  $I$ , is obtained by integrating over all possible frequencies:

$$I = \int_0^\infty I_\nu d\nu \quad (3.8)$$

### Difference between Flux and Intensity

The flux is the net rate of energy flowing across a unit area (e.g., at a detector), *from all directions*, per unit time, per unit frequency interval, which, in terms of intensity means:

$$f_\nu = \int_\Omega \int_\theta I_\nu \cos\theta d\Omega. \quad (3.9)$$

The essential difference between the specific Intensity  $I_\nu$  and the flux  $f_\nu$  is that the specific intensity is independent of the distance from the source (but requires the source to be resolved), while the flux falls off as  $r^{-2}$ . The energy emitted towards (and received

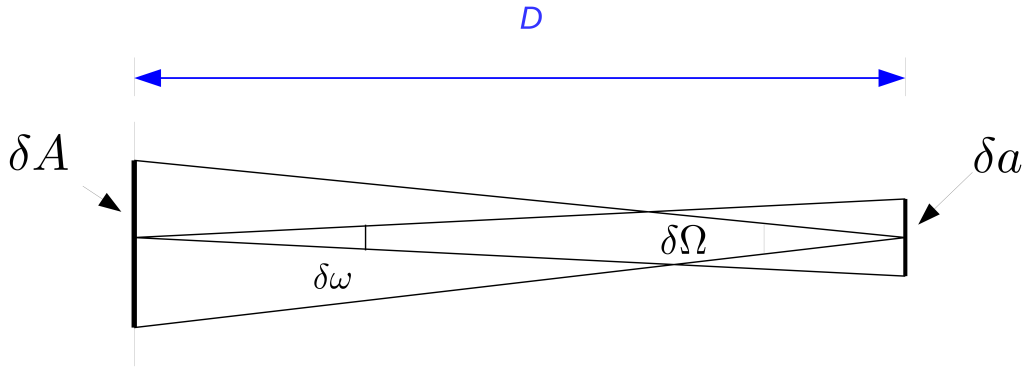


FIGURE 3.7: Let  $\delta A$  be some area on a source at a distance  $D$  subtending a solid angle  $\delta\Omega$  at a detector; while the detector of area  $\delta a$ , subtends a solid angle  $\delta\omega$  at the source.

by) the detector is (see Fig. 3.7):

$$E = I_\nu \delta A \delta\omega$$

$$\Leftrightarrow \frac{E}{\delta\Omega} = I_\nu D^2 \frac{\delta a}{D^2},$$

with  $\delta A = D^2 \delta\Omega$  and  $\delta\omega = \delta a / D^2$ . The terms  $D^2$  cancel out, and one can see that the energy received *per unit solid angle* is independent from the distance. A source must be spatially resolved for the observers to be able to measure the intensity, otherwise, only the flux can be measured. If a source is called *unresolved*, it means that it is much smaller in angular size than the point-source response telescope observing it. If the source is unresolved, the direction of the Poynting vector of the observed radiation cannot be identify.

### Radiative transfer equation

The intensity along a beam is constant, except if local emission or absorption processes add photons or remove photons from it. Providing that such processes occur (requiring the presence of matter), the local intensity gain and the local intensity loss are defined with empirical proportionnality constant, similarly to the definition of the intensity.

**Emissivity** The local addition of photons to a beam of radiation is proportionnal, in the infinitesimal limit, to the number of emitting particles, to the time interval  $dt$ , the frequency bandwidth  $d\nu$ , and the solid angle  $d\Omega$  over which the beam is measured:

$$dE_\nu \equiv j_\nu dV dt d\nu d\Omega, \quad (3.10)$$

with  $dE_\nu$  the energy added in the form of photons to a beam with solid angle  $d\Omega$ , during a time  $dt$ , over bandwidth  $d\nu$ , within the volume  $dV$ . Units of  $j_\nu$ : [ $\text{erg cm}^{-3}\text{s}^{-1}\text{Hz}^{-1}\text{ster}^{-1}$ ]. The emissivity coefficient,  $j_\nu$ , depends on location, direction, time and frequency as well as the intensity  $I_\nu$ . Let us consider a beam with a cross-section  $dA$ , crossing a volume  $dV = dA ds$  while propagating along a path  $ds$ . The amount of intensity added by local emission to a beam with intensity  $I_\nu$  is:

$$dI_\nu = j_\nu(s)ds. \quad (3.11)$$

### Extinction coefficient

Similarly, the number of photons removed from a beam by extinction processes is proportionnal to both the supply of photons and the number of extinguishing particles in the infinitesimal limit. This relation of proportionality is defined as the *extinction coefficient*. The monochromatic extinction coefficient (effective cross-section),  $\sigma_\nu$  per particle, with the units [ $\text{cm}^2$ ], is:

$$dI_\nu \equiv -\sigma_\nu n I_\nu ds. \quad (3.12)$$

with  $n$  the density of the absorbing particles [ $\text{cm}^3$ ]. The extinction per unit path length is:

$$dI_\nu \equiv -\alpha_\nu I_\nu ds, \quad (3.13)$$

with  $\alpha_\nu = \sigma_\nu n$  the monochromatic linear extinction coefficient with the units [ $\text{cm}^{-1}$ ].

### Transport equation

Let us consider a small cylinder with length  $ds$  and sides  $dA$ , oriented along a beam of radiation with intensity  $I_\nu$ . If we consider a constant emissivity  $j_\nu$  and a constant extinction coefficient from  $s$  to  $(s + ds)$ , the total intensity variation is:

$$dI_\nu(s) = I_\nu(s + ds) - I_\nu ds = j_\nu(s)ds - \alpha_\nu I_\nu ds. \quad (3.14)$$

$$\frac{dI_\nu(s)}{ds} = j_\nu - \alpha_\nu I_\nu. \quad (3.15)$$

This is the *transport equation*. It applies most of the time, except when the extinguishing particles are not small with respect to the space between them, or when they are not randomly distributed over the medium. In the case where the medium in which the beam propagates is optically thin, one has  $\alpha_\nu = 0$ . Here, the Crab Nebula is assumed

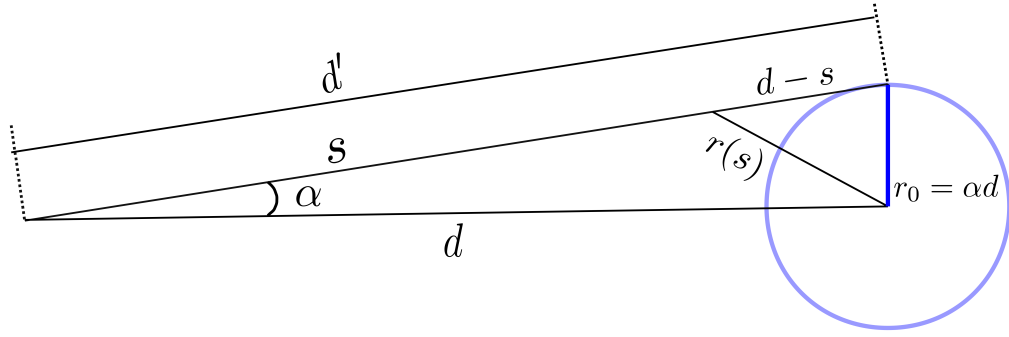


FIGURE 3.8: Representation of the Crab Nebula (blue circle) located at a distance  $d$  from us. The line of sight is denoted by  $s$ , and  $\alpha$  represents the angular size of the Crab Nebula. See text for more details.

to be optically thin. The inverse Compton intensity is then computed via:

$$dI_\nu = j_\nu^{IC}(r(s))ds. \quad (3.16)$$

### 3.2.2 Calculation of the intensity

The calculation of the intensity is done by integrating the emissivity along the line of sight:

$$I_\nu(\alpha) = \int_0^\infty j_\nu(r)ds, \quad (3.17)$$

where  $s$  is the line of sight, and the inverse Compton and Synchrotron emissivity are given by (see Chapter 2):

$$j_\nu^{IC} = \frac{1}{4\pi} \int_\gamma d\gamma \frac{3\sigma_{TC}}{4} \frac{h^2\nu}{\gamma^2} \int_{h\nu/4\gamma^2}^{h\nu} \frac{d\varepsilon}{\varepsilon} f_{IC}(\varepsilon, \nu, \gamma) n_{seed}(r, \varepsilon) n_{el}(\gamma, r), \quad (3.18)$$

$$j_\nu^{Sy} = \frac{1}{4\pi} \int_\gamma d\gamma n_{el}(\gamma, r) \sqrt{\frac{2}{3}} \frac{\sqrt{3}e^3 B \nu}{mc^2} \frac{\nu}{\nu_c} \int_{\nu/\nu_c}^\infty K_{5/3}(x) dx. \quad (3.19)$$

The angular size of the Crab Nebula is denoted by  $\alpha$ ,  $d = 2$  kpc is the distance between the Crab Nebula and the Earth, and  $r$  is of the order of magnitude of the Crab Nebula radius (see Fig. 3.8). The size of the Crab Nebula is much smaller than the distance from the Earth to the nebula:

$$r \ll d. \quad (3.20)$$

The assumption of  $r \ll d$  is justified, because the size of the Crab Nebula itself ( $r \approx 4$  pc) in relation to the distance to us as observer ( $d \approx 2000$  pc) provides a sufficiently accurate description of the situation, since

$$\left(\frac{r}{d}\right) = \frac{4 \text{ pc}}{2000 \text{ pc}} = \frac{2}{1000} \ll 1. \quad (3.21)$$

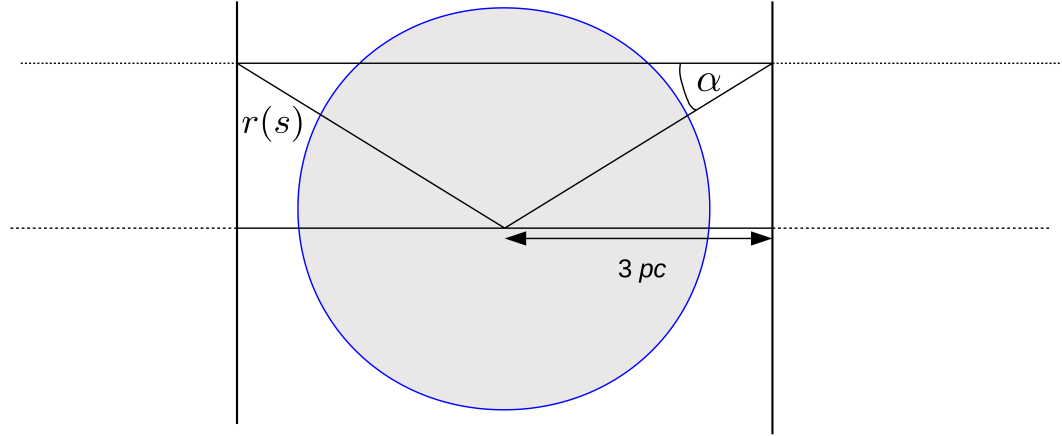


FIGURE 3.9: The Crab Nebula is represented by the blue circle. Here the approximation  $d \simeq d'$  is made. The area between the two vertical lines represents the region where the emissivity is non-zero. See text for more details.

As a result to the small angle approximation,

$$\alpha = \tan\left(\frac{r_0}{d}\right) \simeq \frac{r_0}{d} \iff r_0 = \alpha d. \quad (3.22)$$

The equations 3.18 and 3.19 are expressed in function of  $r$ , and thus should be rewritten in function of  $s$ . One should first show that, at the first order,  $d' \simeq d$  holds. The following relationship between  $d'$ ,  $d$  and  $r_0$  applies (see Fig. 3.8)

$$d' = \sqrt{d^2 + r_0^2} = d\sqrt{1 + \left(\frac{r_0}{d}\right)^2} \simeq d\left(1 + \frac{r_0^2}{2d^2}\right) + o\left(\frac{r_0}{d}\right)^4. \quad (3.23)$$

Therefore, the line of sight can be considered to be perpendicular to  $r_0$ . One obtain:

$$r^2(s) = (d - s)^2 + r_0^2 = (d - s)^2 + (\alpha d)^2 \iff r(s) = \sqrt{(d - s)^2 + (\alpha d)^2}. \quad (3.24)$$

The Synchrotron and IC emissivities are null outside of the Crab Nebula (see Fig. 3.9):

$$j_\nu(r(s)) = \begin{cases} j_\nu(r(s)) & \text{if } d - l < r < d + l, \\ 0 & \text{else,} \end{cases}$$

where the distance  $l = 3 \text{ pc}$  is chosen such that the intensity varies by less than 0.01%. The integral between 0 and  $\infty$  can be replaced by an integrale over the area where the

emissivity is non-zero:

$$I_\nu(\alpha) = \int_0^\infty j_\nu(r(s))ds \approx \int_{d-l}^{d+l} j_\nu(r(s))ds. \quad (3.25)$$

This approximation allows to reduce the numerical computation time.

### 3.2.3 Verification of the model

#### Spectral Energy Distribution

In order to verify the validity of the calculation, several tests are performed. First, the SED of the Crab Nebula is recalculated by integrating the calculated Intensity over the solid angle (see Eq. 1.4):

$$f_\nu = \frac{L_\nu}{4\pi d^2} = \int I_\nu(\alpha)d\Omega = 2\pi \int d\alpha \sin(\alpha)I_\nu(\alpha). \quad (3.26)$$

The integral is approximated by a simple trapezoidal integration:

$$f_\nu = 2\pi \int d\alpha \sin(\alpha)I_\nu(\alpha) = 2\pi \sum_{i=0}^{n=33} \frac{\Delta\alpha}{2} (\sin(\alpha_i + 1)I_\nu(\alpha_{i+1}) + \sin(\alpha_i)I_\nu(\alpha_i)). \quad (3.27)$$

This is sufficient to check that the magnitude and the shapes obtained are in agreement with the expected SED: as can be seen in Fig. 3.10, the luminosity calculated by integration over the solid angle matches the SED well.

#### Size of the synchrotron nebula

The calculation of the synchrotron size is here compared to theoretical predictions. The synchrotron extension is calculated in the following way, combining equations 3.19 and 3.17

$$j_{Sy}(r(s), \nu) = \frac{1}{4\pi} \int_\gamma d\gamma n_{el}(\gamma, r) \frac{\sqrt{3}e^3 B \sin\theta}{mc^2} \frac{\nu}{\nu_c} \int_{\nu/\nu_c}^\infty K_{5/3}(x)dx. \quad (3.28)$$

It follows from Eq. 3.16 that:

$$I_\nu^{Sy}(\alpha) = \int_0^\infty ds j_{Sy}(r(s), \nu). \quad (3.29)$$

As discussed already (Chapter 1, subsubsec. 1.3.3), a “single” electron with a Lorentz

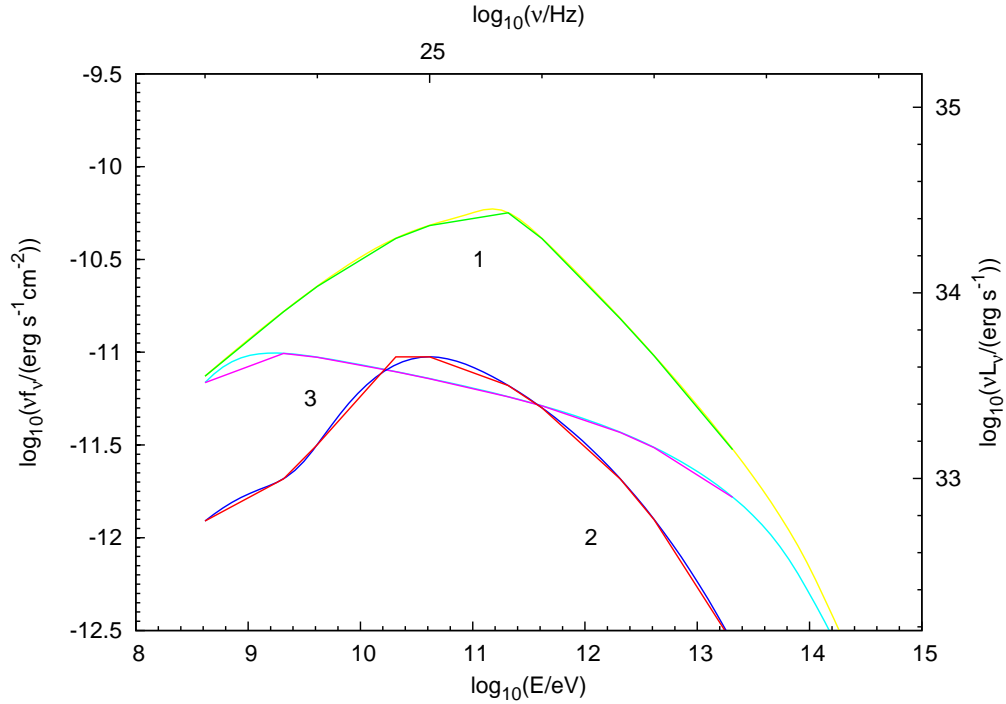


FIGURE 3.10: Comparison between the IC fluxes calculated in the constant  $B$  –  $field$  model (smooth lines) and the IC fluxes obtained by integration of the calculated intensity over the solid angle (broken lines). The contributions from the different seed photon fields are shown: (1) synchrotron, (2) thermal dust, (3) CMB.

factor  $\gamma$  emits most of its synchrotron radiation at the characteristic frequency  $\nu_c$ . Therefore, the Bessel function can be replaced by a “delta-function approximation”

$$\frac{\nu}{\nu_c} \int_{\nu/\nu_c}^{\infty} K_{5/3}(x) dx = \delta(\nu - \nu_c) = \delta(\nu - \nu_0 \gamma^2) = \frac{\delta\left(\gamma - \sqrt{\frac{\nu}{\nu_0}}\right)}{2\nu_0 \sqrt{\frac{\nu}{\nu_0}}}, \quad (3.30)$$

where we have used the property of the delta distribution when it is composed with a smooth function  $g$ :

$$\delta(g(x)) = \frac{\delta(x - x_0)}{|g'(x_0)|}. \quad (3.31)$$

Furthermore, the electron spectrum is a power-law (see Chapter 2, subsection 2.2.4):  $\frac{dN_{el}}{d\gamma} \propto \gamma^\beta$ . Using the equation 3.24,

$$I_\nu^{Sy}(\alpha) = \frac{1}{4\pi} \frac{\sqrt{3}e^3 B \sin \theta}{mc^2} \int_0^\infty ds \int_\gamma d\gamma \gamma^{-\beta} \delta(\nu - \nu_c) e^{-\frac{(d-s)^2 + (\alpha d)^2}{2\rho^2(\gamma)}}. \quad (3.32)$$

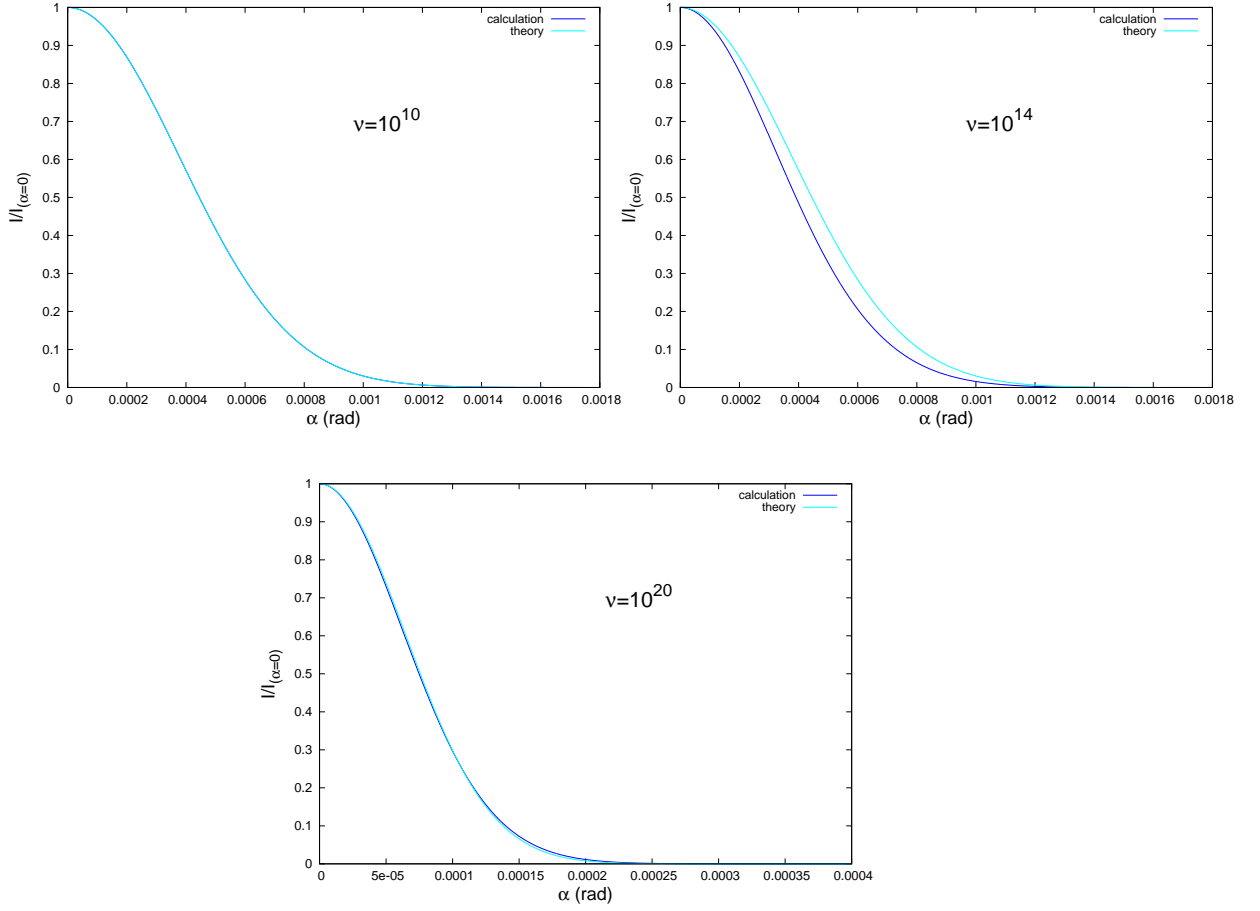


FIGURE 3.11: Normalized synchrotron intensity calculated within the constant B-field model (blue line) in comparison to the expected intensity in the delta approximation (light blue line) for different values of  $\nu$ . Both contributions from radio and wind electrons are taken into account.

It should be noted that the equation above is valid only if  $g(x) = 0$  for  $x = x_0$ , i.e., there is only one root. After integrating over  $\gamma$ , one gets:

$$I_{\nu}^{Sy}(\alpha) = \frac{1}{4\pi} \frac{\sqrt{3}e^3 B \sin \theta}{mc^2} e^{\frac{-(\alpha d)^2}{2\rho^2 \sqrt{\nu/\nu_0}}} \int_0^{\infty} ds \frac{\left(\sqrt{\nu/\nu_0}\right)^{-\beta}}{\beta + 1} e^{\frac{-(\alpha d)^2}{2\rho^2 \sqrt{\nu/\nu_0}}} \frac{1}{2\nu_0 \sqrt{\frac{\nu}{\nu_0}}}. \quad (3.33)$$

Normalizing  $I_{\nu}^{Sy}(\alpha)$  by  $I_{\nu}^{Sy}(\alpha = 0)$ , eliminates the constant term and the integrals over  $s$ :

$$\frac{I_{\nu}^{Sy}(\alpha)}{I_{\nu}^{Sy}(\alpha = 0)} = e^{\frac{-(\alpha d)^2}{2\rho^2 \left(\sqrt{\frac{\nu}{\nu_0}}\right)}}. \quad (3.34)$$

The calculated synchrotron intensity follows the intensity expected in the delta approximation, as shown in Fig. 3.11. However, for values of  $\nu \sim \nu_{break}$ , there is a small disparity between the calculation and the values obtained in the delta approximation (see Fig. 3.11, top right plot). This effect is directly due to the “delta approximation”: for values of  $\nu$  such that  $\nu \lesssim \nu_{break}$  (resp.  $\nu \gtrsim \nu_{break}$ ), the averaged value of  $\rho$  over  $\gamma$  will be smaller (resp. bigger) than in the delta approximation, since  $\rho(\nu < \nu_{break}) > \rho(\nu > \nu_{break})$ . For the radio electrons, the intensities calculated in both the delta approximation and the model, are similar, since the scale length  $\rho$  of the radio electrons is constant (as they are not cooling) (see Fig. 3.11, top left plot). Therefore, when averaged over frequencies  $\nu$  near  $\nu_c$ , we obtain the same average value of  $\rho$  as in the case of the delta approximation. For the wind electron, the intensities calculated in the model and in the delta approximation are almost the same, indeed, for  $\rho(\nu < \nu_c) < \rho(\nu_c)$  and  $\rho(\nu > \nu_c) > \rho(\nu_c)$  (see Fig. 3.11, bottom plot). Therefore, the averaged value of  $\rho$  will be roughly compensated.

### Size of the IC nebula for CMB seed photons

A “single” electron with Lorentz factor  $\gamma$  being scattered by a uniform photon distribution emits most of its IC radiation at photons with a characteristic energy  $E_{\gamma m}$  [(Blumenthal and Gould, 1970)]. Therefore, similarly to the synchrotron intensity calculation, a delta function approximation is introduced in addition to a “monochromatic approximation”, where it is considered that one electron is scattered by photons with a fixed energy  $\varepsilon_0$  [e.g., Schlickeiser (2002)]. In the Thomson limit

$$\langle \varepsilon_{\gamma} \rangle = \frac{4}{3} \varepsilon_0 \gamma^2, \quad (3.35)$$

gives an estimate of the energy of the “monochromatic” IC photons emitted by the electron. The monochromatic photon energy is taken such that  $\varepsilon_0 = \langle \varepsilon_{CMB} \rangle \sim 10^{-3}$  eV. Similarly to the synchrotron intensity calculation:

$$\frac{I_{\nu}^{IC}(\alpha)}{I_{\nu}^{IC}(\alpha=0)} = e^{-\frac{(\alpha d)^2}{2\rho^2 \left( \sqrt{\frac{\nu}{\nu_{IC}}} \right)}}, \quad (3.36)$$

where  $\nu_{IC} = (4/3h)\varepsilon_0$  (see Eq. 3.35) represents the IC critical frequency. The IC intensities calculated in the model and with the delta approximation are shown in Fig. 3.12 for two values of the frequency:  $\nu = 10^{23}$  and  $\nu = 10^{25}$ .

### Qualitative description of the intensity shapes

The figure 3.14 displays the IC flux calculated within the model for two values of the frequency for each photon field. This agrees with the SED of the Crab Nebula (see

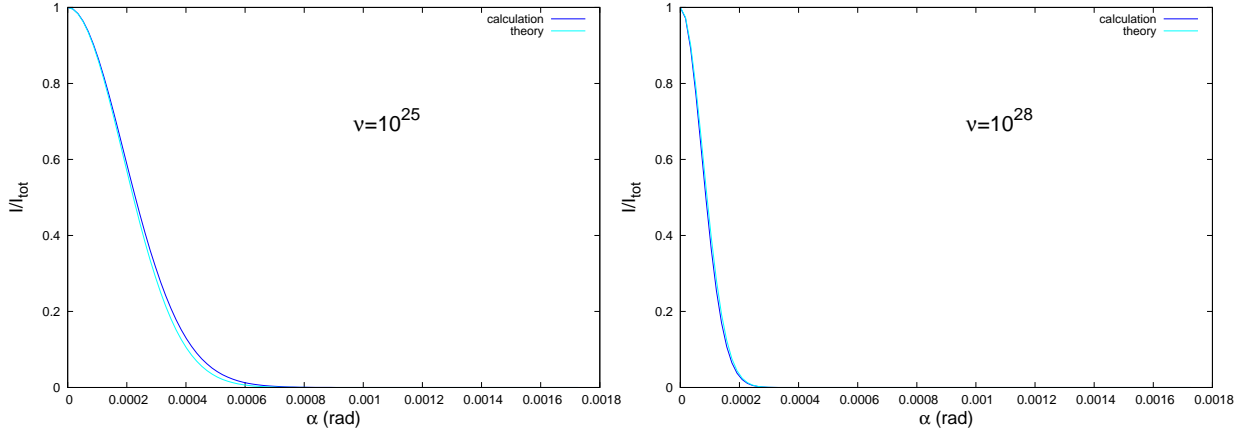


FIGURE 3.12: The IC intensity for the CMB photons calculated within the constant B-field model (blue line) normalized to the intensity for  $\alpha = 0$  compared with the expected intensity in the delta approximation (light blue line) for two different values of  $\nu$ .

section 3.1, Fig. 3.4): for a given frequency, the synchrotron intensity is dominating the two other components and for a given component, the width of the intensity is decreasing with the frequency as it is expected due to the cooling of the electrons. The fraction of synchrotron intensity and the fraction of dust intensity are higher for  $\nu = 10^{25}$  than for  $\nu = 10^{23}$ , while it is the opposite for the CMB (also shown in the SED figure). It should be noted that the fraction of the intensity at  $\alpha = 0$  cannot be directly compared to the flux. Indeed, for a given seed photon field component  $i$ , the corresponding luminosity fraction can be expressed by:

$$\frac{L_{\nu}^i}{L_{\nu}^{tot}} = \frac{\int I_{\nu}^i(\alpha) d\Omega}{\sum_{j=1}^3 \int I_{\nu}^j(\alpha) d\Omega}, \quad (3.37)$$

$\forall \{i, j\} \in \{1, 2, 3\}^2, i \neq j$ , where the index  $i, j$  represent the different seed photons field. Equation 3.37 can be factorized by  $I_{\nu}^i(0)$ :

$$\frac{L_{\nu}^i}{L_{\nu}^{tot}} = \frac{I_{\nu}^i(0) \int g_{\nu}^i(\alpha) d\Omega}{\sum_{j=1}^3 I_{\nu}^j(0) \int g_{\nu}^j(\alpha) d\Omega}. \quad (3.38)$$

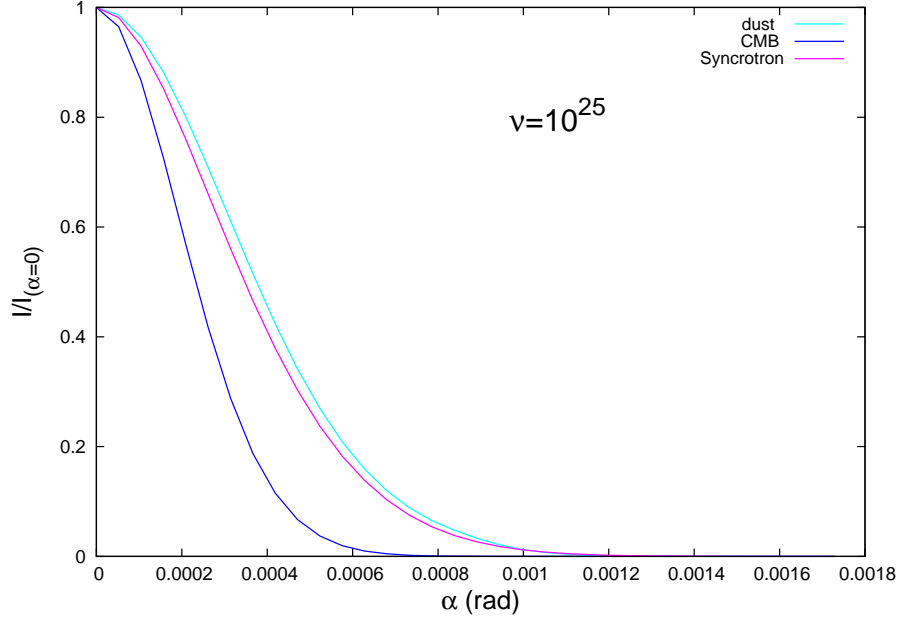


FIGURE 3.13: Intensity  $I$  normalized over the intensity at  $\alpha = 0$ ,  $I(\alpha = 0)$  for the three different seed photons fields.

In the case where the function  $g_\nu^i$  is the same for the three components, one as:

$$\frac{L_\nu^i}{L_\nu^{tot}} = \frac{I_\nu^i(0) \int g_\nu(\alpha) d\Omega}{\sum_{i=1}^3 I_\nu^i(0) \int g_\nu(\alpha) d\Omega} = \frac{I_\nu^i(0)}{I_\nu^{tot}}. \quad (3.39)$$

But as it can be seen in Fig. 3.13, the shapes of the intensity are not the same, therefore:

$$\frac{L_\nu^i}{L_\nu^{tot}} \neq \frac{I_\nu^i(0)}{I_\nu^{tot}}. \quad (3.40)$$

### 3.2.4 Comparison with the Data

In order to compare the results with [Yeung and Horns \(2019\)](#) and [Holler et al. \(2017\)](#), the 68% containment radius,  $R_{68}$  of the Crab Nebula has been determined for different energy bands. The 68% containment radius is defined as the radius corresponding to 68% of the total flux

$$0.68 f_\nu^{max} = \int_0^{R_{68}} I_\nu(\alpha) d\Omega, \quad (3.41)$$

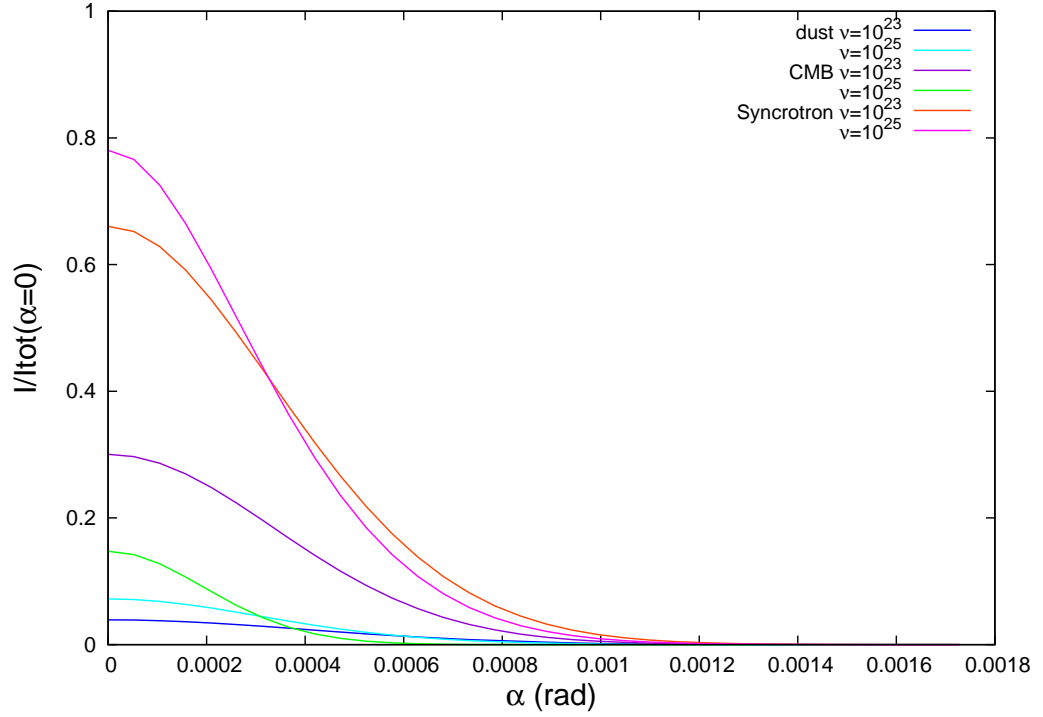


FIGURE 3.14: Intensity  $I$  normalized over the total intensity at  $\alpha = 0$ ,  $I_{tot}(\alpha = 0)$  and calculated for  $\nu = 10^{23}$  and  $\nu = 10^{25}$ .

with the maximal flux  $f_{\nu}^{max}$

$$f_{\nu}^{max} = \int_0^{\alpha_{max}} I_{\nu}(\alpha) d\Omega, \quad (3.42)$$

$\alpha_{max} = 0.1 \text{ deg} \equiv 3.5 \text{ pc}$  is taken to be larger than the size of the Crab Nebula in order to not underestimate the total flux. Integral 3.42 is determined by a trapezoidal integration:

$$f_{\nu} = 2\pi \int d\alpha \sin(\alpha) I_{\nu}(\alpha) = 2\pi \sum_{i=0}^{n=33} \frac{\Delta\alpha}{2} (\sin\alpha_{i+1} I_{\alpha_{i+1}} + \sin\alpha_i I_{\alpha_i}). \quad (3.43)$$

A trapezoidal integration is precise enough since the estimated error on the integration  $\eta$  is found to be:

$$\varepsilon = |f_{\nu,rectangle} - f_{\nu,trapezoid}| \approx 10^{-8} \text{ erg s cm}^{-2}, \quad (3.44)$$

where  $f_{\nu,rectangle}$  and  $f_{\nu,trapezoid}$  represent the fluxes  $f_{\nu}$  calculated with the rectangle and trapezoidal methods, respectively. The function  $I_{\nu}$  is evaluated in 34 points, which

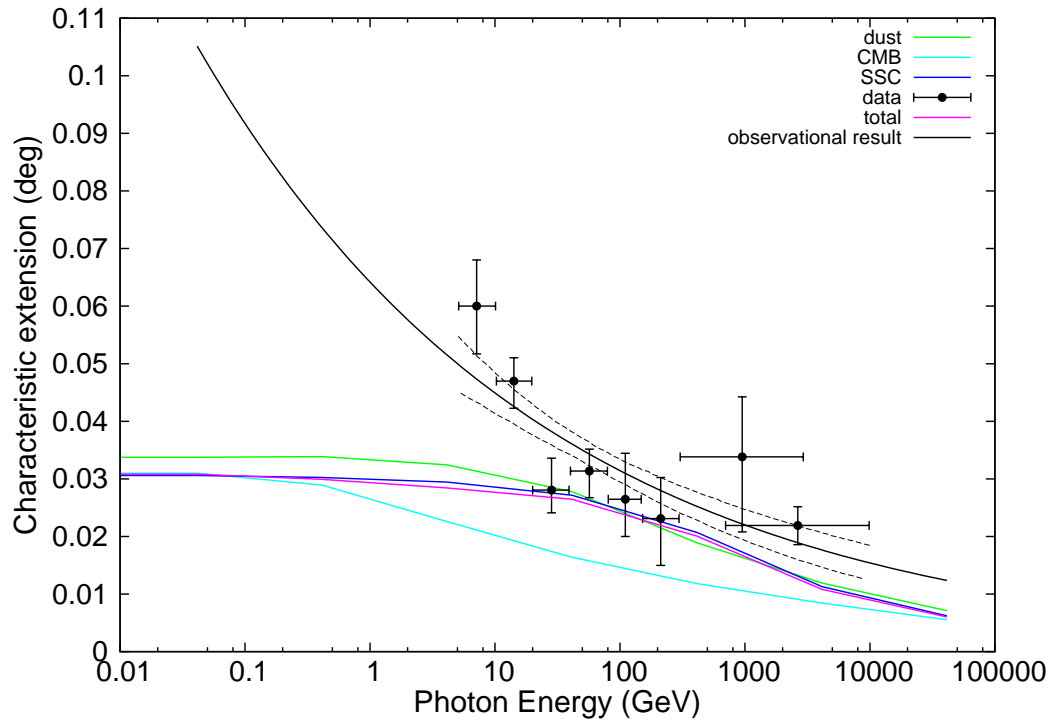


FIGURE 3.15: Energy-dependence of the observed extension (black) and theoretical predictions based on various seed-photon fields (dark blue for CMB, cyan for dust, green for synchrotron-self-Compton (SSC) and red for total seed-photon field). The characteristic extension is defined by equation 3.41. The data are from [Yeung and Horns \(2019\)](#), except the last measurement which is taken from [Holler et al. \(2017\)](#).

is sufficient since the functions do not vary much. The 68% containment radius  $R_{68}$  is shown in Fig. 3.15, together with the data from [Yeung and Horns \(2019\)](#) and [Holler et al. \(2017\)](#). One can see, that the estimated total extension is overall smaller than the measurements, especially for the two first energy bins. In particular for values of photons  $E_\gamma \lesssim 10$  GeV, there is a flattening of the three components, corresponding to the confinement of the electrons in the radio nebula (see the definition of  $\rho$ , Chapter 2, subsection 2.2.2). However, the flattening is not observed in the measurements. For energies  $\lesssim 100$  GeV, the characteristic size of the emission coming from the dust is dominating the other components. This is expected, as photons coming from the dust are located in a shell around the radio nebula and are more likely to interact with the radio electrons. The total extension is very closed to the SSC extension, as the flux of photons scattered by SSC is dominant over the other components (see Fig. 3.3).

### 3.3 Conclusion

The constant  $B$ -field model reproduces well the synchrotron emission but underestimates the IC flux in the high energy regime ( $E \gtrsim 100$  GeV). Furthermore, it fails to describe satisfactorily the  $\gamma$ -ray extension. This is not surprising, since the scattered flux depends on the field strength  $B$  as  $B^{-(S+1)/2}$  (given an electron spectral index of  $S$ ). Therefore, as already suggested by MHD models, a more detailed treatment of the magnetic field structure is required to explain for both the IC emission and the gamma-ray extension of the Crab Nebula.



## Chapter 4

# Modelling of the Crab Nebula with a varying magnetic field

Higher extension measurements of the Crab Nebula in the low-energy range of the IC emission can be explained by two hypothesis. First, as indicated by MHD models, the magnetic field in the nebula is not indefinitely constant-as assumed in a constant  $B$ -field model-but starts to decrease after several  $r/r_s$ , and becomes nul at the edge of the nebula. This causes the escape of the electrons, supposedly confined in the radio nebula in the constant  $B$ -field model. Furthermore, an interesting feature described in [Bietenholz and Kronberg \(1990\)](#) shows that the magnetic field tends to be radial at the edge of the nebula, favoring a rapid escape of the electrons. The other explanation is be that the unseen outer shell (see chapter 1, subsect. 1.1.2) of the Crab Nebula could be actually visible in the Fermi/LAT data. This is the last hypothesis which is chosen here to derive the parameters describing the varying magnetic field, and recalculate the SED accordingly.

### 4.1 Magnetic field structure

This magnetic field in the nebula is described by MHD propagation of the magnetized plasma of relativistic electrons injected at the wind shock into the nebula [[Rees and Gunn \(1974\)](#)]. [Kennel and Coroniti \(1984\)](#) have refined this model by deriving 1-D MHD flow solutions. The magnetic field behaviour and the MHD flow of the relativistic plasma in the nebula are characterized by the “magnetization-” or “ $\sigma$ -parameter”, defined to be the ratio of the electromagnetic energy flux to the particle energy flux at the wind shock

$$\sigma = \frac{B_s^2}{4\pi n u \gamma m c^2}, \quad (4.1)$$

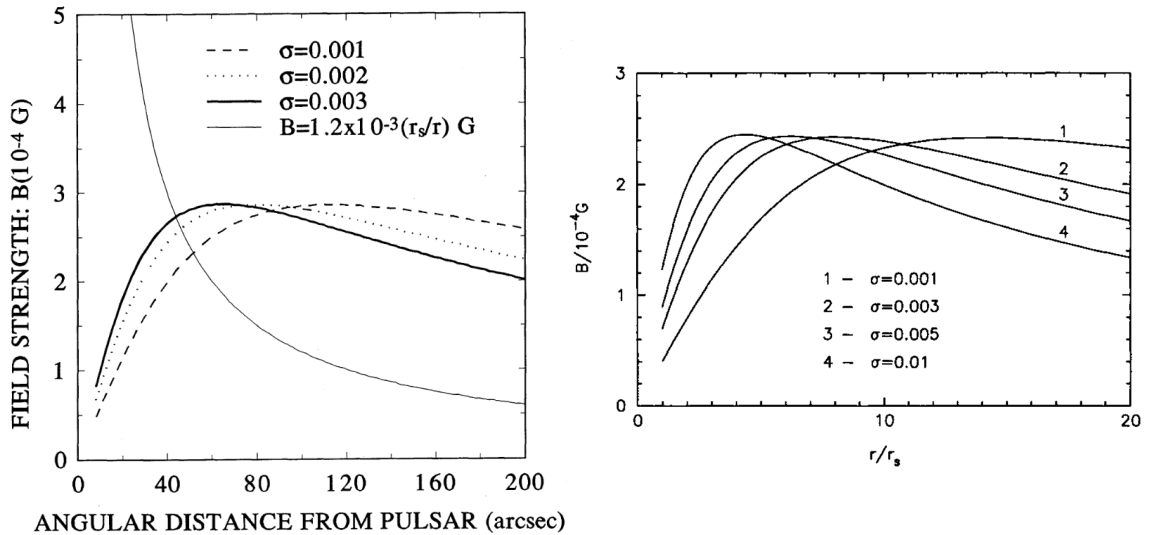


FIGURE 4.1: The magnetic field in the Crab Nebula at different distances  $r$  (right panel) and angular distances (left panel) for different values of the parameter  $\sigma$  in the framework of the MHD model of KC;  $r = r_s$  corresponds to the distance of the wind termination shock from the pulsar. The left plot is taken from [de Jager et al. \(1996\)](#) and the right plot from [Atoyan and Aharonian \(1996a\)](#).

where  $B_s$  is the shock frame magnetic field,  $n$  is the density and  $u$  is the radial four-speed of the relativistic electron flow at the shock. According to [Rees and Gunn \(1974\)](#),  $\sigma \ll 1$  just ahead of the shock. For such small values of  $\sigma$ , the magnetic field strength would be a minimum at the shock radius,  $r_s$ , where the ram pressure from the pulsar wind is balanced by the external pressure. For  $r \geq r_s$ , the magnetic field increases with  $r$  as  $B(r) \propto r$  (see Fig. 4.1). The description of the regime where the magnetic field starts to decrease and becomes nul remains largely unknown.

Under the assumption that electrons coming from the outer shell of the nebula are producing additional IC emission, the radio electrons should “see” a greater magnetic field than the wind electrons, in order to let room in the SED for the new component. Therefore, the magnetic field is modeled by a step function such that (see Fig. 4.2):

$$B = \begin{cases} B_1 & \text{for } r < r_{radio} \\ B_2 & B_2 > B_1, \text{ for } r_{radio} < r < r_{cut} \\ 0 & \text{else.} \end{cases} \quad (4.2)$$

The radius  $r_{cut}$  at which the magnetic field becomes nul is such that  $r_{cut} = 300$  arcsec and is chosen to be a bit larger than the size of the nebula. It permits to not suffer any synchrotron losses, and therefore preserve the observed the radio nebula radius,

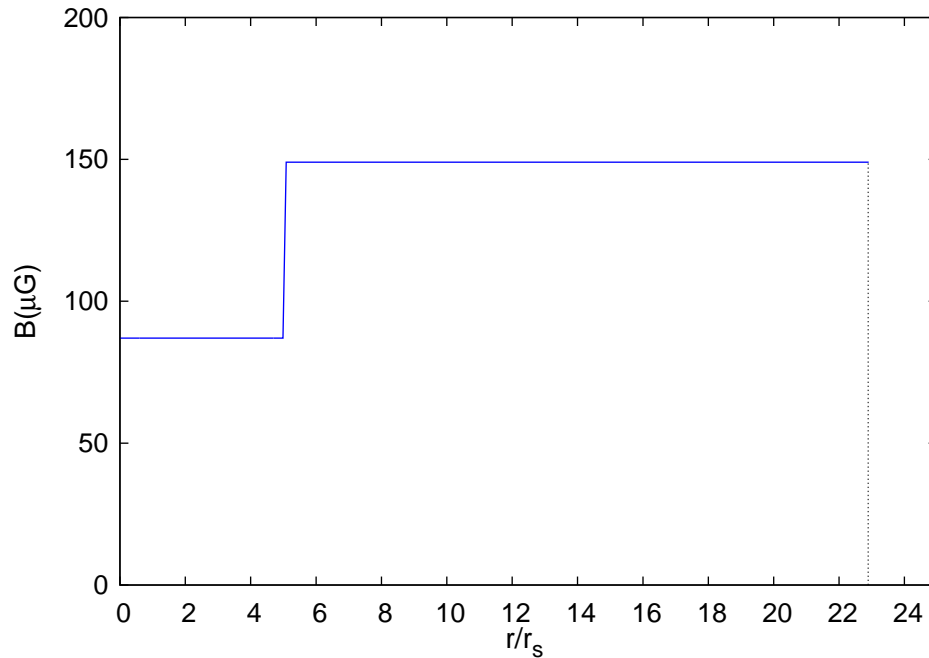


FIGURE 4.2: Magnetic field  $B$  used in the calculations. The value of the magnetic field is  $B_1 = 87 \mu\text{G}$  for  $(r/r_s \lesssim 5)$  and then jump to  $B_2 = 149 \mu\text{G}$ , it is decreasing to 0 for  $r/r_s \gtrsim 23$ .

$r_{radio}$ , defined by  $r_{radio} = d \tan \theta_{radio}$  (with  $\theta_{radio} = 78$  arcsec, see chapter 2, subsection 2.2.2).

Fig. 4.3 shows the effect of the magnetic field on the synchrotron spectrum before adjusting the electron spectra parameters. As expected, the flux is reduced for  $10^{15} \lesssim \nu \lesssim 10^{22}$ , corresponding to the wind electrons contribution to the synchrotron flux. As the magnetic field is lower in the region  $r < r_{radio}$ , where the wind electrons are located, they will produce less synchrotron emission. Consequently, the decrease of the magnetic field in the region  $r < \theta_{radio}$  from previously  $B = 167 \mu\text{G}$  to a smaller value lowers the IC spectrum produced by the wind electrons, as can be seen in Fig. 4.4. The IC spectrum produced by radio electrons is mainly due to soft photons having frequencies in the infrared peak of the Crab Nebula (see Chapter 2, subsect. 2.3.2). This could explain why the contribution of radio electrons to the IC spectrum is also smaller than in the case of a constant magnetic field. Furthermore, for  $\nu_{IC} \sim 10^{25}$ , the radio electrons contributions in the cases of a constant and a varying magnetic field tend to have the same cutoff energy. These electrons are going to scatter mostly seed photons with frequencies  $\nu_{seed} \sim 10^{13}$  (see Eq. 2.25), which seem to not be affected by the magnetic field decrease.

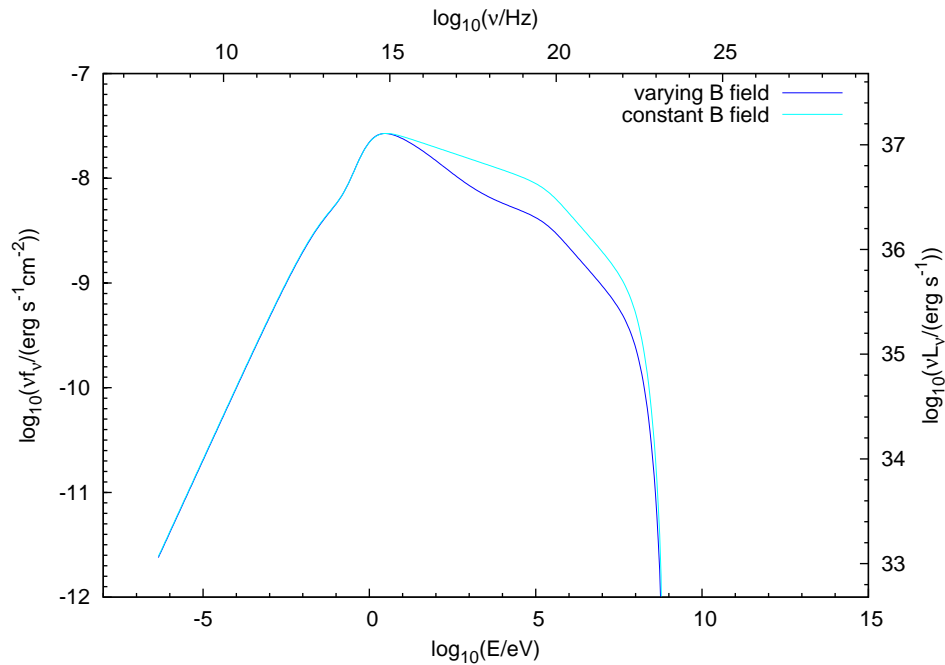


FIGURE 4.3: Synchrotron spectrum represented in the case of the constant  $B$ - field model (light blue line) and in the case of a varying magnetic field (blue line). Here  $B_1 = 80 \mu\text{G}$  and  $B_2 = 250 \mu\text{G}$ .

## 4.2 Best fitting parameters for the varying magnetic field

The total extension  $S$  in the low energy regime  $E \lesssim 10 \text{ GeV}$  should be  $S \sim 0.06 \text{ deg}$  [Yeung and Horns (2019), see Fig. 3.15]. Let  $f_1$  and  $f_2$  be the fluxes from the electrons confined in the nebula, and the electrons located at the outer edge of the nebula respectively. Their corresponding extension are denoted  $s_1$  and  $s_2$ . The total extension  $S$  can be expressed in function of  $f_1$ ,  $f_2$ ,  $s_1$  and  $s_2$  by

$$S^2 = \frac{f_1 s_1^2 + f_2 s_2^2}{f_1 + f_2} = \frac{f_1 s_1^2 + (1 - f_1) s_2^2}{f_1 + f_2}, \quad (4.3)$$

with  $f_1 + f_2 = 1$ , the total flux. The IC extension due to electrons confined in the radio nebula,  $s_1$  is such that  $s_1 \sim 0.03 \text{ deg}$  (see model, Fig. 3.15). The outer radius of the outer blast wave is unknown, therefore, a maximum outer shell radius value,  $s_2 \lesssim 0.2 \text{ deg}$ <sup>1</sup> is assumed. The electrons present in the supposedly outer shell would produce the missing IC emission with a flux  $f_2$ . A lower limit on the IC flux produced by the radio electrons

<sup>1</sup>The value of  $s_2$  is simply obtained by considering an expansion velocity of  $v \simeq 1680 \text{ km.s}^{-1}$  for the ejecta multiplied by the age of the nebula.

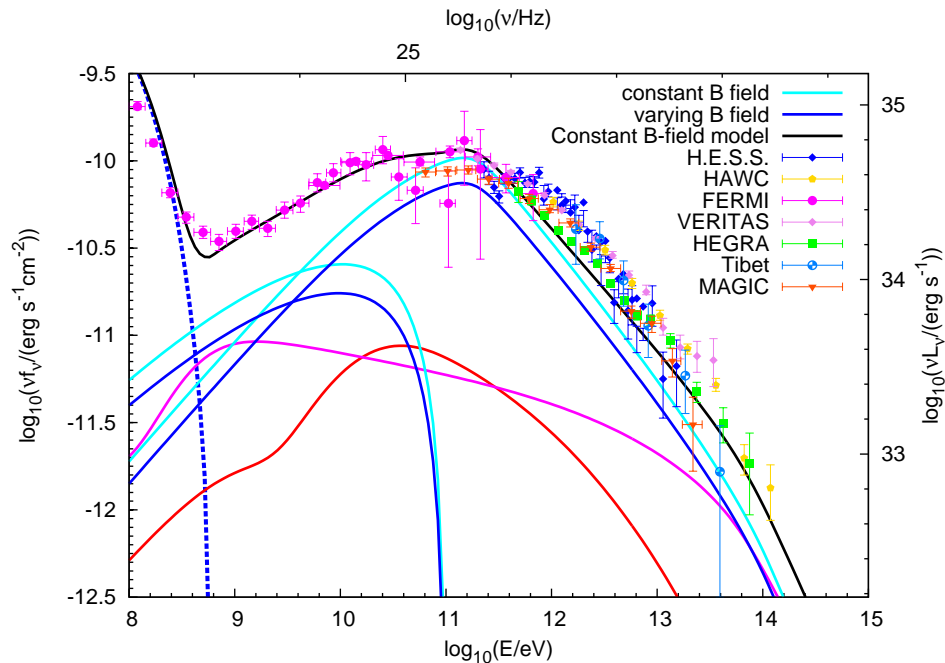


FIGURE 4.4: Contributions to the flux of inverse Compton scattering: the synchrotron radiation in the constant  $B$ -field model (red line) and after varying the magnetic field, the thermal emission of the dust (magenta line), and the CMB (blue line).

can be estimated:

$$f_1 = \frac{S^2 + s_2^2}{s_1^2 - s_2^2}, \quad (4.4)$$

where  $f_1$  is found to be  $f_1 \sim 0.93$ . The best value of  $B_1$  is obtained by a  $\chi^2$  fit of the IC flux to the Fermi/LAT measurements multiplied by  $f_1$ , for frequencies such that  $\nu < 10^{25}$  (this corresponds approximately contribution of radio electrons to the IC flux). The best value of  $B_2$  is found by a  $\chi^2$  fit of the IC flux to the Fermi/LAT and HEGRA measurements (see Fig. 4.5). The best fitting parameters are  $B_1 = (87 \pm 4 \text{ (stat.)}_{-6}^{+15} \text{ (sys.)}) \mu\text{G}$ , and  $B_2 = (149 \pm 6 \text{ (stat.)}_{-6}^{+15} \text{ (sys.)}) \mu\text{G}$  with  $\chi^2/\text{d.o.f.} = 36.89/38 \simeq 0.97$ . The high energy part of the IC flux ( $E \gtrsim 100 \text{ GeV}$ ) is best described with a varying magnetic field. Furthermore, with a constant magnetic field model, it was previously found  $\chi^2/\text{d.o.f.} \simeq 1.13$  for the fit of Fermi/LAT and HEGRA measurements. The resulting inverse Compton spectrum including the different seed photon fields is displayed in details in Fig. 4.6. The choice of fitting the model to HEGRA measurements is motivated by its small statistical uncertainties compared to other IACTs.

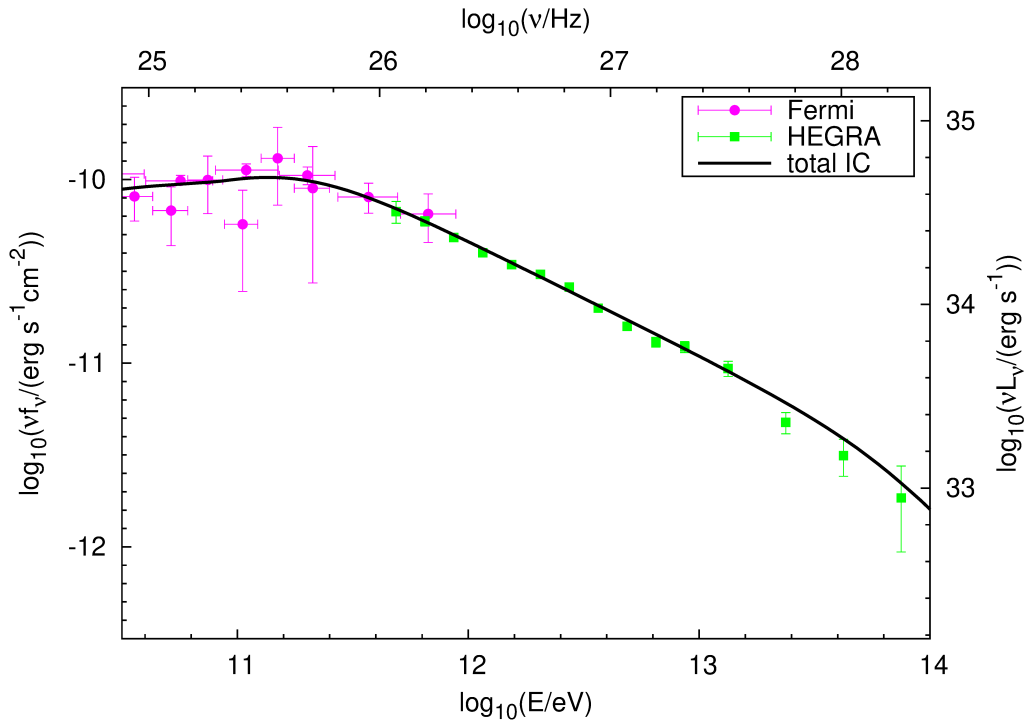


FIGURE 4.5: The IC model (constant  $B$ -field model, solid black line) is adjusted to the measurements from MAGIC and Fermi/LAT.

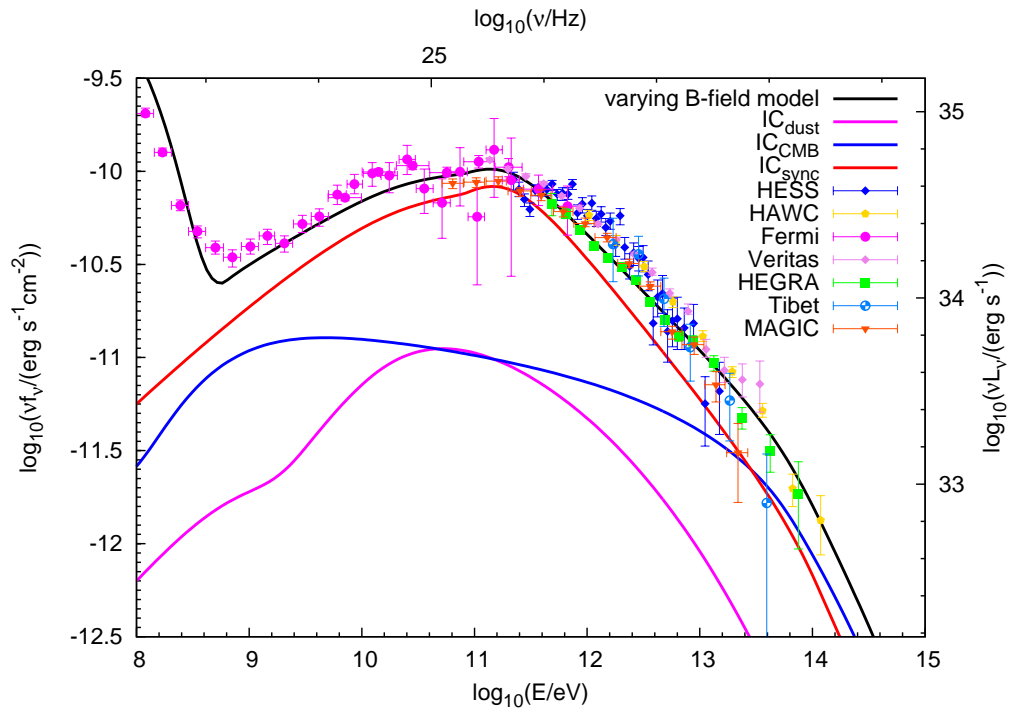


FIGURE 4.6: Contributions to the flux of inverse Compton scattering: the synchrotron radiation (red line), the thermal emission of the dust (magenta line), and the CMB (blue line). The black line represents the total emission calculated in the current  $B$  field step model.

### 4.3 Cross calibration of IACTs and Fermi

Aharonian et al. (2004b) have shown that observational methods can already achieve a stable ( $< 6\%$ ) and accurate calibration ( $+5/-10\%$ ) of the absolute energy scale (Meyer et al. (2010)), as well as inter-calibration of multiple telescopes with an accuracy of  $2\%$  [Hofmann (2003)]. The usual method for calibrating the energy scale with observational methods consists in matching carefully the observed cosmic-ray event rate with the simulated event rate (taking the detector and its performance into account) [see e.g Pühlhofer et al. (2003), Lebohec and Holder (2003)]. Corrected energy-dependent collection areas from Monte-Carlo simulations can be calculated by determining the variations of the energy scale. The method has been demonstrated to work for observations on the Crab nebula covering five years [Aharonian et al. (2004b)]. The energy spectrum (flux and shape) remain stable for years after corrections of time-dependent effects and shifts in the energy scale (which change by as much as  $20\%$ ). Indeed, the remaining variations of the observed integral flux after corrections indicate that the calibration of the energy scale varies by less than  $6\%$  from year to year [Aharonian et al. (2004a)]. It should be noted, that the expected variations of the flux from the Crab nebular are the same in magnitude. Therefore, the quoted  $6\%$  should be considered as an upper limit on the achievable stability of the energy calibration. Even though the relative changes in the energy scale are already quite small after correcting for variations in the detector and atmosphere, the absolute energy scale remains to be determined accurately.

Meyer et al. (2010), have used the inverse-Compton component of the energy spectrum from the Crab nebula to cross-calibrate the Fermi-LAT flux measurements with ground-based flux measurements. Their analysis showed that the relative shift of the energy scale among ground based telescopes is smaller than the estimated systematic uncertainty of the instruments at that time ( $15\%$ ). Since their work, new measurements are available (see Chapter 1, section 1.2), therefore, the varying  $B$ -field model is used to derive scaling factors. The cross calibration between the imaging air Cherenkov telescopes H.E.S.S., HEGRA and MAGIC and Fermi/LAT is achieved in the following way: the average magnetic field is fitted to the Fermi/LAT measurements (see section 3.1.1). For each IACT, an energy scaling factor is applied to adjust the measured energy  $E_{meas}$  to a common energy scale  $E$  such that

$$E = E_{meas} \cdot s_{IACT} \quad (4.5)$$

The scaling factor  $s_{IACT}$  for each instrument is determined by a  $\chi^2$ -minimization in which the energy scale  $s_{IACT}$  is varied according to the formula above until the data best matches the model.

Instrument	Scaling factor $S_{IAC T}$	Statistical error $\Delta s$	$\chi^2_{before}/d.o.f$	$\chi^2_{after}/d.o.f$
Fermi/LAT	1.00	+0.05 -0.03	-	0.97
HEGRA	1.00	$\pm 0.1$	-	0.97
MAGIC	1.02	$\pm 0.01$	0.9	0.8
H.E.S.S.	0.96	$\pm 0.02$	6.70	1.38
Tibet	1.0	$\pm 0.1$	2.91	2.91
HAWC	0.90	$\pm 0.03$	0.88	0.48
VERITAS	0.938	$\pm 0.003$	14.68	6.34

TABLE 4.1: Energy scaling factors of the IACTs used for the cross calibration.

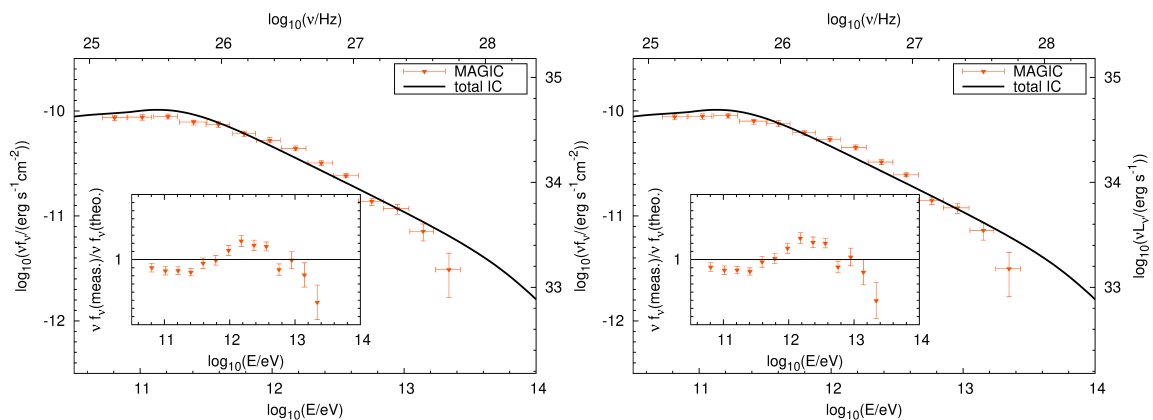


FIGURE 4.7: Left panel: The IC model (constant  $B$ -field model, solid black line) with measurements from MAGIC and Fermi/LAT. No energy scaling is applied. Right panel: The same curve as in the left panel but with the scaling factor  $s = 1.02$  applied to the data.

The derived scaling factors for the different instruments are listed in table 4.1 with their statistical errors. For each instrument, the comparison between the unscaled and scaled data points with the model is represented in Fig. 4.7, Fig. 4.8, Fig. 4.9, Fig. 4.10 and Fig. 4.11. The scaling factors are applied, according to equation 4.5. It is clear from these figures that the scaled data points fit the model better. This is also confirmed by the  $\chi^2$ -value before and after the application of the scaling factors. All scaling factors lie within the aforementioned 15% energy uncertainty of the IACTs. Meyer et al. (2010) found similar values for the scaling factors of H.E.S.S. and MAGIC. Values of  $\chi^2$  smaller than 1 are due to bin correlations.

This method is also suitable to any other experiment measuring the flux from the Crab Nebula in the high-energy range. IACTs suffer from systematic uncertainties which are currently estimated to be around 15% [Gaug (2017)].

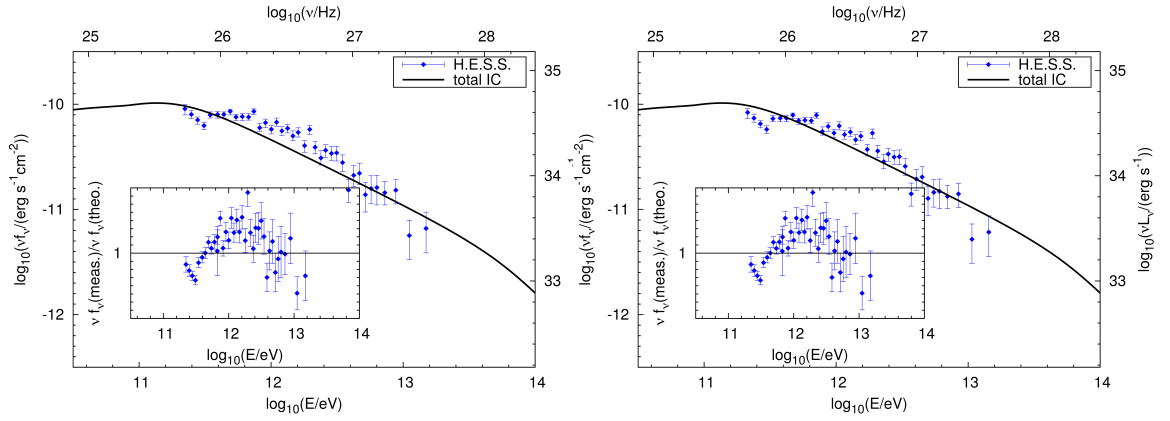


FIGURE 4.8: Left panel: The IC model (constant  $B$ -field model, solid black line) with measurements from H.E.S.S and Fermi/LAT. No energy scaling is applied. Right panel: The same curve as in the left panel but with the scaling factor  $s = 0.96$  applied to the data.

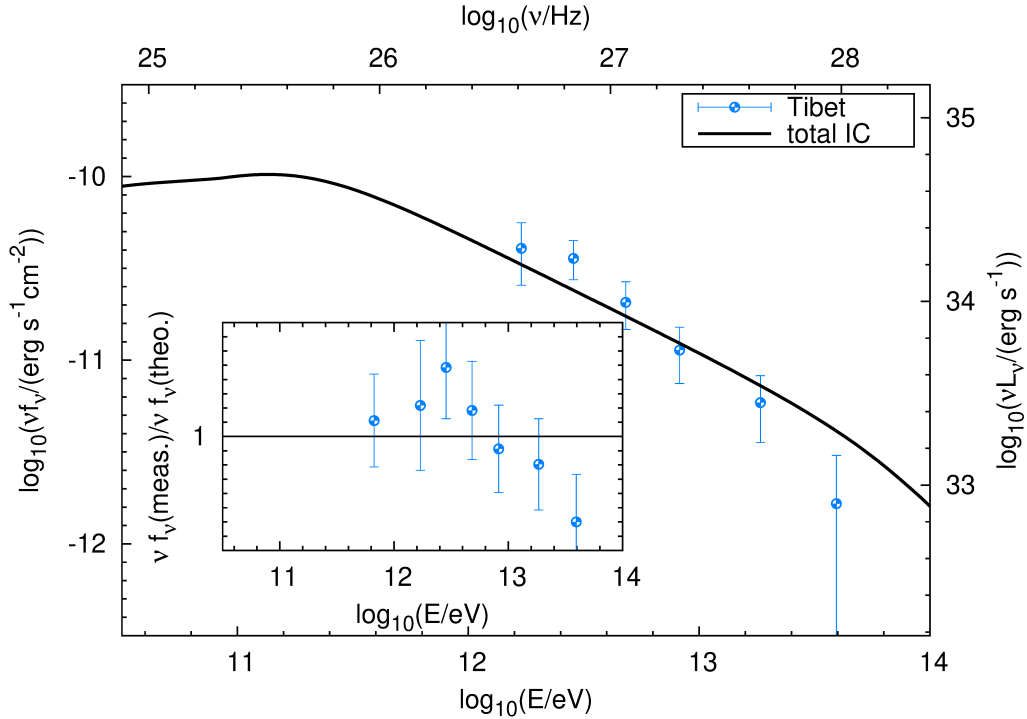


FIGURE 4.9: The IC model (constant  $B$ -field model, solid black line) with measurements from Tibet and Fermi/LAT. No energy scaling is applied.

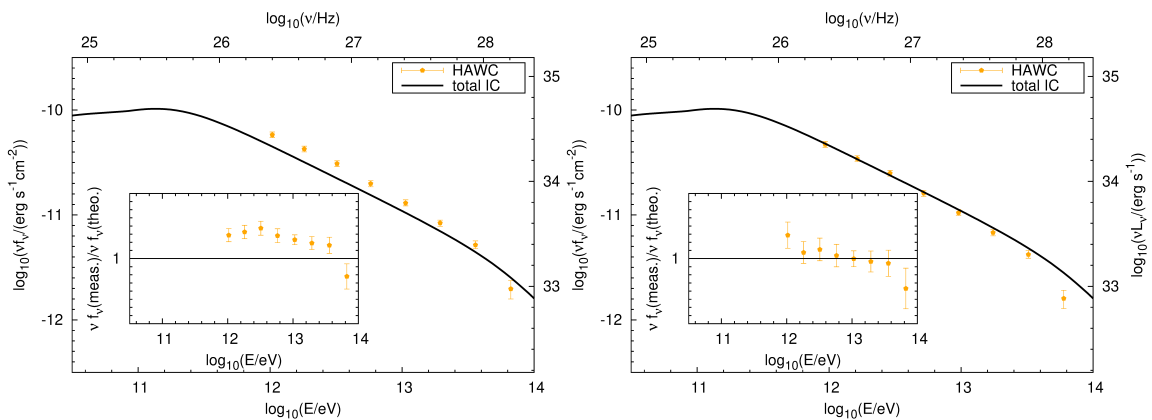


FIGURE 4.10: Left panel: The IC model (constant  $B$ -field model, solid black line) with measurements from HAWC and Fermi/LAT. No energy scaling is applied. Right panel: The same curve as in the left panel but with the scaling factor  $s = 0.9$  applied to the data.

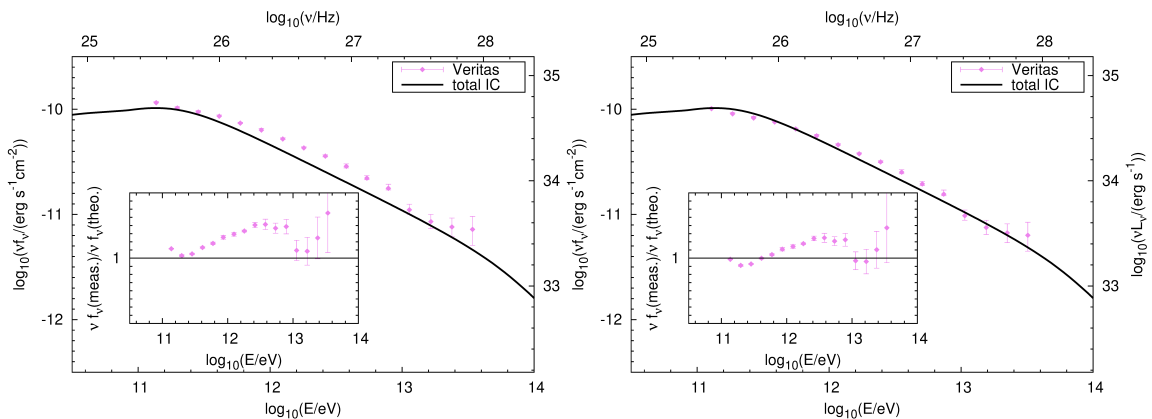


FIGURE 4.11: Left panel: The IC model (constant  $B$ -field model, solid black line) with measurements from VERITAS and Fermi/LAT. No energy scaling is applied. Right panel: The same curve as in the left panel but with the scaling factor  $s = 0.938$  applied to the data.

## 4.4 Conclusion

A varying magnetic field model reproduces the IC flux better than with a constant magnetic field, where the high energy part of the IC component was underestimated. By adjusting the IACTs to a common energy scale with Fermi/LAT and HEGRA, the cross calibration eliminates the systematic uncertainties. Indeed, all the relative shift of the energy scale are less than 10%. However, the Fermi/LAT's absolute energy uncertainty remains, but it implies an improvement from  $\pm 15\%$  to  $5\%$  and  $-3\%$ .



## Chapter 5

# Summary and conclusion

This work provides an updated non-thermal emission model of the Crab Nebula. In the framework of a constant (and static) volume-averaged magnetic field, the model is used to calculate the observable components of the Crab Nebula, such as its size and multiwavelength emission. The spatial distribution of the relativistic electrons in the nebula is deduced from observations. Including for the first time in details the spatial distribution of the photons coming from the thermal emission, the model is first used to reproduce the spectral energy distribution of the Crab Nebula. After adjusting the electron spectra parameters, the model describes well the observations over almost 15 orders of magnitude, but slightly underestimates the IC flux in the HE range. The dust is found to have a contribution to the IC flux  $\sim 15$  lower than previous estimates. The gamma-ray extension of the Crab Nebula is then calculated and compared with recent measurements. The calculated size of the nebula seen in the gamma-ray energies is found to be lower than the data, especially for energies  $\lesssim 100$  GeV, where the size plateaus. Therefore, the model fails to describe both the IC emission and the gamma-ray morphology of the Crab Nebula, but allows to draw important conclusions.

As seen in the previous chapters, the discrepancy between the modeled gamma-ray extension of the Crab Nebula and the measurements could have two possible explanations. The size of the IC nebula could be interpreted by the escape of electrons at the outer edge of the radio nebula. An other explanation could be that the unseen outer shell of the Crab Nebula may be visible with the Fermi/LAT. The supernova which gave rise to the Crab Nebula is believed to be a core-collapse supernova. Therefore, the presence of an outer blast wave around the nebula is expected. However, radio and X-ray observations have failed to unveil such outer shell. One possible explanation is that the density of the surrounding gas is not high enough to produce detectable circumstellar emission when interacting with the ejecta.

Under the assumption that the missing IC emission is produced by electrons in the outer shell, and the help of a varying magnetic field structure, the SED is recalculated by varying the magnetic field parameters. This more realistic model actually describes the high energy part of the IC component ( $E \gtrsim 100$  GeV) better than with a constant magnetic field.

Furthermore, an updated analysis of the Crab Nebula allows for a cross calibration between ground-based air shower experiments and the Fermi/LAT+HEGRA. Cross-calibration enable to eliminates the source of error when observing an object with several instruments, and thus enhance the significance of results based on combined measurements.

From the model presented in this work, more information about the physics of the crab nebula could be obtained in the future. In particular, it is of great interest to further investigate the nature of the event which gave rise to the Crab Nebula. If a fast outer shell is absent, the Crab Nebula could originate from a type of under-luminous supernova. This would bring us to reconsider our current understanding of supernova explosions. Recalculating the size of the IC nebula by considering outer shell electrons needs to be done in order to determine which scenario could be responsible for the gamma-ray morphology of the Crab Nebula.



## Appendix A

# Derivation of the expression of the spectral number density

The calculation of the spectral number density of photons,  $n_{seed}$  is straightforward assuming that the source is transparent for photons with a frequency  $\nu$ . Let us assume an isotropic spectral emissivity  $j_\nu$  in the infinitesimal volume  $d^3r'$ . The number of photons of frequency  $\varepsilon = h\nu$ , per unit volume, located at a distance  $r$  can be written:

$$n_{seed}(r, \varepsilon) = \int_{\nu} \delta n(\vec{r}, \vec{r}', \varepsilon) = \frac{1}{h\varepsilon} \int_{\nu} \frac{j_\nu(|\vec{r}'|, \varepsilon) d^3r'}{4\pi c |\vec{r} - \vec{r}'|^2}. \quad (\text{A.1})$$

The infinitesimal volumes  $d^3r'$  and  $d^3r$  are defined such that

$$d^3r' = r'^2 dr' \sin \theta' d\theta' d\varphi', \quad (\text{A.2})$$

$$d^3r = r^2 dr \sin \theta d\theta d\varphi, \quad (\text{A.3})$$

where the different coordinates are represented in Fig. A.1.

$$|\vec{r} - \vec{r}'| = r^2 - 2rr' \cos \alpha + r'^2, \quad (\text{A.4})$$

with  $\alpha$  be the angle between  $\vec{r}$  and  $\vec{r}'$ . Let us choose  $\theta$  such that  $\theta = 0$ , then  $\theta' = \alpha$ , and  $n$  can be expressed:

$$n(r, \nu) = \frac{1}{4\pi c} \frac{1}{h\varepsilon} \int_{\varphi'=0}^{\varphi'=2\pi} \int_{\theta'=0}^{\theta'=\pi} \int_{r_1}^{r_2} \frac{j_\nu(r') |\vec{r}'| r'^2 \sin \alpha d\alpha d\varphi' dr'}{r^2 - 2rr' \cos \alpha + r'^2}. \quad (\text{A.5})$$

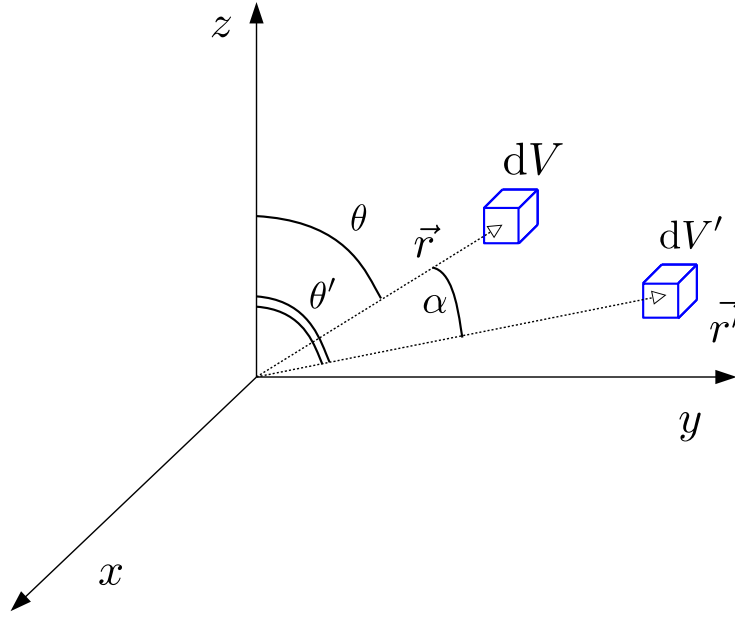


FIGURE A.1: Spherical coordinate system.

After integrating over  $\varphi'$  and multiplying numerator and denominator by  $2r$

$$n(r, \nu) = \frac{1}{2c} \frac{1}{h\varepsilon} \int_{\alpha=0}^{\alpha=\pi} \int_{r_1}^{r_2} \frac{j_\nu(r') |\vec{r}'| 2rr'^2 \sin \alpha d\alpha dr'}{2r(r^2 - 2rr' \cos \alpha + r'^2)}. \quad (\text{A.6})$$

Let  $f$  be a function of  $\alpha$  such that

$$f(\alpha) = \frac{2rr' \sin \alpha d\alpha dr'}{(r^2 - 2rr' \cos \alpha + r'^2)}, \quad (\text{A.7})$$

$f$  is defined and differentiable on  $\mathbf{R}$ :

$$\frac{df}{d\alpha} = [\ln |r^2 - 2rr' \cos \alpha + r'^2|]_0^\pi \quad (\text{A.8})$$

$$= \ln |r^2 + 2rr' + r'^2| - \ln |r^2 - 2rr' + r'^2| \quad (\text{A.9})$$

$$= \ln \left( \frac{r + r'}{|r - r'|} \right)^2 = 2 \ln \left( \frac{r + r'}{|r - r'|} \right). \quad (\text{A.10})$$

Therefore,  $n$  can finally be rewritten:

$$n(r, \nu) = \frac{1}{2c} \frac{1}{h\varepsilon} \int_{r_1}^{r_2} \frac{r'}{r} j_\nu(r') \ln \left( \frac{r + r'}{|r - r'|} \right) dr'. \quad (\text{A.11})$$

Assuming that the emissivity units are  $[j(r', \nu)] = \text{eV} \cdot \text{cm}^{-3} \cdot \text{s} \cdot \text{s}^{-1}$ , the spectral number density of seed photons is in units of  $[n_{seed}(r, \varepsilon)] = \text{eV}^{-1} \cdot \text{cm}^{-3} \cdot \text{s} \cdot \text{s}^{-1}$

## Appendix B

# Chandra images of the Crab Nebula in different energy bands

This appendix displays the images of the Crab Nebula from Chandra used in Chapter 2 (see subsubsec. 2.2.2) to determine the synchrotron extension of the Crab Nebula. The characteristic extension,  $R_{68}$ , has been calculated in 10 energy bins between 0.3 and 10 keV. The light blue circle represents the 68% containment radius and the black cross is the center of the circle. Table B.1 summarizes the different  $R_{68}$  associated to each image, as well as the coordinates of the center  $(x; y)$  of the circle.

Bin number	Energy range (keV)	$R_{68}$ (arcsec)	x (arcsec)	y (arcsec)
1	0.3-1.27	45.1	260.8	298.5
2	1.27-2.24	42.6	257.8	297.3
3	2.24-3.21	40.2	257.5	296.8
4	3.21-4.18	38.9	252.9	294.5
5	4.18-5.15	38.2	255.1	292.8
6	5.15-6.12	37.2	254.9	290.7
7	6.12-7.09	36.0	252.5	291.4
8	7.09-8.06	35.3	251.5	291.4
9	8.06-9.03	33.6	252.3	292.4
10	9.03-10	33.7	252.0	290.8

TABLE B.1: The ten different energy bands used to calculate the 68% containment radius,  $R_{68}$ .

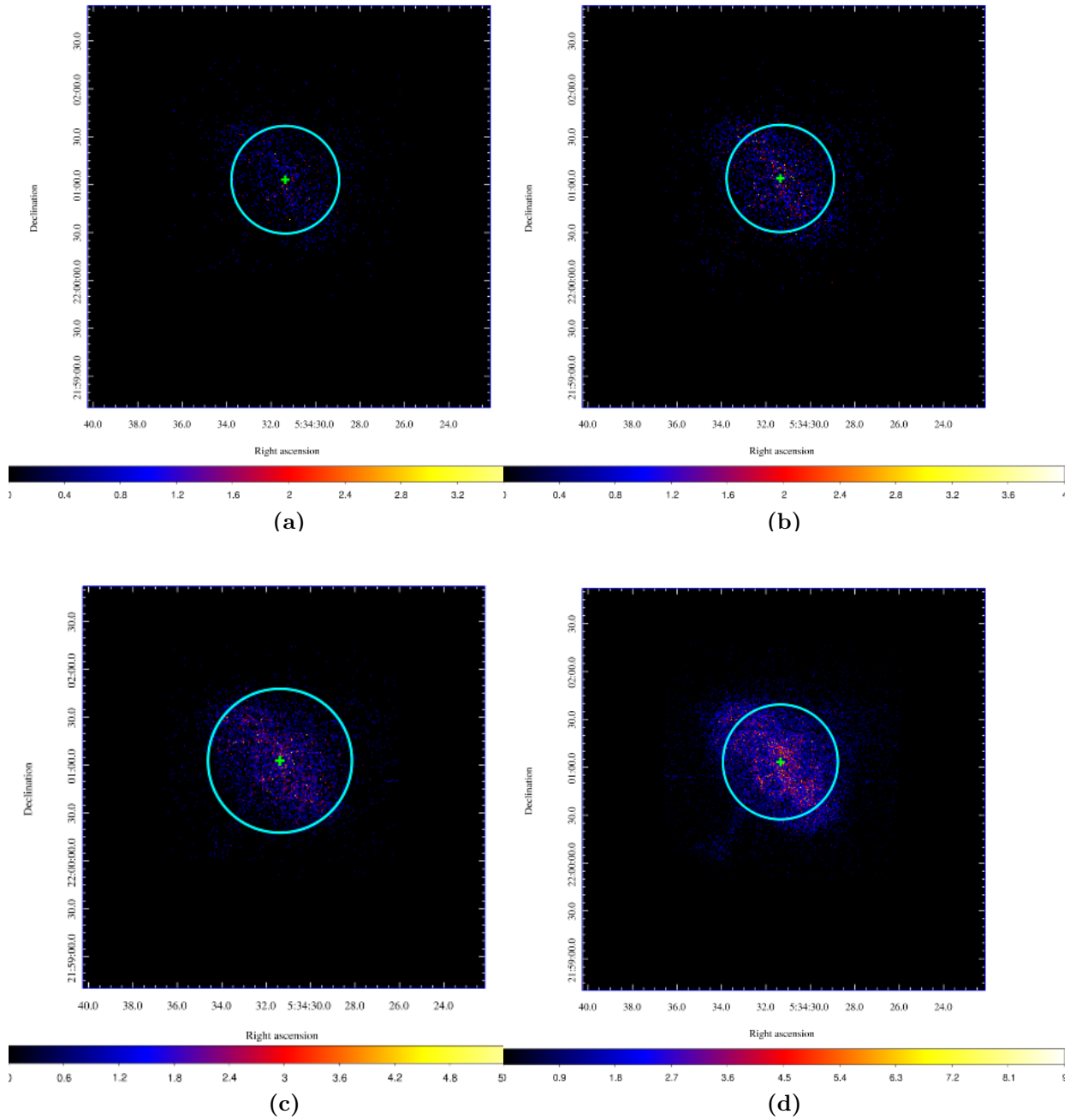


FIGURE B.1: Chandra images of the Crab Nebula in the energy band (a) 9.03-10 keV, (b) 8.06-9.03 keV, (c) 7.09-8.06 keV, (d) 6.12-7.09 keV. The light blue circle represents the 68% containment radius and the green cross the center of the circle and the centroid of the image (see text). The central blacked out region is the pulsar location and the horizontal line departing from it is the read-out of pulsed emission which spilled over. The Chandra images come from [ivo://ADS/Sa.CX0#obs/13154](http://ivo://ADS/Sa.CX0#obs/13154).

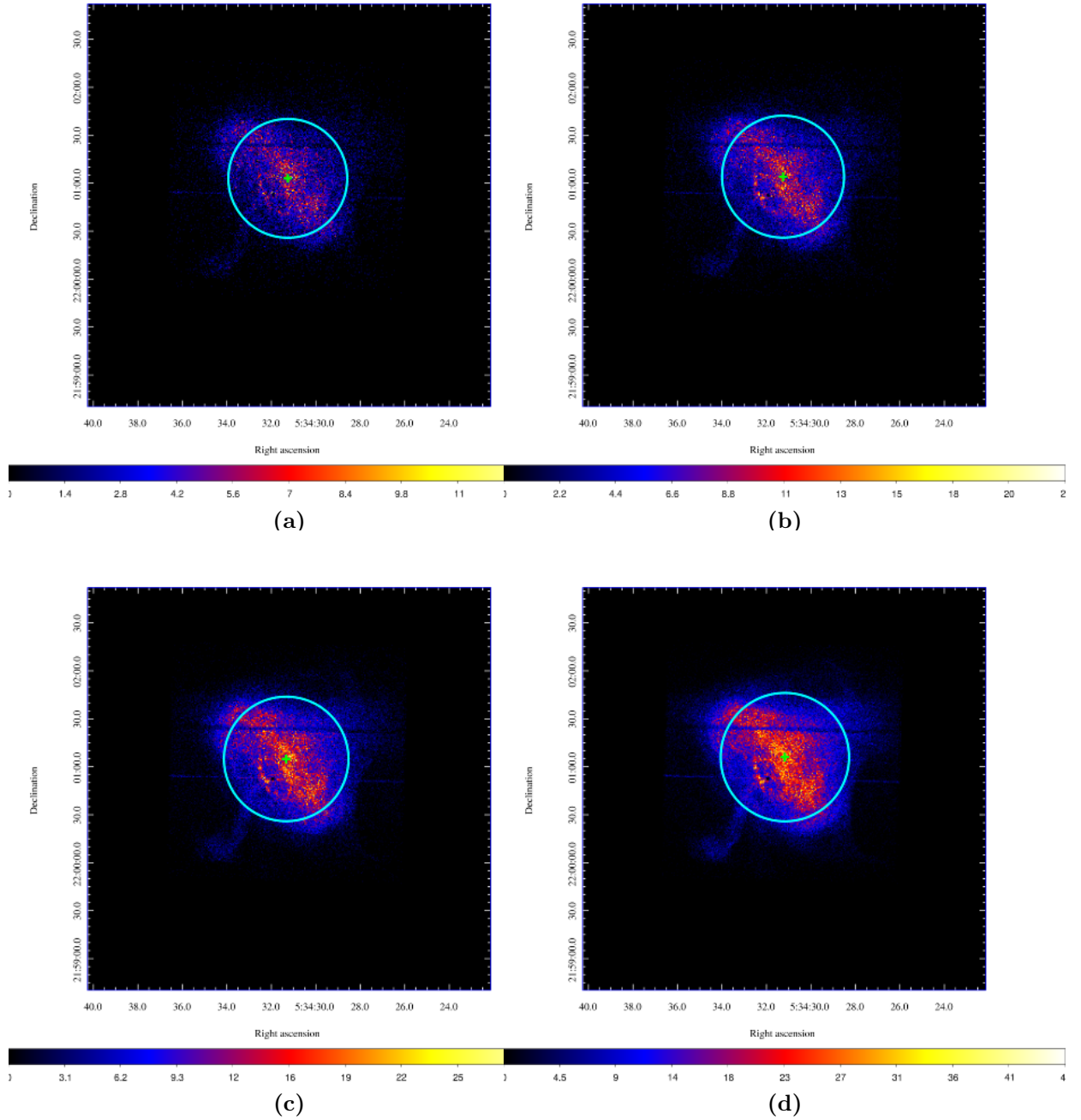


FIGURE B.2: Chandra images of the Crab Nebula in the energy band (a) 5.15-6.12 keV, (b) 4.18-5.15 keV, (c) 3.21-4.18 keV, (d) 2.24-3.21 keV. The light blue circle represents the 68% containment radius and the green cross the center of the circle and the centroid of the image (see text). The central blacked out region is the pulsar location and the horizontal line departing from it is the read-out of pulsed emission which spilled over. The Chandra images come from [ivo://ADS/Sa.CX0#obs/13154](https://ivo://ADS/Sa.CX0#obs/13154).

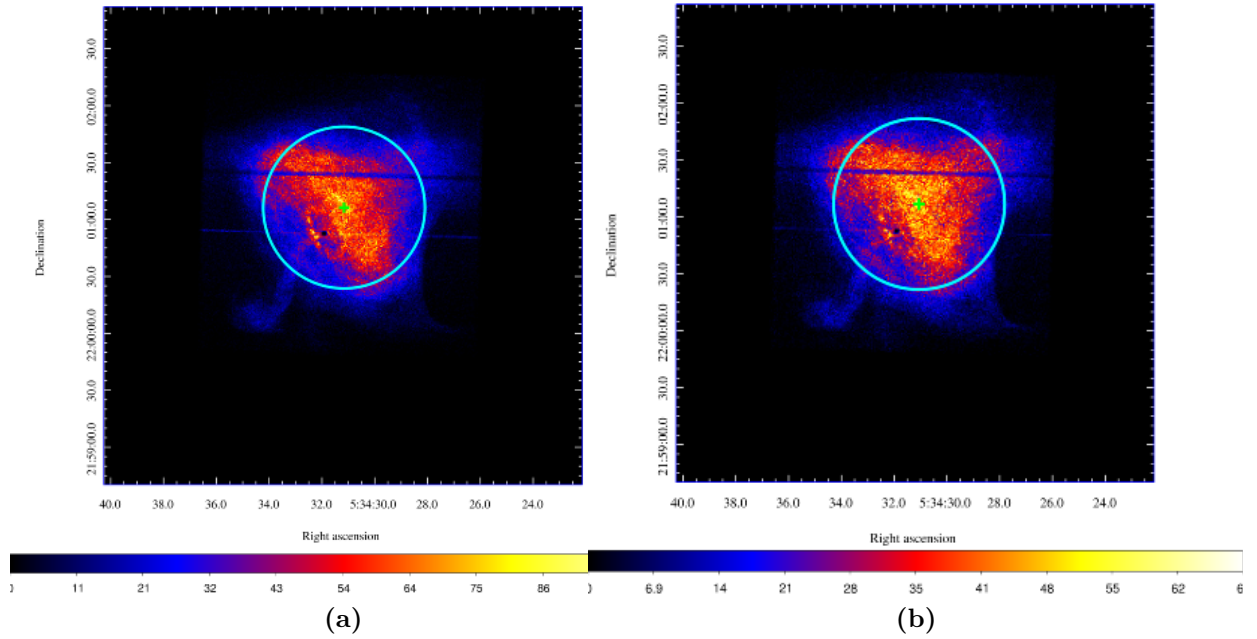


FIGURE B.3: Chandra images of the Crab Nebula in the energy band (a) 1.27-2.24 keV, (b) 0.3-1.27 keV. The light blue circle represents the 68% containment radius and the green cross the center of the circle and the centroid of the image (see text). The central blacked out region is the pulsar location and the horizontal line departing from it is the read-out of pulsed emission which spilled over. The Chandra images come from [ivo://ADS/Sa.CX0#obs/13154](http://ivo://ADS/Sa.CX0#obs/13154).

# Appendix C

## Program

The program was written in the C language, and the different numerical calculations were performed with the GNU scientific library (GSL). The different numerical integrations were performed with the QAG adaptive integration routine from GSL (see <https://www.gnu.org/software/gsl/doc/html/integration.html> for more details). The source files of the program can be found at the following address: <https://svnsrv.desy.de/desy/astrohh/dirsonlu/code/ludmillaCode/>.

### **C program used in the calculation of the SED, the intensity and the extension**

**Name of the program:** *crab\_spectrum*

The program calculates the complete spectrum of the Crab Nebula, as well as the intensity, with all the components described in the previous chapters and saves it in the form of a table. It also calculates the integrals of the intensity over the solid angle. The program *crab\_spectrum* is divided into several source files:

- **crab\_spectrum.c** contains the function `int main(void,*params)`.
- **calc\_crab\_lud.c** handles the spatial integrations.
- **ic\_lud.c** returns the IC flux or intensity.
- **initialize.c** contains the initial values of the different parameters used in the calculation.
- **sync.c** calculates the synchrotron flux or intensity.

- **create\_table.c** creates a table with the values of the function  $F(\nu/\nu_c)$  (see Chapitre 1, subsection 1.3.3, Eq. 1.30).
- **nel.c** contains the functions describing the electron spectra.

## Spectral energy distribution

The different quantities saved in the table to plot the SED are:

- the frequency in Hz,
- the total inverse Compton flux  $f_\nu^{IC}$  in units of  $\text{ergs s}^{-1} \text{cm}^{-2} \text{Hz}^{-1}$ ,
- the complete synchrotron flux, in units of  $f_\nu^{Sy}$ ,
- the thermal radiation from the dust in units of  $f_\nu$ .

### calc\_crab\_lud.c

Here are presented the main functions present in the file **calc\_crab\_lud.c**.

```
1 double nphot(double eps, void *params) {}
```

returns the CMB photon number density in units of photons  $\text{cm}^3 \text{eV}$ .

```
1 double dust_emissivity_shell(double eps, void *params) {}
```

returns the emissivity coming from the dust in  $\text{eV s s}^{-1} \text{cm}^{-3}$ .

```
1 calc_crab_dust(double eps, void *params){
```

returns the energy dependent seed photons number density,  $n_{seed}(\varepsilon)$ , by multiplying `dust_emissivity_shell()` by  $\frac{1}{h\varepsilon} \frac{1}{2c}$ .

- synchrotron seed photons

The functions used in the calculation for the synchrotron seed photons are (from the innermost to the outermost):

```
1 double integrand(double r, void *params) {}
```

returns

$$\frac{r}{r_1} \ln \frac{r+r_1}{|r-r_1|} e^{-\frac{r^2}{2\rho(\gamma')^2}}. \quad (\text{C.1})$$

```
1 double sync_kern_seed(double gammap, void *params) {}
```

returns

$$\frac{dN_{el}}{d\gamma'} \frac{\nu_p}{\nu_c} \int_{\nu_p/\nu_c} K_{5/3}(x) dx \int dr_1 \frac{r}{r_1} \ln \frac{r+r_1}{|r-r_1|} e^{-\frac{r^2}{2\rho(\gamma')^2}} n_0(\rho(\gamma')). \quad (\text{C.2})$$

```
1 double sync_seed(double nup, void *params) {}
```

Integrates `sync_kern_seed()` over  $\gamma'$ :

$$\int_{\gamma'} d\gamma' \frac{dN_{el}}{d\gamma'} \frac{\nu_p}{\nu_c} \int_{\nu_p/\nu_c} K_{5/3}(x) dx \int dr_1 \frac{r}{r_1} \ln \frac{r+r_1}{|r-r_1|} e^{-\frac{r^2}{2\rho(\gamma')^2}} n_0(\rho(\gamma')). \quad (\text{C.3})$$

```
1 double integrale_sync(double lr, void *params) {}
```

returns

$$e^{-\frac{r^2}{2\rho(\gamma)^2}} n_{seed}(r, \varepsilon). \quad (\text{C.4})$$

```
1 double calc_crab_dens(double eps, void *params) {}
```

Integrates `integrale_sync()` over the volume of the nebula:

$$\int_V d^3r e^{-\frac{r^2}{2\rho(\gamma)^2}} n_{seed}(r, \varepsilon) \quad (\text{C.5})$$

- Dust and CMB seed photons

The functions used in the calculation for the dust and CMB seed photons are (from the innermost to the outermost):

---

```
1 double first_integrale_cmb(double ly, void *params) {}
```

---

returns:

$$r^2 e^{\frac{-r^2}{2\rho(\gamma)^2}}, \quad (\text{C.6})$$

for the CMB seed photons.

---

```
1 double first_integrale_shell(double r, void *params) {}
```

---

returns

$$\left[ \left( r_{out} + \left[ \frac{r_{out}^2}{2y} - \frac{r}{2} \right] \ln \frac{1 + r_{out}/r}{|r_{out}/r - 1|} \right) - \left( r_{in} + \left[ \frac{r_{in}^2}{2y} - \frac{r}{2} \right] \ln \frac{1 + r_{in}/r}{|r_{in}/r - 1|} \right) \right] r^2 e^{\frac{-r^2}{2\rho(\gamma)^2}}, \quad (\text{C.7})$$

for the dust seed photons.

---

```
1 double integrale(void *params) {}
```

---

Integrates `first_integrale_shell()` and `first_integrale_cmb()` over the volume of the nebula.

---

```
1 double ic_kern2(double epsilon, void *params) {}
```

---

multiplies `calc_crab_dens()`, `calc_crab_dust()` or `nphot()` by  $\frac{f_{IC}(\epsilon, \nu, \gamma)}{\epsilon}$ .

---

```
1 double ic_kern(double gamma, void *params)
```

---

integrates `ic_kern2()` over  $\epsilon$ .

For dust and CMB seed photons, the result of the function is multiplied by the function `integrale()`. For the synchrotron seed photons, the result of the function is multiplied by  $dN_{el}/d\gamma$ .

---

```
1 double ic(double nu, void *params) {}
```

---

integrates `ic_kern()` over  $\gamma$  and returns the IC flux in units of  $\text{erg cm}^{-2} \text{s}^{-1} \text{Hz}^{-1}$ .

## Intensity

The intensity is returned by the function `ic()`. For the synchrotron seed photons, the choice of calculating either the intensity or the IC flux is made in the file `calc_crab_lud.c`, in the function `calc_crab_dens()`. In the function `ic_kern` for the cmb and dust, the user can make the choice to calculate the intensity or the flux by multiplying the result by `intensity_rdep()`, or `integrale` respectively.

```
1 double intensity_rdep(double alpha, void *params){}
```

integrates `sintegrale_sync()`, `first_integrale_shell()` and `first_integrale_cmb()` over  $r$ .

```
1 double sintegrale_sync(double s, void *params){}
```

then `calc_crab_dens()` is multiplied by the function `intensity_rdep()` or `ic_kern` for the cmb and dust.

# Appendix D

## Acronyms

<b>LAT</b>	Large area telescope
<b>PSF</b>	Point spread function
<b>HESS</b>	High Energy Stereoscopic System
<b>SED</b>	Spectral energy distribution
<b>HE</b>	High energy
<b>VHE</b>	Very high energy
<b>SSC</b>	Synchrotron-self-Compton
<b>IC</b>	Inverse Compton
<b>HAWC</b>	High Altitude Water Cherenkov Experiment
<b>VERITAS</b>	Very Energetic Radiation Imaging Telescope Array System
<b>PWN</b>	Pulsar wind nebula
<b>SN</b>	Supernova
<b>MHD</b>	Magnetohydrodynamics
<b>MAGIC</b>	Major Atmospheric Gamma Imaging Cherenkov Telescopes
<b>HEGRA</b>	High-Energy-Gamma-Ray Astronomy
<b>CMB</b>	Cosmic microwave background

## Appendix E

# Definition of the 68% containment radius

The infinitesimal area  $d^2r$  is defined such that:

$$d^2r = r dr d\varphi, \quad (\text{E.1})$$

By definition of the 68% containment radius (see Fig.E.1):

$$0.68 = \frac{\int_0^{R_{68}} I(r) d^2r}{\int_0^\infty I(r) d^2r} \quad (\text{E.2})$$

$$= \frac{2\pi \int_0^{R_{68}} I(r) r dr}{2\pi \int_0^\infty I(r) r dr} \quad (\text{E.3})$$

$$= \frac{\int_0^{R_{68}} k e^{-r^2/(2\sigma_{1D}^2)} dr^2}{\int_0^\infty k e^{-r^2/(2\sigma_{1D}^2)} dr^2} \quad (\text{E.4})$$

$$= \frac{[e^{-r^2/(2\sigma_{1D}^2)}]_0^{R_{68}}}{[e^{-r^2/(2\sigma_{1D}^2)}]_0^\infty} \quad (\text{E.5})$$

$$= 1 - e^{-R_{68}^2/(2\sigma_{1D}^2)}. \quad (\text{E.6})$$

Therefore, we obtain the following relationship between  $\sigma_{1D}$  and  $R_{68}$ :

$$R_{68} = \ln(0.32)\sigma_{1D} \simeq 1.509\sigma_{1D}. \quad (\text{E.7})$$

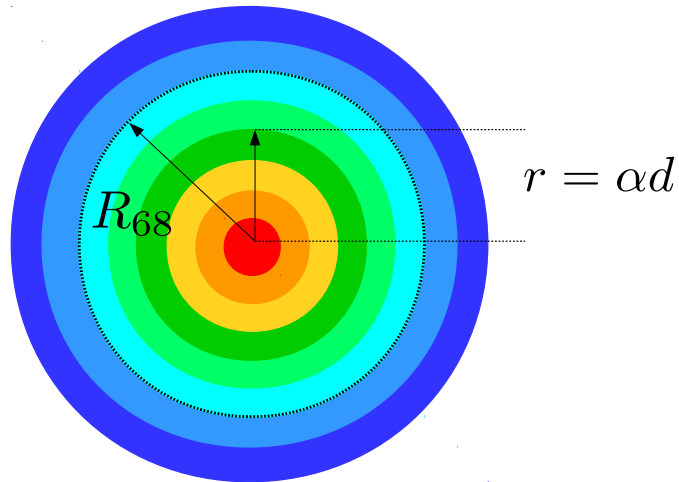


FIGURE E.1: Representation of the 68% containment radius. The intensity  $I$  as a function of the angular distance  $r = \alpha d$  from the center of the nebula is well described by a Gaussian. This is qualitatively shown by the color grading which goes from red at the center to blue at the edge of the nebula.

# List of Figures

1	Energy-dependence of the observed extension (black) and theoretical predictions based on various seed-photon fields (dark blue for CMB, cyan for dust, green for synchrotron-self-Compton (SSC) and red for total seed-photon field). The data are taken from Yeung and Horns (2019), Ackermann et al. (2018) and Holler et al. (2017)). . . . .	vii
2	SED of the Crab Nebula calculated in the framework of the constant $B$ -field model (black line). The total contribution of radio electrons to the synchrotron flux is shown (dashed red line), as well as the contribution from the wind electrons (dashed blue line). The non-thermal emission coming from the dust (gray line) and from the filaments (thin orange line) are also represented. . . . .	vii
1.1	Color composite of the Crab synchrotron nebula showing a Chandra X-ray image in blue and white, a visible light image taken with HST in purple, and a Spitzer infrared image in pink. The pulsar is seen as the white blue point source at the center of the image. It can be seen that the emission is brightest near the center of the nebula close to where the high-energy electron are injected. Moving outward through the nebula, the emission becomes fainter owing to adiabatic and radiative losses as almost only low-energy electrons survive long enough to reach the edge of the nebula. The picture is taken from <a href="http://chandra.harvard.edu/photo/2018/crab/">http://chandra.harvard.edu/photo/2018/crab/</a> . . . . .	4
1.2	The Crab Nebula seen in different energy bands: (a) radio <a href="https://public.nrao.edu/gallery/crab-nebula/">https://public.nrao.edu/gallery/crab-nebula/</a> (b) infrared <a href="https://public.nrao.edu/gallery/crab-nebula/">https://public.nrao.edu/gallery/crab-nebula/</a> (c) optical <a href="https://www.spacetelescope.org/images/heic0515a/">https://www.spacetelescope.org/images/heic0515a/</a> (d) UV <a href="https://www.esa.int/spaceinimages/Images/2018/03/Crab_Nebula_in_ultraviolet">https://www.esa.int/spaceinimages/Images/2018/03/Crab_Nebula_in_ultraviolet</a> (e) X-ray <a href="https://www.spacetelescope.org/images/potw1720f/">https://www.spacetelescope.org/images/potw1720f/</a> (f) gamma-rays <a href="https://svs.gsfc.nasa.gov/cgi-bin/details.cgi?aid=10767">https://svs.gsfc.nasa.gov/cgi-bin/details.cgi?aid=10767</a> . . . . .	5
1.3	Overlaying images of various optical wavelength observations from HST. The filaments are formed by line emission of atoms that have been ionized by the synchrotron radiation. Shown are the forbidden lines of oxygen and silicon. [O III] $\lambda$ 5007 is shown in red, [S II] $\lambda\lambda$ 6717,6731 in green, and [O I] $\lambda$ 6300 in blue. The synchrotron continuum filling the nebula is shown in light blue. The X-ray emitting torus from Fig. 1.1 is in the center of this picture. The image is taken from Hester (2008). . . . .	6

- 1.4 Sketch of the interior of the supernova remnant SN1054 showing the sites and radiation mechanisms of non thermal emission associated with rotation powered pulsars. (i) the region within the light cylinder where the magnetospheric pulsed radiation from radio to  $\gamma$ -rays is produced; (ii) the relativistic wind of positrons and electrons terminates at a shock front, where the wind of cold relativistic plasma meets the surrounding material of the supernova remnant. The wind emits GeV and TeV  $\gamma$ -rays through the IC mechanism; (iii) the surrounding synchrotron nebula which emits broadband electromagnetic radiation from radio to multi-TeV  $\gamma$ -rays through the synchrotron and IC processes. Source of illustration: Aharonian and Bogovalov (2003). . . . . 7
- 1.5 SED of the Crab Nebula with the different measurements used in this work. The optical line emission from thermal filaments is shown in orange line. . . . . 10
- 1.6 (a) A planar shock wave propagating at a supersonic velocity,  $V_s$  through a stationary medium with density  $\rho_1$ , pressure  $p_1$  and temperature  $T_1$  (b) rest system of the shock wave. In the non-relativistic case, it follows from the shock conditions that, for a strong shock, the velocities of the plasmas upstream and downstream are linked by  $v_+ = 1/4v_-$  (c) rest system of the upstream plasma. The particles velocity is isotropized and the plasma downstream flows toward the shock at the speed of  $3/4v_-$  (d) rest system of the plasma downstream. It shows the same situation as in (b). The figures are based on Longair (2011). . . . . 20
- 1.7 Radiation pattern of charged particles moving in a circular path: blue ( $\beta \ll 1$ ) and red ( $\beta \approx 1$ ) give ref. The opening angle of the frontward lobe is  $\psi \sim 2/\gamma$  whereas the backward lobe is smashed. Source of illustration: <https://www.intechopen.com/books/synchrotron-radiation-useful-and-interesting-fundamental-of-synchrotron-radiations> . . . . . 25
- 1.8 Waves structure for a spherical shock. The ejecta are shown in red and the interstellar medium is represented in blue. Shocked material is in dark color and undisturbed material is in light colors. The illustration is from Ferrand (2008) . . . . . 30
- 2.1 Characteristic extensions (defined as the standard deviation  $\sigma$ ; assuming the intensity to have a Gaussian profile) in different energy-segments, from the radio band to the X-ray band. The radio data are based on a VLA (5.5 GHz) image (published in Bietenholz et al. (2004)) and on the map of total intensity at 2.7 GHz in Wilson (1972). The optical data are from Grindlay and Hoffman (1971) and Scargle (1969). The Chandra characteristic extensions are determined within this work (see text for more details). The NuSTAR measurements are provided by Madsen et al. (2015). The blue line is the function which best describes the dependency between the characteristic extension and the photon energy. The left vertical dashed line represents the frequency  $\nu_{break} = (1.2 \pm 0.2) \times 10^{14}$  Hz at which the synchrotron extension starts to depend upon the frequency. The right dashed line indicates the frequency of the last data point:  $\nu_{obs,max} = (1.4 \pm 0.5) \times 10^{19}$ . . . . . 38

2.2	Chandra images of the Crab Nebula in the energy band 7.09-8.06 keV (right panel) and 0.3-1.27 keV (left panel). The light blue circle represents the 68% containment radius and the green cross the center of the circle and the centroid of the image (see text). The central blacked out region is the pulsar location and the horizontal line departing from it is the read-out of pulsed emission which spilled over. The Chandra images come from <code>ivo://ADS/Sa.CX0#obs/13154</code> . . . . .	39
2.3	Scale length $\rho$ of the electron distribution as a function of the Lorentz factor $\gamma$ . The dashed line represents the parameter $\gamma_{break}$ such that for $\gamma < \gamma_{break}$ , $\rho$ is a constant. . . . .	40
2.4	Electron number density $n_{el}$ , as a function of the ratio $r/r_s$ for different values of the Lorentz factor $\gamma$ , $r$ is the distance to the center of the Crab Nebula and $r_s$ is the termination shock radius. The radius of the nebula, $R_{PWN}$ corresponds to $r/r_s \approx 20$ . . . . .	41
2.5	Lorentz factor $\gamma$ as a function of the magnetic field $B$ corresponding to the synchrotron cooling frequency $\gamma_{cool}$ , to the upper $\nu_{opt}^{sup}$ and lower $\nu_{opt}^{inf}$ limits of the break frequency $\nu_{opt}$ . . . . .	42
2.6	The two components of the electron spectrum used to calculate the broad band SED of the Crab Nebula in the constant B-field model. The radio electrons are showed in red solid line, while the wind electrons are represented by the blue solid line. The black dashed lines indicate the minimum, maximum and break energies. . . . .	44
2.7	The contribution of dust emission from the filaments and synchrotron emission in the FIR-sub-mm range is shown in magenta points, the gray solide line represents the two-temperature-blackbody model used to fit the data and the light blue line represents the modelled synchrotron emission. The dark blue line is the total flux obtained from summing the synchrotron and the two dust components. The data are taken from Gomez et al. (2012). . . . .	45
2.8	Dust photon number density in photons per $\text{cm}^3$ per eV (for an energy of $\varepsilon = 0.01$ eV). Most of the photons are located in the area between $1.7 \text{ pc} \lesssim r \lesssim 2.3 \text{ pc}$ . . . . .	46
2.9	Spatial overlap between the electrons and dust photons $n_{seed}(\varepsilon, r)n_{el}(\gamma, r)$ multiplied by $r^2$ , for $\varepsilon = 0.01$ and for different values of $\gamma$ . . . . .	47
2.10	SSC flux from the Crab Nebula, calculated in the frame of the constant $B$ -field model. . . . .	48
2.11	IC flux coming from the synchrotron seed photons for $\gamma = 10^5$ and $\nu = 10^{23}$ . . . . .	49
2.12	IC flux coming from the synchrotron seed photons for $\gamma = 10^3$ and $\nu = 10^{23}$ . . . . .	49
2.13	photon number density from the CMB in photons per $\text{cm}^3 \text{ eV}^{-1}$ . . . . .	50
3.1	The predicted IC spectrum above 700 MeV used to calculate $\chi^2(B)$ for a range of B field values using only the Fermi data. Here the IC spectrum is represented for $B = 167 \mu\text{G}$ . . . . .	53
3.2	$\chi^2$ minimization of the IC flux fit to the Fermi/LAT measurements by variation of the magnetic field. . . . .	54

3.3	SED of the Crab Nebula calculated in the framework of the constant $B$ -field model (black line). The total contribution of radio electrons to the synchrotron flux is shown (dashed red line), as well as the contribution from the wind electrons (dashed blue line). The non-thermal emission coming from the dust (gray line) and from the filaments (thin orange line) are also represented. . . . .	55
3.4	Contributions to the flux of inverse Compton scattering: the synchrotron radiation (red line), the thermal emission of the dust (magenta), and the CMB (blue line). The black line represents the total emission calculated in the constant $B$ -field model. . . . .	56
3.5	The two components of the electron spectrum used to calculate the broad band SED of the Crab Nebula in the constant $B$ -field model. The radio electrons (red line) and the wind electrons (blue line) are represented. The black solid line indicates the value for the minimum, maximum and break energies. . . . .	57
3.6	Representation of the quantities used to define the intensity (see text for more details). . . . .	60
3.7	Let $\delta A$ be some area on a source at a distance $D$ subtending a solid angle $\delta\Omega$ at a detector; while the detector of area $\delta a$ , subtends a solid angle $\delta\omega$ at the source. . . . .	61
3.8	Representation of the Crab Nebula (blue circle) located at a distance $d$ from us. The ligne of sight is denoted by $s$ , and $\alpha$ represents the angular size of the Crab Nebula. See text for more details. . . . .	63
3.9	The Crab Nebula is represented by the blue circle. Here the approximation $d \simeq d'$ is made. The area between the two vertical lines represents the region where the emissivity is non-zero. See text for more details. . . . .	64
3.10	Comparison between the IC fluxes calculated in the constant $B$ -field model (smooth lines) and the IC fluxes obtained by integration of the calculated intensity over the solid angle (broken lines). The contributions from the different seed photon fields are shown: (1) synchrotron, (2) thermal dust, (3) CMB. . . . .	66
3.11	Normalized synchrotron intensity calculated within the constant $B$ -field model (blue line) in comparison to the expected intensity in the delta approximation (light blue line) for different values of $\nu$ . Both contributions from radio and wind electrons are taken into account. . . . .	67
3.12	The IC intensity for the CMB photons calculated within the constant $B$ -field model (blue line) normalized to the intensity for $\alpha = 0$ compared with the expected intensity in the delta approximation (light blue line) for two different values of $\nu$ . . . . .	69
3.13	Intensity $I$ normalized over the intensity at $\alpha = 0$ , $I(\alpha = 0)$ for the three different seed photons fields. . . . .	70
3.14	Intensity $I$ normalized over the total intensity at $\alpha = 0$ , $I_{tot}(\alpha = 0)$ and calculated for $\nu = 10^{23}$ and $\nu = 10^{25}$ . . . . .	71
3.15	Energy-dependence of the observed extension (black) and theoretical predictions based on various seed-photon fields (dark blue for CMB, cyan for dust, green for synchrotron-self-Compton (SSC) and red for total seed-photon field). The characteristic extension is defined by equation 3.41. The data are from Yeung and Horns (2019), except the last measurement which is taken from Holler et al. (2017) . . . . .	72

4.1	The magnetic field in the Crab Nebula at different distances $r$ (right panel) and angular distances (left panel) for different values of the parameter $\sigma$ in the framework of the MHD model of KC; $r = r_s$ corresponds to the distance of the wind termination shock from the pulsar. The left plot is taken from de Jager et al. (1996) and the right plot from Atoyan and Aharonian (1996a).	75
4.2	Magnetic field $B$ used in the calculations. The value of the magnetic field is $B_1 = 87 \mu\text{G}$ for ( $r/r_s \lesssim 5$ ) and then jump to $B_2 = 149 \mu\text{G}$ , it is decreasing to 0 for $r/r_s \gtrsim 23$ .	76
4.3	Synchrotron spectrum represented in the case of the constant $B$ -field model (light blue line) and in the case of a varying magnetic field (blue line). Here $B_1 = 80 \mu\text{G}$ and $B_2 = 250 \mu\text{G}$ .	77
4.4	Contributions to the flux of inverse Compton scattering: the synchrotron radiation in the constant $B$ -field model (red line) and after varying the magnetic field, the thermal emission of the dust (magenta line), and the CMB (blue line).	78
4.5	The IC model (constant $B$ -field model, solid black line) is adjusted to the measurements from MAGIC and Fermi/LAT.	79
4.6	Contributions to the flux of inverse Compton scattering: the synchrotron radiation (red line), the thermal emission of the dust (magenta line), and the CMB (blue line). The black line represents the total emission calculated in the current $B$ field step model.	79
4.7	Left panel: The IC model (constant $B$ -field model, solid black line) with measurements from MAGIC and Fermi/LAT. No energy scaling is applied. Right panel: The same curve as in the left panel but with the scaling factor $s = 1.02$ applied to the data.	81
4.8	Left panel: The IC model (constant $B$ -field model, solid black line) with measurements from H.E.S.S and Fermi/LAT. No energy scaling is applied. Right panel: The same curve as in the left panel but with the scaling factor $s = 0.96$ applied to the data.	82
4.9	The IC model (constant $B$ -field model, solid black line) with measurements from Tibet and Fermi/LAT. No energy scaling is applied.	82
4.10	Left panel: The IC model (constant $B$ -field model, solid black line) with measurements from HAWC and Fermi/LAT. No energy scaling is applied. Right panel: The same curve as in the left panel but with the scaling factor $s = 0.9$ applied to the data.	83
4.11	Left panel: The IC model (constant $B$ -field model, solid black line) with measurements from VERITAS and Fermi/LAT. No energy scaling is applied. Right panel: The same curve as in the left panel but with the scaling factor $s = 0.938$ applied to the data.	83
A.1	Spherical coordinate system.	87
B.1	Chandra images of the Crab Nebula in the energy band <b>(a)</b> 9.03-10 keV, <b>(b)</b> 8.06-9.03 keV, <b>(c)</b> 7.09-8.06 keV, <b>(d)</b> 6.12-7.09 keV. The light blue circle represents the 68% containment radius and the green cross the center of the circle and the centroid of the image (see text). The central blacked out region is the pulsar location and the horizontal line departing from it is the read-out of pulsed emission which spilled over. The Chandra images come from <code>ivo://ADS/Sa.CXO#obs/13154</code> .	89

- B.2 Chandra images of the Crab Nebula in the energy band **(a)** 5.15-6.12 keV, **(b)** 4.18-5.15 keV, **(c)** 3.21-4.18 keV, **(d)** 2.24-3.21 keV. The light blue circle represents the 68% containment radius and the green cross the center of the circle and the centroid of the image (see text). The central blacked out region is the pulsar location and the horizontal line departing from it is the read-out of pulsed emission which spilled over. The Chandra images come from `ivo://ADS/Sa.CXO#obs/13154`. . . . . 90
- B.3 Chandra images of the Crab Nebula in the energy band **(a)** 1.27-2.24 keV, **(b)** 0.3-1.27 keV. The light blue circle represents the 68% containment radius and the green cross the center of the circle and the centroid of the image (see text). The central blacked out region is the pulsar location and the horizontal line departing from it is the read-out of pulsed emission which spilled over. The Chandra images come from `ivo://ADS/Sa.CXO#obs/13154`. . . . . 91
- E.1 Representation of the 68% containment radius. The intensity  $I$  as a function of the angular distance  $r = \alpha d$  from the center of the nebula is well described by a Gaussian. This is qualitatively shown by the color grading which goes from red at the center to blue at the edge of the nebula. . . . 99

# List of Tables

1.1	Compilation of observations of the Crab Nebula from radio to very high energies. . . . .	8
1.2	Different models used for modelling the Crab Nebula. <b>D</b> represents the number of spatial dimension used in the model. <b>B</b> indicates the treatment of the magnetic field. “Obs.,” “Sync.” and “Phen.” stands for “Observations”, “Synchrotron” and “Phenomenology” respectively. . . .	16
1.3	Summary of the relations of the spectral and photon indices. Each line gives the respective index depending on the index of the respective column. . . . .	26
3.1	Parameters of the electron spectra used in the constant B-field model. At the energy $\gamma_{min}$ , the radio electron spectrum cuts off sharply whereas the wind electrons cut off superexponentially. The energy $\gamma_{max}$ denotes a sharp cut-off for the radio and wind electrons. . . . .	56
3.2	The correlation coefficients between the fit-parameters of the synchrotron spectrum. Since the matrix is symmetric, the lower trigonal part is not shown. . . . .	57
4.1	Energy scaling factors of the IACTs used for the cross calibration. . . . .	81
B.1	The ten different energy bands used to calculate the 68% containment radius, $R_{68}$ . . . . .	88

# Bibliography

M. G. Aartsen, M. Ackermann, J. Adams, J. A. Aguilar, M. Ahlers, M. Ahrens, D. Altmann, T. Anderson, C. Argüelles, T. C. Arlen, J. Auffenberg, X. Bai, S. W. Barwick, V. Baum, J. J. Beatty, J. Becker Tjus, K. H. Becker, S. BenZvi, P. Berghaus, D. Berley, E. Bernardini, A. Bernhard, D. Z. Besson, G. Binder, D. Bindig, M. Bissook, E. Blaufuss, J. Blumenthal, D. J. Boersma, C. Böhm, F. Bos, D. Bose, S. Böser, O. Botner, L. Brayeur, H. P. Bretz, A. M. Brown, J. Casey, M. Casier, D. Chirkin, A. Christov, B. Christy, K. Clark, L. Classen, F. Clevermann, S. Coenders, D. F. Cowen, A. H. Cruz Silva, M. Danninger, J. Daughhetee, J. C. Davis, M. Day, J. P. A. M. de André, C. De Clercq, S. De Ridder, P. Desiati, K. D. de Vries, M. de With, T. DeYoung, J. C. Díaz-Vélez, M. Dunkman, R. Eagan, B. Eberhardt, B. Eichmann, J. Eisch, S. Euler, P. A. Evenson, O. Fadiran, A. R. Fazely, A. Fedynitch, J. Feintzeig, J. Felde, T. Feusels, K. Filimonov, C. Finley, T. Fischer-Wasels, S. Flis, A. Franckowiak, K. Frantzen, T. Fuchs, T. K. Gaisser, J. Gallagher, L. Gerhardt, D. Gier, L. Gladstone, T. Glüsenkamp, A. Goldschmidt, G. Golup, J. G. Gonzalez, J. A. Goodman, D. Góra, D. T. Grandmont, D. Grant, P. Gretskov, J. C. Groh, A. Groß, C. Ha, C. Haack, A. Haj Ismail, P. Hallen, A. Hallgren, F. Halzen, K. Hanson, D. Hebecker, D. Heereman, D. Heinen, K. Helbing, R. Hellauer, D. Hellwig, S. Hickford, G. C. Hill, K. D. Hoffman, R. Hoffmann, A. Homeier, K. Hoshina, F. Huang, W. Huelsnitz, P. O. Hulth, K. Hultqvist, S. Hussain, A. Ishihara, E. Jacobi, J. Jacobsen, K. Jagielski, G. S. Japaridze, K. Jero, O. Jlelati, M. Jurkovic, B. Kaminsky, A. Kappes, T. Karg, A. Karle, M. Kauer, J. L. Kelley, A. Kheirandish, J. Kiryluk, J. Kläs, S. R. Klein, J. H. Köhne, G. Kohnen, H. Kolanoski, A. Koob, L. Köpke, C. Kopper, S. Kopper, D. J. Koskinen, M. Kowalski, A. Kriesten, K. Krings, G. Kroll, M. Kroll, J. Kunnen, N. Kurahashi, T. Kuwabara, M. Labare, D. T. Larsen, M. J. Larson, M. Lesiak-Bzdak, M. Leuermann, J. Leute, J. Lünemann, O. Macías, J. Madsen, G. Maggi, R. Maruyama, K. Mase, H. S. Matis, F. McNally, K. Meagher, M. Medici, A. Meli, T. Meures, S. Miarecki, E. Middell, E. Middlemas, N. Milke, J. Miller, L. Mohrmann, T. Montaruli, R. Morse, R. Nahnauer, U. Naumann, H. Niederhausen,

S. C. Nowicki, D. R. Nygren, A. Obertacke, S. Odrowski, A. Olivas, A. Omairat, A. O'Murchadha, T. Palczewski, L. Paul, Ö. Penek, J. A. Pepper, C. Pérez de los Heros, C. Pfindner, D. Pieloth, E. Pinat, J. Posselt, P. B. Price, G. T. Przybylski, J. Pütz, M. Quinnan, L. Rädcl, M. Rameez, K. Rawlins, P. Redl, I. Rees, R. Reimann, E. Resconi, W. Rhode, M. Richman, B. Riedel, S. Robertson, J. P. Rodrigues, M. Rongen, C. Rott, T. Ruhe, B. Ruzybayev, D. Ryckbosch, S. M. Saba, H. G. Sand er, J. Sandroos, M. Santander, S. Sarkar, K. Schatto, F. Scheriau, T. Schmidt, M. Schmitz, S. Schoenen, S. Schöneberg, A. Schönwald, A. Schukraft, L. Schulte, O. Schulz, D. Seckel, Y. Sestayo, S. Seunarine, R. Shanidze, C. Sheremata, M. W. E. Smith, D. Soldin, G. M. Spiczak, C. Spiering, M. Stamatikos, T. Stanev, N. A. Stanisha, A. Stasik, T. Stezelberger, R. G. Stokstad, A. Stöbl, E. A. Strahler, R. Ström, N. L. Strotjohann, G. W. Sullivan, H. Taavola, I. Taboada, A. Tamburro, A. Tepe, S. Ter-Antonyan, A. Terliuk, G. Tešić, S. Tilav, P. A. Toale, M. N. Tobin, D. Tosi, M. Tselengidou, E. Unger, M. Usner, S. Vallecorsa, N. van Eijndhoven, J. Vand enbroucke, J. van Santen, M. Vehring, M. Voge, M. Vraeghe, C. Walck, M. Wallraff, Ch. Weaver, M. Wellons, C. Wendt, S. Westerhoff, B. J. Whelan, N. Whitehorn, C. Wichary, K. Wiebe, C. H. Wiebusch, D. R. Williams, H. Wissing, M. Wolf, T. R. Wood, K. Woschnagg, D. L. Xu, X. W. Xu, J. P. Yanez, G. Yodh, S. Yoshida, P. Zarzhitsky, J. Ziemann, S. Zierke, M. Zoll, J. Aasi, B. P. Abbott, R. Abbott, T. Abbott, M. R. Abernathy, F. Acernese, K. Ackley, C. Adams, T. Adams, P. Addesso, R. X. Adhikari, C. Affeldt, M. Agathos, N. Aggarwal, O. D. Aguiar, P. Ajith, A. Alesic, B. Allen, A. Allocca, D. Amariutei, M. Andersen, R. A. Anderson, S. B. Anderson, W. G. Anderson, K. Arai, M. C. Araya, C. Arceneaux, J. S. Areeda, S. Ast, S. M. Aston, P. Astone, P. Aufmuth, H. Augustus, C. Aulbert, B. E. Aylott, S. Babak, P. T. Baker, G. Ballardini, S. W. Ballmer, J. C. Barayoga, M. Barbet, B. C. Barish, D. Barker, F. Barone, B. Barr, L. Barsotti, M. Barsuglia, M. A. Barton, I. Bartos, R. Bassiri, A. Basti, J. C. Batch, J. Bauchrowitz, Th. S. Bauer, C. Baune, V. Bavigadda, B. Behnke, M. Bejger, M. G. Beker, C. Belczynski, A. S. Bell, C. Bell, G. Bergmann, D. Bersanetti, A. Bertolini, J. Betzwieser, I. A. Bilenko, G. Billingsley, J. Birch, S. Biscans, M. Bitossi, C. Biwer, M. A. Bizouard, E. Black, J. K. Blackburn, L. Blackburn, D. Blair, S. Bloemen, O. Bock, T. P. Bodiya, M. Boer, G. Bogaert, C. Bogan, P. Bojtos, C. Bond, F. Bondu, L. Bonelli, R. Bonnand, R. Bork, M. Born, V. Boschi, Sukanta Bose, L. Bosi, C. Bradaschia, P. R. Brady, V. B. Braginsky, M. Branchesi, J. E. Brau, T. Briant, D. O. Bridges, A. Brillet, M. Brinkmann, V. Brisson, A. F. Brooks, D. A. Brown, D. D. Brown, F. Brückner, S. Buchman, A. Buikema, T. Bulik, H. J. Bulten, A. Buonanno, R. Burman, D. Buskulic, C. Buy, L. Cadonati, G. Cagnoli, J. Calderón Bustillo, E. Calloni, J. B. Camp, P. Campsie, K. C. Cannon, B. Canuel, J. Cao, C. D. Capano, F. Carbognani, L. Carbone, S. Caride, G. Castaldi, S. Caudill, M. Cavaglià, F. Cavalier, R. Cavalieri, C. Celerier, G. Cella, C. Cepeda,

E. Cesarini, R. Chakraborty, T. Chalermongsak, S. J. Chamberlin, S. Chao, P. Charlton, E. Chassande-Mottin, X. Chen, Y. Chen, A. Chincarini, A. Chiummo, H. S. Cho, M. Cho, J. H. Chow, N. Christensen, Q. Chu, S. S. Y. Chua, S. Chung, G. Ciani, F. Clara, D. E. Clark, J. A. Clark, J. H. Clayton, F. Cleva, E. Coccia, P. F. Cohadon, A. Colla, C. Collette, M. Colombini, L. Cominsky, M. Constancio, A. Conte, D. Cook, T. R. Corbitt, N. Cornish, A. Corsi, C. A. Costa, M. W. Coughlin, J. P. Coulon, S. Countryman, P. Couvares, D. M. Coward, M. J. Cowart, D. C. Coyne, R. Coyne, K. Craig, J. D. E. Creighton, R. P. Croce, S. G. Crowder, A. Cumming, L. Cunningham, E. Cuoco, C. Cutler, K. Dahl, T. Dal Canton, M. Damjanic, S. L. Danilishin, S. D'Antonio, K. Danzmann, V. Dattilo, H. Daveloza, M. Davier, G. S. Davies, E. J. Daw, R. Day, T. Dayanga, D. DeBra, G. Debreczeni, J. Degallaix, S. Deléglise, W. Del Pozzo, W. Del Pozzo, T. Dent, T. Dent, H. Dereli, V. Dergachev, R. De Rosa, R. T. DeRosa, R. DeSalvo, S. Dhurandhar, M. Díaz, J. Dickson, L. Di Fiore, A. Di Lieto, I. Di Palma, A. Di Virgilio, V. Dolique, E. Dominguez, F. Donovan, K. L. Dooley, S. Doravari, R. Douglas, T. P. Downes, M. Drago, R. W. P. Drever, J. C. Driggers, Z. Du, M. Ducrot, S. Dwyer, T. Eberle, T. Edo, M. Edwards, A. Effler, H. B. Eggenstein, P. Ehrens, J. Eichholz, S. S. Eikenberry, G. Endrőczy, R. Essick, T. Etzel, M. Evans, T. Evans, M. Factourovich, V. Fafone, S. Fairhurst, X. Fan, Q. Fang, S. Farinon, B. Farr, W. M. Farr, M. Favata, D. Fazi, H. Fehrmann, M. M. Fejer, D. Feldbaum, F. Feroz, I. Ferrante, E. C. Ferreira, F. Ferrini, F. Fidecaro, L. S. Finn, I. Fiori, R. P. Fisher, R. Flaminio, J. D. Fournier, S. Franco, S. Frasca, F. Frasconi, M. Frede, Z. Frei, A. Freise, R. Frey, T. T. Fricke, P. Fritschel, V. V. Frolov, P. Fulda, M. Fyffe, J. R. Gair, L. Gammaitoni, S. Gaonkar, F. Garufi, N. Gehrels, G. Gemme, B. Gendre, E. Genin, A. Gennai, S. Ghosh, J. A. Giaime, K. D. Giardina, A. Giazotto, J. Gleason, E. Goetz, R. Goetz, L. Gondan, G. González, N. Gordon, M. L. Gorodetsky, S. Gossan, S. Gößler, R. Gouaty, C. Gräf, P. B. Graff, M. Granata, A. Grant, S. Gras, C. Gray, R. J. S. Greenhalgh, A. M. Gretarsson, P. Groot, H. Grote, K. Grover, S. Grunewald, G. M. Guidi, C. J. Guido, K. Gushwa, E. K. Gustafson, R. Gustafson, J. Ha, E. D. Hall, W. Hamilton, D. Hammer, G. Hammond, M. Hanke, J. Hanks, C. Hanna, M. D. Hannam, J. Hanson, J. Harms, G. M. Harry, I. W. Harry, E. D. Harstad, M. Hart, M. T. Hartman, C. J. Haster, K. Haughian, A. Heidmann, M. Heintze, H. Heitmann, P. Hello, G. Hemming, M. Hendry, I. S. Heng, A. W. Heptonstall, M. Heurs, M. Hewitson, S. Hild, D. Hoak, K. A. Hodge, D. Hofman, K. Holt, P. Hopkins, T. Horrom, D. Hoske, D. J. Hosken, J. Hough, E. J. Howell, Y. Hu, E. Huerta, B. Hughey, S. Husa, S. H. Huttner, M. Huynh, T. Huynh-Dinh, A. Idrisy, D. R. Ingram, R. Inta, G. Islas, T. Isogai, A. Ivanov, B. R. Iyer, K. Izumi, M. Jacobson, H. Jang, P. Jaranowski, Y. Ji, F. Jiménez-Forteza, W. W. Johnson, D. I. Jones, R. Jones, R. J. G. Jonker, L. Ju, Haris K, P. Kalmus, V. Kalogera, S. Kandhasamy, G. Kang, J. B. Kanner, J. Karlen, M. Kasprzack, E. Katsavounidis, W. Katzman,

H. Kaufer, S. Kaufer, T. Kaur, K. Kawabe, F. Kawazoe, F. K  f  lian, G. M. Keiser, D. Keitel, D. B. Kelley, W. Kells, D. G. Keppel, A. Khalaidovski, F. Y. Khalili, E. A. Khazanov, C. Kim, K. Kim, N. G. Kim, N. Kim, S. Kim, Y. M. Kim, E. J. King, P. J. King, D. L. Kinzel, J. S. Kissel, S. Klimenko, J. Kline, S. Koehlenbeck, K. Kokeyama, V. Kondrashov, S. Koranda, W. Z. Korth, I. Kowalska, D. B. Kozak, V. Kringel, A. Kr  lak, G. Kuehn, A. Kumar, D. Nanda Kumar, P. Kumar, R. Kumar, L. Kuo, A. Kutynia, P. K. Lam, M. Landry, B. Lantz, S. Larson, P. D. Lasky, A. Lazzarini, C. Lazzaro, P. Leaci, S. Leavey, E. O. Lebigot, C. H. Lee, H. K. Lee, H. M. Lee, J. Lee, P. J. Lee, M. Leonardi, J. R. Leong, A. Le Roux, N. Leroy, N. Letendre, Y. Levin, B. Levine, J. Lewis, T. G. F. Li, K. Libbrecht, A. Libson, A. C. Lin, T. B. Littenberg, N. A. Lockerbie, V. Lockett, D. Lodhia, K. Loew, J. Logue, A. L. Lombardi, E. Lopez, M. Lorenzini, V. Lorette, M. Lormand, G. Losurdo, J. Lough, M. J. Lubinski, H. L  ck, A. P. Lundgren, Y. Ma, E. P. Macdonald, T. MacDonald, B. Machenschalk, M. MacInnis, D. M. Macleod, F. Maga  a-Sandoval, R. Magee, M. Mageswaran, C. Maglione, K. Mailand, E. Majorana, I. Maksimovic, V. Malvezzi, N. Man, G. M. Manca, I. Mandel, V. Mandic, V. Mangano, N. M. Mangini, G. Mansell, M. Mantovani, F. Marchesoni, F. Marion, S. M  rka, Z. M  rka, A. Markosyan, E. Maros, J. Marque, F. Martelli, I. W. Martin, R. M. Martin, L. Martinelli, D. Martynov, J. N. Marx, K. Mason, A. Masserot, T. J. Massinger, F. Matichard, L. Matone, N. Mavalvala, G. May, N. Mazumder, G. Mazzolo, R. McCarthy, D. E. McClelland, S. C. McGuire, G. McIntyre, J. McIver, K. McLin, D. Meacher, G. D. Meadors, M. Mehmet, J. Meidam, M. Meinders, A. Melatos, G. Mendell, R. A. Mercer, S. Meshkov, C. Messenger, M. S. Meyer, P. M. Meyers, F. Mezzani, H. Miao, C. Michel, E. E. Mikhailov, L. Milano, J. Miller, Y. Minenkov, C. M. F. Mingarelli, C. Mishra, S. Mitra, V. P. Mitrofanov, G. Mitselmakher, R. Mittleman, B. Moe, A. Moggi, M. Mohan, S. R. P. Mohapatra, D. Moraru, G. Moreno, N. Morgado, S. R. Morriss, K. Mossavi, B. Mours, C. M. Mow-Lowry, C. L. Mueller, G. Mueller, S. Mukherjee, A. Mullaevy, J. Munch, D. Murphy, P. G. Murray, A. Mytidis, M. F. Nagy, I. Nardecchia, L. Naticchioni, R. K. Nayak, V. Necula, G. Nelemans, I. Neri, M. Neri, G. Newton, T. Nguyen, A. B. Nielsen, S. Nissanke, A. H. Nitz, F. Nocera, D. Nolting, M. E. N. Normandin, L. K. Nuttall, E. Ochsner, J. O'Dell, E. Oelker, J. J. Oh, S. H. Oh, F. Ohme, S. Omar, P. Oppermann, R. Oram, B. O'Reilly, W. Ortega, R. O'Shaughnessy, C. Osthelder, D. J. Ottaway, R. S. Ottens, H. Overmier, B. J. Owen, C. Padilla, A. Pai, O. Palashov, C. Palomba, H. Pan, Y. Pan, C. Pankow, F. Paoletti, M. A. Papa, H. Paris, A. Pasqualetti, R. Passaquieti, D. Passuello, M. Pedraza, A. Pele, S. Penn, A. Perreca, M. Phelps, M. Pichot, M. Pickenpack, F. Piergiovanni, V. Pierro, L. Pinard, I. M. Pinto, M. Pitkin, J. Poeld, R. Poggiani, A. Poteomkin, J. Powell, J. Prasad, V. Predoi, S. Premachandra, T. Prestegard, L. R. Price, M. Prijatelj, S. Privitera, G. A. Prodi, L. Prokhorov, O. Puncken, M. Punturo, P. Puppato, M. P  rrer, J. Qin, V. Quetschke, E. Quintero,

R. Quitzow-James, F. J. Raab, D. S. Rabeling, I. Rácz, H. Radkins, P. Raffai, S. Raja, G. Rajalakshmi, M. Rakhmanov, C. Ramet, K. Ramirez, P. Rapagnani, V. Raymond, M. Razzano, V. Re, S. Recchia, C. M. Reed, T. Regimbau, S. Reid, D. H. Reitze, O. Reula, E. Rhoades, F. Ricci, R. Riesen, K. Riles, N. A. Robertson, F. Robinet, A. Rocchi, S. B. Roddy, L. Rolland, J. G. Rollins, R. Romano, G. Romanov, J. H. Romie, D. Rosińska, S. Rowan, A. Rüdiger, P. Ruggi, K. Ryan, F. Salemi, L. Sammut, V. Sandberg, J. R. Sanders, S. Sankar, V. Sannibale, I. Santiago-Prieto, E. Saracco, B. Sassolas, B. S. Sathyaprakash, P. R. Saulson, R. Savage, J. Scheuer, R. Schilling, M. Schilman, P. Schmidt, R. Schnabel, R. M. S. Schofield, E. Schreiber, D. Schuette, B. F. Schutz, J. Scott, S. M. Scott, D. Sellers, A. S. Sengupta, D. Sentenac, V. Sequino, A. Sergeev, D. A. Shaddock, S. Shah, M. S. Shahriar, M. Shaltev, Z. Shao, B. Shapiro, P. Shawhan, D. H. Shoemaker, T. L. Sidery, K. Siellez, X. Siemens, D. Sigg, D. Simakov, A. Singer, L. Singer, R. Singh, A. M. Sintes, B. J. J. Slagmolen, J. Slutsky, J. R. Smith, M. R. Smith, R. J. E. Smith, N. D. Smith-Lefebvre, E. J. Son, B. Sorazu, T. Souradeep, A. Staley, J. Stebbins, M. Steinke, J. Steinlechner, S. Steinlechner, B. C. Stephens, S. Steplewski, S. Stevenson, R. Stone, D. Stops, K. A. Strain, N. Straniero, S. Strigin, R. Sturani, A. L. Stuver, T. Z. Summerscales, S. Susmithan, P. J. Sutton, B. Swinkels, M. Tacca, D. Talukder, D. B. Tanner, J. Tao, S. P. Tarabrin, R. Taylor, G. Tellez, M. P. Thirugnanasambandam, M. Thomas, P. Thomas, K. A. Thorne, K. S. Thorne, E. Thrane, V. Tiwari, K. V. Tokmakov, C. Tomlinson, M. Tonelli, C. V. Torres, C. I. Torrie, F. Travasso, G. Traylor, M. Tse, D. Tshilumba, H. Tuennermann, D. Ugolini, C. S. Unnikrishnan, A. L. Urban, S. A. Usman, H. Vahlbruch, G. Vajente, G. Valdes, M. Vallisneri, M. van Beuzekom, J. F. J. van den Brand, C. Van Den Broeck, M. V. van der Sluys, J. van Heijningen, A. A. van Veggel, S. Vass, M. Vasúth, R. Vaulin, A. Vecchio, G. Vedovato, J. Veitch, P. J. Veitch, K. Venkateswara, D. Verkindt, F. Vetrano, A. Viceré, R. Vincent-Finley, J. Y. Vinet, S. Vitale, T. Vo, H. Vocca, C. Vorvick, W. D. Vousden, S. P. Vyachanin, A. R. Wade, L. Wade, M. Wade, M. Walker, L. Wallace, S. Walsh, M. Wang, X. Wang, R. L. Ward, M. Was, B. Weaver, L. W. Wei, M. Weinert, A. J. Weinstein, R. Weiss, T. Welborn, L. Wen, P. Wessels, M. West, T. Westphal, K. Wette, J. T. Whelan, D. J. White, B. F. Whiting, K. Wiesner, C. Wilkinson, K. Williams, L. Williams, R. Williams, T. D. Williams, A. R. Williamson, J. L. Willis, B. Willke, M. Wimmer, W. Winkler, C. C. Wipf, A. G. Wiseman, H. Wittel, G. Woan, N. Wolovick, J. Worden, Y. Wu, J. Yablon, I. Yakushin, W. Yam, H. Yamamoto, C. C. Yancey, H. Yang, S. Yoshida, M. Yvert, A. Zadrożny, M. Zanolin, J. P. Zendri, Fan Zhang, L. Zhang, C. Zhao, H. Zhu, X. J. Zhu, M. E. Zucker, S. Zuraw, J. Zweizig, and IceCube Collaboration. Multimessenger search for sources of gravitational waves and high-energy neutrinos: Initial results for LIGO-Virgo and IceCube. *Phys. Rev. D*, 90(10):102002, November 2014. doi: 10.1103/PhysRevD.90.102002.

M. G. Aartsen, M. Ackermann, J. Adams, J. A. Aguilar, M. Ahlers, M. Ahrens, C. Alispach, K. Andeen, T. Anderson, I. Anseau, G. Anton, C. Argüelles, J. Auffenberg, S. Axani, H. Bagherpour, X. Bai, A. Balagopal V., A. Barbano, S. W. Barwick, B. Bastian, V. Baum, S. Baur, R. Bay, J. J. Beatty, K. H. Becker, J. Becker Tjus, S. BenZvi, D. Berley, E. Bernardini, D. Z. Besson, G. Binder, D. Bindig, E. Blaufuss, S. Blot, C. Boehm, S. Böser, O. Botner, J. Böttcher, E. Bourbeau, J. Bourbeau, F. Bradascio, J. Braun, S. Bron, J. Brostean-Kaiser, A. Burgman, J. Buscher, R. S. Busse, T. Carver, C. Chen, E. Cheung, D. Chirkin, S. Choi, B. A. Clark, K. Clark, L. Classen, A. Coleman, G. H. Collin, J. M. Conrad, P. Coppin, P. Correa, D. F. Cowen, R. Cross, P. Dave, C. De Clercq, J. J. DeLaunay, H. Dembinski, K. Deoskar, S. De Ridder, P. Desiati, K. D. de Vries, G. de Wasseige, M. de With, T. DeYoung, A. Diaz, J. C. Díaz-Vélez, H. Dujmovic, M. Dunkman, E. Dvorak, B. Eberhardt, T. Ehrhardt, P. Eller, R. Engel, P. A. Evenson, S. Fahey, A. R. Fazely, J. Felde, K. Filimonov, C. Finley, D. Fox, A. Franckowiak, E. Friedman, A. Fritz, T. K. Gaisser, J. Gallagher, E. Ganster, S. Garrappa, L. Gerhardt, K. Ghorbani, T. Glauch, T. Glüsenkamp, A. Goldschmidt, J. G. Gonzalez, D. Grant, T. Grégoire, Z. Griffith, S. Griswold, M. Günder, M. Gündüz, C. Haack, A. Hallgren, R. Halliday, L. Halve, F. Halzen, K. Hanson, A. Haungs, D. Hebecker, D. Heereman, P. Heix, K. Helbing, R. Hellauer, F. Henningsen, S. Hickford, J. Hignight, G. C. Hill, K. D. Hoffman, R. Hoffmann, T. Hoinka, B. Hokanson-Fasig, K. Hoshina, F. Huang, M. Huber, T. Huber, K. Hultqvist, M. Hünnefeld, R. Hussain, S. In, N. Iovine, A. Ishihara, M. Jansson, G. S. Japaridze, M. Jeong, K. Jero, B. J. P. Jones, F. Jonske, R. Joppe, D. Kang, W. Kang, A. Kappes, D. Kappesser, T. Karg, M. Karl, A. Karle, U. Katz, M. Kauer, M. Kellermann, J. L. Kelley, A. Kheirandish, J. Kim, T. Kintscher, J. Kiryluk, T. Kittler, S. R. Klein, R. Koirala, H. Kolanoski, L. Köpke, C. Kopper, S. Kopper, D. J. Koskinen, M. Kowalski, K. Krings, G. Krückl, N. Kulacz, N. Kurahashi, A. Kyriacou, J. L. Lanfranchi, M. J. Larson, F. Lauber, J. P. Lazar, K. Leonard, A. Leszczyńska, Q. R. Liu, E. Lohfink, C. J. Lozano Mariscal, L. Lu, F. Lucarelli, A. Ludwig, J. Lünemann, W. Luszczak, Y. Lyu, W. Y. Ma, J. Madsen, G. Maggi, K. B. M. Mahn, Y. Makino, P. Mallik, K. Mallot, S. Mancina, I. C. Mariş, R. Maruyama, K. Mase, R. Maunu, F. McNally, K. Meagher, M. Medici, A. Medina, M. Meier, S. Meighen-Berger, G. Merino, T. Meures, J. Micallef, D. Mockler, G. Momenté, T. Montaruli, R. W. Moore, R. Morse, M. Moulai, P. Muth, R. Nagai, U. Naumann, G. Neer, L. V. Nguyêñ, H. Niederhausen, M. U. Nisa, S. C. Nowicki, D. R. Nygren, A. Obertacke Pollmann, M. Oehler, A. Olivas, A. O’Murchadha, E. O’Sullivan, T. Palczewski, H. Pandya, D. V. Pankova, N. Park, P. Peiffer, C. Pérez de los Heros, S. Philippen, D. Pieloth, S. Pieper, E. Pinat, A. Pizzuto, M. Plum, A. Porcelli, P. B. Price, G. T. Przybylski, C. Raab, A. Raissi, M. Rameez, L. Rauch, K. Rawlins, I. C. Rea, A. Rehman, R. Reimann, B. Relethford, M. Renschler, G. Renzi, E. Resconi,

- W. Rhode, M. Richman, S. Robertson, M. Rongen, C. Rott, T. Ruhe, D. Ryckbosch, D. Rysewyk Cantu, I. Safa, S. E. Sanchez Herrera, A. Sand rock, J. Sandroos, M. Santander, S. Sarkar, S. Sarkar, K. Satalecka, M. Schaufel, H. Schieler, P. Schlunder, T. Schmidt, A. Schneider, J. Schneider, F. G. Schröder, L. Schumacher, S. Sclafani, D. Seckel, S. Seunarine, S. Shefali, M. Silva, R. Snihur, J. Soedingrekso, D. Soldin, M. Song, G. M. Spiczak, C. Spiering, J. Stachurska, M. Stamatikos, T. Stanev, R. Stein, J. Stettner, A. Steuer, T. Stezelberger, R. G. Stokstad, A. Stöbl, N. L. Strotjohann, T. Stürwald, T. Stuttard, G. W. Sullivan, I. Taboada, F. Tenholt, S. TerAntonyan, A. Terliuk, S. Tilav, K. Tollefson, L. Tomankova, C. Tönnis, S. Toscano, D. Tosi, A. Trettin, M. Tselengidou, C. F. Tung, A. Turcati, R. Turcotte, C. F. Turley, B. Ty, E. Unger, M. A. Unland Elorrieta, M. Usner, J. Vandenbroucke, W. Van Driessche, D. van Eijk, N. van Eijndhoven, J. van Santen, S. Verpoest, M. Vraeghe, C. Walck, A. Wallace, M. Wallraff, N. Wandkowsky, T. B. Watson, C. Weaver, A. Weindl, M. J. Weiss, J. Weldert, C. Wendt, J. Werthebach, B. J. Whelan, N. Whitehorn, K. Wiebe, C. H. Wiebusch, L. Wille, D. R. Williams, L. Wills, M. Wolf, J. Wood, T. R. Wood, K. Woschnagg, G. Wrede, D. L. Xu, X. W. Xu, Y. Xu, J. P. Yanez, G. Yodh, S. Yoshida, T. Yuan, M. Zöcklein, and IceCube Collaboration. IceCube Search for High-energy Neutrino Emission from TeV Pulsar Wind Nebulae. *Astrophys. J.*, 898(2):117, August 2020. doi: 10.3847/1538-4357/ab9fa0.
- A. A. Abdo, M. Ackermann, M. Ajello, W. B. Atwood, M. Axelsson, L. Baldini, J. Ballet, G. Barbiellini, D. Bastieri, and M. Battelino. Measurement of the Cosmic Ray  $e^+e^-$  Spectrum from 20GeV to 1TeV with the Fermi Large Area Telescope. *Physical Review Letters*, 102(18):181101, May 2009. doi: 10.1103/PhysRevLett.102.181101.
- A. U. Abeysekara, A. Albert, R. Alfaro, C. Alvarez, J. D. Álvarez, J. R. Angeles Camacho, R. Arceo, J. C. Arteaga-Velázquez, K. P. Arunbabu, D. Avila Rojas, H. A. Ayala Solares, V. Baghmany, E. Belmont-Moreno, S. Y. BenZvi, C. Brisbois, K. S. Caballero-Mora, T. Capistrán, A. Carramiñana, S. Casanova, U. Cotti, J. Cotzomi, S. Coutiño de León, E. De la Fuente, C. de León, S. Dichiara, B. L. Dingus, M. A. DuVernois, J. C. Díaz-Vélez, R. W. Ellsworth, K. Engel, C. Espinoza, B. Fick, H. Fleischhack, N. Fraija, A. Galván-Gámez, J. A. García-González, F. Garfias, M. M. González, J. A. Goodman, J. P. Harding, S. Hernandez, J. Hinton, B. Hona, F. Hueyotl-Zahuantitla, C. M. Hui, P. Hüntemeyer, A. Iriarte, A. Jardin-Blicq, V. Joshi, S. Kaufmann, D. Kieda, A. Lara, W. H. Lee, H. León Vargas, J. T. Linnemann, A. L. Longinotti, G. Luis-Raya, J. Lundeen, K. Malone, S. S. Marinelli, O. Martinez, I. Martinez-Castellanos, J. Martínez-Castro, H. Martínez-Huerta, J. A. Matthews, P. Miranda-Romagnoli, J. A. Morales-Soto, E. Moreno, M. Mostafá, A. Nayerhoda, L. Nellen, M. Newbold, M. U. Nisa, R. Noriega-Papaqui,

- A. Peisker, E. G. Pérez-Pérez, J. Pretz, Z. Ren, C. D. Rho, C. Rivière, D. Rosa-González, M. Rosenberg, E. Ruiz-Velasco, H. Salazar, F. Salesa Greus, A. Sandoval, M. Schneider, H. Schoorlemmer, M. Seglar Arroyo, G. Sinnis, A. J. Smith, R. W. Springer, P. Surajbali, E. Tabachnick, M. Tanner, O. Tibolla, K. Tollefson, I. Torres, T. Weisgarber, S. Westerhoff, J. Wood, T. Yapici, A. Zepeda, H. Zhou, and HAWC Collaboration. Measurement of the Crab Nebula Spectrum Past 100 TeV with HAWC. *Astrophys. J.*, 881(2):134, Aug 2019. doi: 10.3847/1538-4357/ab2f7d.
- Abraham Achterberg, Yves A. Gallant, John G. Kirk, and Axel W. Guthmann. Particle acceleration by ultrarelativistic shocks: theory and simulations. *Month. Not. Roy. Astr. Soc.*, 328(2):393–408, Dec 2001a. doi: 10.1046/j.1365-8711.2001.04851.x.
- Abraham Achterberg, Yves A. Gallant, John G. Kirk, and Axel W. Guthmann. Particle acceleration by ultrarelativistic shocks: theory and simulations. *Month. Not. Roy. Astr. Soc.*, 328(2):393–408, Dec 2001b. doi: 10.1046/j.1365-8711.2001.04851.x.
- M. Ackermann, M. Ajello, A. Allafort, W. B. Atwood, M. Axelsson, L. Baldini, G. Barbiellini, D. Bastieri, K. Bechtol, R. Bellazzini, B. Berenji, E. D. Bloom, E. Bonamente, A. W. Borgland, A. Bouvier, J. Bregeon, A. Brez, M. Brigida, P. Bruel, R. Buehler, S. Buson, G. A. Caliendo, R. A. Cameron, P. A. Caraveo, J. M. Casandjian, C. Cecchi, E. Charles, A. Chekhtman, J. Chiang, S. Ciprini, R. Claus, J. Cohen-Tanugi, S. Cutini, F. de Palma, C. D. Dermer, S. W. Digel, E. Do Couto E Silva, P. S. Drell, A. Drlica-Wagner, R. Dubois, T. Enoto, L. Falletti, C. Favuzzi, S. J. Fegan, W. B. Focke, P. Fortin, Y. Fukazawa, S. Funk, P. Fusco, F. Gargano, N. Gehrels, S. Germani, N. Giglietto, F. Giordano, M. Giroletti, T. Glanzman, G. Godfrey, I. A. Grenier, J. E. Grove, S. Guiriec, D. Hadasch, M. Hayashida, E. Hays, R. E. Hughes, G. Jóhannesson, A. S. Johnson, T. J. Johnson, T. Kamae, H. Katagiri, J. Kataoka, J. Knödseder, M. Kuss, J. Lande, L. Latronico, S. H. Lee, F. Longo, F. Loparco, M. N. Lovellette, P. Lubrano, G. M. Madejski, M. N. Mazziotta, J. E. McEnery, P. F. Michelson, T. Mizuno, A. A. Moiseev, C. Monte, M. E. Monzani, A. Morselli, I. V. Moskalenko, S. Murgia, T. Nakamori, M. Naumann-Godo, P. L. Nolan, J. P. Norris, E. Nuss, T. Ohsugi, A. Okumura, N. Omodei, E. Orlando, J. F. Ormes, M. Ozaki, D. Paneque, J. H. Panetta, D. Parent, M. Pesce-Rollins, M. Pierbattista, F. Piron, S. Rainò, R. Rando, M. Razzano, A. Reimer, O. Reimer, T. Reposeur, S. Ritz, L. S. Rochester, C. Sgrò, E. J. Siskind, P. D. Smith, G. Spandre, P. Spinelli, D. J. Suson, H. Takahashi, T. Tanaka, J. G. Thayer, J. B. Thayer, D. J. Thompson, L. Tibaldo, G. Tosti, E. Troja, T. L. Usher, J. Vandenbroucke, V. Vasileiou, G. Vianello, N. Vilchez, V. Vitale, A. P. Waite, P. Wang, B. L. Winer, K. S. Wood, Z. Yang, and S. Zimmer. In-flight measurement of the absolute energy scale of the

- Fermi Large Area Telescope. *Astroparticle Physics*, 35(6):346–353, Jan 2012. doi: 10.1016/j.astropartphys.2011.10.007.
- M. Ackermann, M. Ajello, L. Baldini, J. Ballet, G. Barbiellini, D. Bastieri, R. Bellazzini, E. Bissaldi, R. D. Blandford, E. D. Bloom, R. Bonino, E. Bottacini, T. J. Brandt, J. Bregeon, P. Bruel, R. Buehler, R. A. Cameron, R. Caputo, P. A. Caraveo, D. Castro, E. Cavazzuti, E. Charles, C. C. Cheung, G. Chiaro, S. Ciprini, J. Cohen-Tanugi, D. Costantin, S. Cutini, F. D’Ammando, F. de Palma, A. Desai, N. Di Lalla, M. Di Mauro, L. Di Venere, C. Favuzzi, J. Finke, A. Franckowiak, Y. Fukazawa, S. Funk, P. Fusco, F. Gargano, D. Gasparri, N. Giglietto, F. Giordano, M. Giroletti, D. Green, I. A. Grenier, L. Guillemot, S. Guiriec, E. Hays, J. W. Hewitt, D. Horan, G. Jóhannesson, S. Kensei, M. Kuss, S. Larsson, L. Latronico, M. Lemoine-Goumard, J. Li, F. Longo, F. Loparco, M. N. Lovellette, P. Lubrano, J. D. Magill, S. Maldera, A. Manfreda, M. N. Mazziotta, J. E. McEnery, M. Meyer, T. Mizuno, M. E. Monzani, A. Morselli, I. V. Moskalenko, M. Negro, E. Nuss, N. Omodei, M. Orienti, E. Orlando, J. F. Ormes, M. Palatiello, V. S. Paliya, D. Paneque, J. S. Perkins, M. Persic, M. Pesce-Rollins, F. Piron, T. A. Porter, G. Principe, S. Rainò, R. Rando, B. Rani, S. Razzaque, A. Reimer, O. Reimer, T. Reposeur, C. Sgrò, E. J. Siskind, G. Spandre, P. Spinelli, D. J. Suson, H. Tajima, J. B. Thayer, L. Tibaldo, D. F. Torres, G. Tosti, J. Valverde, T. M. Venters, M. Vogel, K. Wood, M. Wood, G. Zaharijas, Fermi-LAT Collaboration, and J. Biteau. The Search for Spatial Extension in High-latitude Sources Detected by the Fermi Large Area Telescope. *The Astrophys. J. Supp.*, 237:32, August 2018. doi: 10.3847/1538-4365/aacdf7.
- F. Aharonian, A. Akhperjanian, M. Beilicke, K. Bernlöhr, H. G. Börst, H. Bojahr, O. Bolz, T. Coarasa, J. L. Contreras, J. Cortina, S. Denninghoff, M. V. Fonseca, M. Girma, N. Götting, G. Heinzlmann, G. Hermann, A. Heusler, W. Hofmann, D. Horns, I. Jung, R. Kankanyan, M. Kestel, A. Kohnle, A. Konopelko, D. Kranich, H. Lampeitl, M. Lopez, E. Lorenz, F. Lucarelli, O. Mang, D. Mazin, H. Meyer, R. Mirzoyan, A. Moralejo, E. Oña-Wilhelmi, M. Panter, A. Plyasheshnikov, G. Pühlhofer, R. de los Reyes, W. Rhode, J. Ripken, G. Rowell, V. Sahakian, M. Samorski, M. Schilling, M. Siems, D. Sobzynska, W. Stamm, M. Tluczykont, V. Vitale, H. J. Völk, C. A. Wiedner, and W. Wittek. The Crab Nebula and Pulsar between 500 GeV and 80 TeV: Observations with the HEGRA Stereoscopic Air Cerenkov Telescopes. *Astrophys. J.*, 614(2):897–913, Oct 2004a. doi: 10.1086/423931.
- F. Aharonian, A. Akhperjanian, M. Beilicke, K. Bernlöhr, H.-G. Börst, H. Bojahr, O. Bolz, T. Coarasa, J. L. Contreras, J. Cortina, S. Denninghoff, M. V. Fonseca, M. Girma, N. Götting, G. Heinzlmann, G. Hermann, A. Heusler, W. Hofmann, D. Horns, I. Jung, R. Kankanyan, M. Kestel, A. Kohnle, A. Konopelko, D. Kranich,

- H. Lampeitl, M. Lopez, E. Lorenz, F. Lucarelli, O. Mang, D. Mazin, H. Meyer, R. Mirzoyan, A. Moralejo, E. Oña-Wilhelmi, M. Panter, A. Plyasheshnikov, G. Pühlhofer, R. de los Reyes, W. Rhode, J. Ripken, G. Rowell, V. Sahakian, M. Samorski, M. Schilling, M. Siems, D. Sobzynska, W. Stamm, M. Tluczykont, V. Vitale, H. J. Völk, C. A. Wiedner, and W. Wittek. The Crab Nebula and Pulsar between 500 GeV and 80 TeV: Observations with the HEGRA Stereoscopic Air Cerenkov Telescopes. *Astrophys. J.*, 614:897–913, October 2004b. doi: 10.1086/423931.
- F. A. Aharonian and S. V. Bogovalov. Exploring physics of rotation powered pulsars with sub-10 GeV imaging atmospheric Cherenkov telescopes. *New Astronomy*, 8(2): 85–103, Feb 2003. doi: 10.1016/S1384-1076(02)00200-2.
- Sebastiano Aiello, Arnauld Albert, Sergio Alves Garre, Zineb Aly, Fabrizio Ameli, Michel Andre, Giorgos Androulakis, Marco Anghinolfi, Mancia Anguita, Gisela Anton, Miquel Ardid, Julien Aublin, Christos Bagatelas, Giancarlo Barbarino, Bruny Baret, Suzan Basegmez du Pree, Meriem Bendahman, Edward Berbee, Vincent Bertin, Simone Biagi, Andrea Biagioni, Matthias Bissinger, Markus Boettcher, Jihad Boumaaza, Mohammed Bouta, Mieke Bouwhuis, Cristiano Bozza, Horea Branzas, Ronald Bruijn, Jürgen Brunner, Ernst-Jan Buis, Raffaele Buompane, Jose Busto, Barbara Caiffi, David Calvo, Antonio Capone, Víctor Carretero, Paolo Castaldi, Silvia Celli, Mohamed Chabab, Nhan Chau, Andrew Chen, Silvio Cherubini, Vitaliano Chiarella, Tommaso Chiarusi, Marco Circella, Rosanna Cocimano, Joao Coelho, Alexis Coleiro, Marta Colomer Molla, Rosa Coniglione, Paschal Coyle, Alexandre Creusot, Giacomo Cuttone, Antonio D’Onofrio, Richard Dallier, Maarten de Jong, Paul de Jong, Mauro De Palma, Gwenhaël de Wasseige, Els de Wolf, Irene Di Palma, Antonio Diaz, Dídac Diego-Tortosa, Carla Distefano, Alba Domi, Roberto Donà, Corinne Donzaud, Damien Dornic, Manuel Dörr, Doriane Drouhin, Thomas Eberl, Imad El Bojaddaini, Dominik Elsaesser, Alexander Enzenhöfer, Paolo Fermani, Giovanna Ferrara, Miroslav Filipovic, Francesco Filippini, Luigi Antonio Fusco, Omar Gabella, Tamas Gal, Alfonso Andres Garcia Soto, Fabio Garufi, Yoann Gatelet, Nicole Geißelbrecht, Lucio Gialanella, Emidio Giorgio, Sara Rebecca Gozzini, Rodrigo Gracia, Kay Graf, Dario Grasso, Giuseppe Grella, Carlo Guidi, Steffen Hallmann, Hassane Hamdaoui, Aart Heijboer, Amar Hekalo, Juan-Jose Hernandez-Rey, Jannik Hofestädt, Feifei Huang, Walid Idrissi Ibnsalih, Giulia Illuminati, Clancy James, Bouke Jisse Jung, Matthias Kadler, Piotr Kalaczyński, Oleg Kalekin, Uli Katz, Nafis Rezwan Khan Chowdhury, Giorgi Kistauri, Els Koffeman, Paul Kooijman, Antoine Kouchner, Michael Kreter, Vladimir Kulikovskiy, Robert Lahmann, Giuseppina Larosa, Remy Le Breton, Ornella Leonardi, Francesco Leone, Emanuele Leonora, Giuseppe Levi, Massimiliano Lincetto, Miles Lindsey Clark, Thomas Lipreau, Alessandro Lonardo, Fabio Longhitano, Daniel Lopez Coto, Lukas

Maderer, Jerzy Mańczak, Karl Mannheim, Annarita Margiotta, Antonio Marinelli, Christos Markou, Lilian Martin, Juan Antonio Martínez-Mora, Agnese Martini, Fabio Marzaioli, Stefano Mastroianni, Safaa Mazzou, Karel Melis, Gennaro Miele, Pasquale Migliozi, Emilio Migneco, Piotr Mijakowski, Luis Salvador Miranda Palacios, Carlos Maximiliano Mollo, Mauro Morganti, Michael Moser, Abdelilah Moussa, Rasa Muller, Mario Musumeci, Lodewijk Nauta, Sergio Navas, Carlo Alessandro Nicolau, Brían Ó Fearraigh, Mukharbek Organokov, Angelo Orlando, Gogita Papalashvili, Riccardo Papaleo, Cosimo Pastore, Alice Paun, Gabriela Emilia Pavalas, Carmelo Pellegrino, Mathieu Perrin-Terrin, Paolo Piattelli, Camiel Pieterse, Konstantinos Pikounis, Ofelia Pisanti, Chiara Poirè, Vlad Popa, Maarten Post, Thierry Pradier, Gerd Pühlhofer, Sara Pulvirenti, Omphile Rabyang, Fabrizio Raffaelli, Nunzio Randazzo, Antonio Raponi, Soebur Razzaque, Diego Real, Stefan Reck, Giorgio Riccobene, Marc Richer, Stephane Rivoire, Alberto Rovelli, Francisco Salesa Greus, Dorothea Franziska Elisabeth Samtleben, Agustín Sánchez Losa, Matteo Sanguineti, Andrea Santangelo, Domenico Santonocito, Piera Sapienza, Jutta Schnabel, Jordan Seneca, Irene Sgura, Rezo Shanidze, Ankur Sharma, Francesco Simeone, Anna Sinopoulou, Bernardino Spisso, Maurizio Spurio, Dimitris Stavropoulos, Jos Steijger, Simona Maria Stellacci, Mauro Taiuti, Yahya Tayalati, Enrique Tenllado, Tarak Thakore, Steven Tingay, Ekaterini Tzamariudaki, Dimitrios Tzanetatos, Ad van den Berg, Frits van der Knaap, Daan van Eijk, Véronique Van Elewyck, Hans van Haren, Godefroy Vannoye, George Vasileiadis, Federico Versari, Salvatore Viola, Daniele Vivolo, Joern Wilms, Rafał Wojaczyński, Dmitry Zaborov, Sandra Zavatarelli, Angela Zegarelli, Daniele Zito, Juan-de-Dios Zornoza, Juan Zúñiga, and Natalia Zywuca. Event reconstruction for KM3NeT/ORCA using convolutional neural networks. *arXiv e-prints*, art. arXiv:2004.08254, April 2020.

J. Aleksić, S. Ansoldi, L. A. Antonelli, P. Antoranz, A. Babic, P. Bangale, J. A. Barrio, J. Becerra González, W. Bednarek, E. Bernardini, B. Biasuzzi, A. Biland, O. Blanch, S. Bonnefoy, G. Bonnoli, F. Borracci, T. Bretz, E. Carmona, A. Carosi, P. Colin, E. Colombo, J. L. Contreras, J. Cortina, S. Covino, P. Da Vela, F. Dazzi, A. De Angelis, G. De Caneva, B. De Lotto, E. de Oña Wilhelmi, C. Delgado Mendez, M. Doert, D. Dominis Prester, D. Dorner, M. Doro, S. Einecke, D. Eisenacher, D. Elsaesser, M. V. Fonseca, L. Font, K. Frantzen, C. Fruck, D. Galindo, R. J. García López, M. Garczarczyk, D. Garrido Terrats, M. Gaug, N. Godinović, A. González Muñoz, S. R. Gozzini, D. Hadasch, Y. Hanabata, M. Hayashida, J. Herrera, D. Hildebrand, J. Hose, D. Hrupec, W. Idec, V. Kadenius, H. Kellermann, K. Kodani, Y. Konno, J. Krause, H. Kubo, J. Kushida, A. La Barbera, D. Lelas, N. Lewandowska, E. Lindfors, S. Lombardi, M. López, R. López-Coto, A. López-Oramas, E. Lorenz, I. Lozano, M. Makariev, K. Mallot, G. Maneva, N. Mankuzhiyil, K. Mannheim, L. Maraschi,

- B. Marcote, M. Mariotti, M. Martínez, D. Mazin, U. Menzel, J. M. Miranda, R. Mirzoyan, A. Moralejo, P. Munar-Adrover, D. Nakajima, A. Niedzwiecki, K. Nilsson, K. Nishijima, K. Noda, N. Nowak, R. Orito, A. Overkemping, S. Paiano, M. Palatiello, D. Paneque, R. Paoletti, J. M. Paredes, X. Paredes-Fortuny, M. Persic, P. G. Prada Moroni, E. Prandini, S. Preziuso, I. Puljak, R. Reinthal, W. Rhode, M. Ribó, J. Rico, J. Rodriguez Garcia, S. Rügamer, A. Saggion, T. Saito, K. Saito, K. Satalecka, V. Scalzotto, V. Scapin, C. Schultz, T. Schweizer, S. N. Shore, A. Sillanpää, J. Sitarek, I. Snidaric, D. Sobczynska, F. Spanier, V. Stamatescu, A. Stamerra, T. Steinbring, J. Storz, M. Strzys, L. Takalo, H. Takami, F. Tavecchio, P. Temnikov, T. Terzić, D. Tesaro, M. Teshima, J. Thaele, O. Tibolla, D. F. Torres, T. Toyama, A. Treves, M. Uellenbeck, P. Vogler, R. M. Wagner, R. Zanin, D. Horns, J. Martín, and M. Meyer. Measurement of the Crab Nebula spectrum over three decades in energy with the MAGIC telescopes. *Journal of High Energy Astrophysics*, 5:30–38, March 2015. doi: 10.1016/j.jheap.2015.01.002.
- M. Amenomori, Y. W. Bao, X. J. Bi, D. Chen, T. L. Chen, W. Y. Chen, Xu Chen, Y. Chen, Cirennima, S. W. Cui, Danzengluobu, L. K. Ding, J. H. Fang, K. Fang, C. F. Feng, Zhaoyang Feng, Z. Y. Feng, Qi Gao, Q. B. Gou, Y. Q. Guo, H. H. He, Z. T. He, K. Hibino, N. Hotta, Haibing Hu, H. B. Hu, J. Huang, H. Y. Jia, L. Jiang, H. B. Jin, F. Kajino, K. Kasahara, Y. Katayose, C. Kato, S. Kato, K. Kawata, M. Kozai, Labaciren, G. M. Le, A. F. Li, H. J. Li, W. J. Li, Y. H. Lin, B. Liu, C. Liu, J. S. Liu, M. Y. Liu, Y. Q. Lou, H. Lu, X. R. Meng, H. Mitsui, K. Munakata, Y. Nakamura, H. Nanjo, M. Nishizawa, M. Ohnishi, I. Ohta, S. Ozawa, X. L. Qian, X. B. Qu, T. Saito, M. Sakata, T. K. Sako, Y. Sengoku, J. Shao, M. Shibata, A. Shiomi, H. Sugimoto, M. Takita, Y. H. Tan, N. Tateyama, S. Torii, H. Tsuchiya, S. Udo, H. Wang, H. R. Wu, L. Xue, K. Yagisawa, Y. Yamamoto, Z. Yang, A. F. Yuan, L. M. Zhai, H. M. Zhang, J. L. Zhang, X. Zhang, X. Y. Zhang, Y. Zhang, Yi Zhang, Ying Zhang, Zhaxisangzhu, and X. X. Zhou. First Detection of Photons with Energy Beyond 100 TeV from an Astrophysical Source. *arXiv e-prints*, art. arXiv:1906.05521, Jun 2019.
- Jonathan Arons. Pulsars as Gamma-Rays Sources: Nebular Shocks and Magnetospheric Gaps. *Space Science Reviews*, 75(1-2):235–255, Jan 1996. doi: 10.1007/BF00195037.
- Jonathan Arons and Marco Tavani. Relativistic Particle Acceleration in Plerions. *The Astrophys. J. Supp.*, 90:797, Feb 1994. doi: 10.1086/191905.
- A. M. Atoyan. Radio spectrum of the Crab nebula as an evidence for fast initial spin of its pulsar. *Astr. Astrophys.*, 346:L49–L52, June 1999.
- A. M. Atoyan and F. A. Aharonian. On the mechanisms of gamma radiation in the Crab Nebula. *Month. Not. Roy. Astr. Soc.*, 278:525–541, January 1996a. doi: 10.1093/mnras/278.2.525.

- A. M. Atoyan and F. A. Aharonian. On the mechanisms of gamma radiation in the Crab Nebula. *Month. Not. Roy. Astr. Soc.*, 278(2):525–541, January 1996b. doi: 10.1093/mnras/278.2.525.
- W. B. Atwood, A. A. Abdo, M. Ackermann, W. Althouse, B. Anderson, M. Axelsson, L. Baldini, J. Ballet, D. L. Band, G. Barbiellini, J. Bartelt, D. Bastieri, B. M. Baughman, K. Bechtol, D. Bédérède, F. Bellardi, R. Bellazzini, B. Berenji, G. F. Bignami, D. Bisello, E. Bissaldi, R. D. Blandford, E. D. Bloom, J. R. Bogart, E. Bonamente, J. Bonnell, A. W. Borgland, A. Bouvier, J. Bregeon, A. Brez, M. Brigida, P. Bruel, T. H. Burnett, G. Busetto, G. A. Caliandro, R. A. Cameron, P. A. Caraveo, S. Carius, P. Carlson, J. M. Casandjian, E. Cavazzuti, M. Ceccanti, C. Cecchi, E. Charles, A. Chekhtman, C. C. Cheung, J. Chiang, R. Chipaux, A. N. Cillis, S. Ciprini, R. Claus, J. Cohen-Tanugi, S. Condamoor, J. Conrad, R. Corbet, L. Corucci, L. Costamante, S. Cutini, D. S. Davis, D. Decotigny, M. DeKlotz, C. D. Dermer, A. de Angelis, S. W. Digel, E. do Couto e Silva, P. S. Drell, R. Dubois, D. Dumora, Y. Edmonds, D. Fabiani, C. Farnier, C. Favuzzi, D. L. Flath, P. Fleury, W. B. Focke, S. Funk, P. Fusco, F. Gargano, D. Gasparrini, N. Gehrels, F. X. Gentit, S. Germani, B. Giebels, N. Giglietto, P. Giommi, F. Giordano, T. Glanzman, G. Godfrey, I. A. Grenier, M. H. Grondin, J. E. Grove, L. Guillemot, S. Guiriec, G. Haller, A. K. Harding, P. A. Hart, E. Hays, S. E. Healey, M. Hirayama, L. Hjalmarsdotter, R. Horn, R. E. Hughes, G. Jóhannesson, G. Johansson, A. S. Johnson, R. P. Johnson, T. J. Johnson, W. N. Johnson, T. Kamae, H. Katagiri, J. Kataoka, A. Kavelaars, N. Kawai, H. Kelly, M. Kerr, W. Klamra, J. Knödlseeder, M. L. Kocian, N. Komin, F. Kuehn, M. Kuss, D. Landriu, L. Latronico, B. Lee, S. H. Lee, M. Lemoine-Goumard, A. M. Lionetto, F. Longo, F. Loparco, B. Lott, M. N. Lovellette, P. Lubrano, G. M. Madejski, A. Makeev, B. Marangelli, M. M. Massai, M. N. Mazziotta, J. E. McEnery, N. Menon, C. Meurer, P. F. Michelson, M. Minuti, N. Mirizzi, W. Mitthumsiri, T. Mizuno, A. A. Moiseev, C. Monte, M. E. Monzani, E. Moretti, A. Morselli, I. V. Moskalenko, S. Murgia, T. Nakamori, S. Nishino, P. L. Nolan, J. P. Norris, E. Nuss, M. Ohno, T. Ohsugi, N. Omodei, E. Orlando, J. F. Ormes, A. Paccagnella, D. Paneque, J. H. Panetta, D. Parent, M. Pearce, M. Pepe, A. Perazzo, M. Pesce-Rollins, P. Picozza, L. Pieri, M. Pinchera, F. Piron, T. A. Porter, L. Poupard, S. Rainò, R. Rando, E. Rapposelli, M. Razzano, A. Reimer, O. Reimer, T. Reposeur, L. C. Reyes, S. Ritz, L. S. Rochester, A. Y. Rodriguez, R. W. Romani, M. Roth, J. J. Russell, F. Ryde, S. Sabatini, H. F. W. Sadrozinski, D. Sanchez, A. Sand er, L. Sapozhnikov, P. M. Saz Parkinson, J. D. Scargle, T. L. Schalk, G. Scolieri, C. Sgrò, G. H. Share, M. Shaw, T. Shimokawabe, C. Shrader, A. Sierpowska-Bartosik, E. J. Siskind, D. A. Smith, P. D. Smith, G. Spandre, P. Spinelli, J. L. Starck, T. E. Stephens, M. S. Strickman, A. W. Strong, D. J. Suson, H. Tajima, H. Takahashi, T. Takahashi, T. Tanaka, A. Tenze, S. Tether, J. B.

- Thayer, J. G. Thayer, D. J. Thompson, L. Tibaldo, O. Tibolla, D. F. Torres, G. Tosti, A. Tramacere, M. Turri, T. L. Usher, N. Vilchez, V. Vitale, P. Wang, K. Watters, B. L. Winer, K. S. Wood, T. Ylinen, and M. Ziegler. The Large Area Telescope on the Fermi Gamma-Ray Space Telescope Mission. *Astrophys. J.*, 697(2):1071–1102, Jun 2009. doi: 10.1088/0004-637X/697/2/1071.
- W. Baade and F. Zwicky. Remarks on Super-Novae and Cosmic Rays. *Physical Review*, 46(1):76–77, Jul 1934. doi: 10.1103/PhysRev.46.76.2.
- J. W. M. Baars and A. P. Hartsuijker. The Decrease of Flux Density of Cassiopeia A and the Absolute Spectra of Cassiopeia A, Cygnus A and Taurus A. *Astr. Astrophys.*, 17:172, Mar 1972.
- K. R. Ballard and A. F. Heavens. Shock acceleration and steep-spectrum synchrotron sources. *Month. Not. Roy. Astr. Soc.*, 259(1):89–94, Nov 1992. doi: 10.1093/mnras/259.1.89.
- R. Bandiera, R. Neri, and R. Cesaroni. The Crab Nebula at 1.3 mm. Evidence for a new synchrotron component. *Astr. Astrophys.*, 386:1044–1054, May 2002. doi: 10.1051/0004-6361:20020325.
- W. Bednarek and M. Bartosik. Gamma-rays from the pulsar wind nebulae. *Astr. Astrophys.*, 405:689–702, Jul 2003. doi: 10.1051/0004-6361:20030593.
- A. R. Bell. The acceleration of cosmic rays in shock fronts - I. *Month. Not. Roy. Astr. Soc.*, 182:147–156, Jan 1978. doi: 10.1093/mnras/182.2.147.
- M. F. Bietenholz and P. P. Kronberg. The Magnetic Field of the Crab Nebula and the Nature of Its “Jet”. *Astrophys. J. Letters*, 357:L13, Jul 1990. doi: 10.1086/185755.
- M. F. Bietenholz, N. Kassim, D. A. Frail, R. A. Perley, W. C. Erickson, and A. R. Hajian. The Radio Spectral Index of the Crab Nebula. *Astrophys. J.*, 490(1):291–301, Nov 1997. doi: 10.1086/304853.
- M. F. Bietenholz, J. J. Hester, D. A. Frail, and N. Bartel. The Crab Nebula’s Wisps in Radio and Optical. *Astrophys. J.*, 615:794–804, November 2004. doi: 10.1086/424653.
- Roger Blandford and David Eichler. Particle acceleration at astrophysical shocks: A theory of cosmic ray origin. *Physical reports*, 154(1):1–75, Oct 1987. doi: 10.1016/0370-1573(87)90134-7.
- G. R. Blumenthal and R. J. Gould. Bremsstrahlung, Synchrotron Radiation, and Compton Scattering of High-Energy Electrons Traversing Dilute Gases. *Reviews of Modern Physics*, 42:237–271, 1970. doi: 10.1103/RevModPhys.42.237.

- R. Buehler, J. D. Scargle, R. D. Blandford, L. Baldini, M. G. Baring, A. Belfiore, E. Charles, J. Chiang, F. D'Ammando, and C. D. Dermer. Gamma-Ray Activity in the Crab Nebula: The Exceptional Flare of 2011 April. *Astrophys. J.*, 749(1):26, Apr 2012. doi: 10.1088/0004-637X/749/1/26.
- R. A. Chevalier. The interaction of supernovae with the interstellar medium. *Annu. Rev. Astron. Astrophys.*, 15:175–196, Jan 1977. doi: 10.1146/annurev.aa.15.090177.001135.
- Roger A. Chevalier. A Model for the X-Ray Luminosity of Pulsar Nebulae. *Astrophys. J.*, 539(1):L45–L48, Aug 2000. doi: 10.1086/312835.
- J. M. Comella, H. D. Craft, R. V. E. Lovelace, and J. M. Sutton. Crab Nebula Pulsar NP 0532. *Nature*, 221(5179):453–454, Feb 1969. doi: 10.1038/221453a0.
- K. Davidson and R. A. Fesen. Recent developments concerning the Crab Nebula. *Annu. Rev. Astron. Astrophys.*, 23:119–146, Jan 1985a. doi: 10.1146/annurev.aa.23.090185.001003.
- K. Davidson and R. A. Fesen. Recent developments concerning the Crab Nebula. *Annu. Rev. Astron. Astrophys.*, 23:119–146, Jan 1985b. doi: 10.1146/annurev.aa.23.090185.001003.
- Kris Davidson. Spectrophotometry of the Crab Nebula as a Whole. *The Astronomical Journal*, 94:964, Oct 1987. doi: 10.1086/114529.
- O. C. de Jager and A. K. Harding. The expected high-energy to ultra-high-energy gamma-ray spectrum of the Crab Nebula. *Astrophys. J.*, 396:161–172, September 1992. doi: 10.1086/171706.
- O. C. de Jager, A. K. Harding, P. F. Michelson, H. I. Nel, P. L. Nolan, P. Sreekumar, and D. J. Thompson. Gamma-Ray Observations of the Crab Nebula: A Study of the Synchro-Compton Spectrum. *Astrophys. J.*, 457:253, Jan 1996. doi: 10.1086/176726.
- L. Del Zanna, D. Volpi, E. Amato, and N. Bucciantini. Simulated synchrotron emission from pulsar wind nebulae. *Astr. Astrophys.*, 453(2):621–633, Jul 2006. doi: 10.1051/0004-6361:20064858.
- J. J. L. Duyvendak. Further Data Bearing on the Identification of the Crab Nebula with the Supernova of 1054 A.D. Part I. The Ancient Oriental Chronicles. *Astronomical Society of the Pacific*, 54(318):91–94, Apr 1942. doi: 10.1086/125409.
- Gilles Ferrand. *Étude de l'accélération des rayons cosmiques par les ondes de choc des restes de supernovae dans les superbulles galactiques*. PhD thesis, 2008.

- Robert A. Fesen, J. Michael Shull, and Alan P. Hurford. An Optical Study of the Circumstellar Environment Around the Crab Nebula. *The Astronomical Journal*, 113:354–363, Jan 1997. doi: 10.1086/118258.
- Markus Gaug. CTA Atmospheric Calibration. In *European Physical Journal Web of Conferences*, volume 144 of *European Physical Journal Web of Conferences*, page 01003, Jan 2017. doi: 10.1051/epjconf/201714401003.
- Gabriele Ghisellini. *Radiative Processes in High Energy Astrophysics*, volume 873. 2013. doi: 10.1007/978-3-319-00612-3.
- H. L. Gomez, O. Krause, M. J. Barlow, B. M. Swinyard, P. J. Owen, C. J. R. Clark, M. Matsuura, E. L. Gomez, J. Rho, and M. A. Besel. A Cool Dust Factory in the Crab Nebula: A Herschel Study of the Filaments. *Astrophys. J.*, 760(1):96, Nov 2012. doi: 10.1088/0004-637X/760/1/96.
- D. A. Green, R. J. Tuffs, and C. C. Popescu. Far-infrared and submillimetre observations of the Crab nebula. *Month. Not. Roy. Astr. Soc.*, 355(4):1315–1326, Dec 2004. doi: 10.1111/j.1365-2966.2004.08414.x.
- J. E. Grindlay and J. A. Hoffman. Compton-Synchrotron Spectrum of the Crab Nebula with the Pulsar Magnetic Field. *Astrophysics Letters*, 8:209, March 1971.
- A. F. Heavens and L. O’C. Drury. Relativistic shocks and particle acceleration. *Month. Not. Roy. Astr. Soc.*, 235:997–1009, Dec 1988. doi: 10.1093/mnras/235.3.997.
- Gregory S. Hennessey, Robert W. O’Connell, Kwang P. Cheng, Ralph C. Bohlin, Nicholas R. Collins, Theodore R. Gull, Paul Hintzen, Joan E. Isensee, Wayne B. Landsman, and Morton S. Roberts. Ultraviolet Imaging Telescope Observations of the Crab Nebula. *Astrophys. J.*, 395:L13, Aug 1992. doi: 10.1086/186477.
- J. J. Hester. The Crab Nebula: An Astrophysical Chimera. *Annu. Rev. Astron. Astrophys.*, 46:127–155, September 2008. doi: 10.1146/annurev.astro.45.051806.110608.
- J. Jeff Hester, James R. Graham, Charles A. Beichman, and III Gautier, T. N. Infrared and Optical Imagery of the Crab Nebula. *Astrophys. J.*, 357:539, Jul 1990. doi: 10.1086/168941.
- A. M. Hillas, C. W. Akerlof, S. D. Biller, J. H. Buckley, D. A. Carter-Lewis, M. Catanese, M. F. Cawley, D. J. Fegan, J. P. Finley, J. A. Gaidos, F. Krennrich, R. C. Lamb, M. J. Lang, G. Mohanty, M. Punch, P. T. Reynolds, A. J. Rodgers, H. J. Rose, A. C. Rovero, M. S. Schubnell, G. H. Sembroski, G. Vacanti, T. C. Weekes, M. West, and J. Zweerink. The Spectrum of Teravolt Gamma Rays from the Crab Nebula. *Astrophys. J.*, 503:744–759, August 1998. doi: 10.1086/306005.

- Peng-Yoke Ho, F. W. Paar, and P. W. Parsons. The Chinese guest star of A.D. 1054 and the Crab Nebula. *Vistas in Astronomy*, 13(1):1–13, Jan 1972. doi: 10.1016/0083-6656(72)90002-5.
- Werner Hofmann. Intercalibration of Cherenkov telescopes in telescope arrays. *Astroparticle Physics*, 20(1):1–3, Oct 2003. doi: 10.1016/S0927-6505(03)00137-3.
- M. Holler, D. Berge, C. van Eldik, J. P. Lenain, V. Marandon, T. Murach, M. de Naurois, R. D. Parsons, H. Prokoph, and D. Zaborov. Observations of the Crab Nebula with H.E.S.S. Phase II. *arXiv e-prints*, art. arXiv:1509.02902, Sep 2015.
- M. Holler, D. Berge, J. Hahn, D. Khangulyan, R. D. Parsons, and for the H. E. S. S. collaboration. Advanced search for the extension of unresolved TeV sources with H.E.S.S.: First measurement of the extension of the Crab nebula at TeV energies. *arXiv e-prints*, July 2017.
- IceCube Collaboration. Evidence for High-Energy Extraterrestrial Neutrinos at the IceCube Detector. *Science*, 342(6161):1242856, November 2013. doi: 10.1126/science.1242856.
- IceCube Collaboration, M. G. Aartsen, M. Ackermann, J. Adams, J. A. Aguilar, M. Ahlers, M. Ahrens, I. Al Samarai, D. Altmann, K. Andeen, T. Anderson, I. Anseau, G. Anton, C. Argüelles, B. Arsoli, J. Auffenberg, S. Axani, H. Bagherpour, X. Bai, J. P. Barron, S. W. Barwick, V. Baum, R. Bay, J. J. Beatty, J. Becker Tjus, K. H. Becker, S. BenZvi, D. Berley, E. Bernardini, D. Z. Besson, G. Binder, D. Bindig, E. Blaufuss, S. Blot, C. Boehm, M. Börner, F. Bos, S. Böser, O. Botner, E. Bourbeau, J. Bourbeau, F. Bradascio, J. Braun, M. Brenzke, H. P. Bretz, S. Bron, J. Brostean-Kaiser, A. Burgman, R. S. Busse, T. Carver, E. Cheung, D. Chirkin, A. Christov, K. Clark, L. Classen, S. Coenders, G. H. Collin, J. M. Conrad, P. Coppin, P. Correa, D. F. Cowen, R. Cross, P. Dave, M. Day, J. P. A. M. de André, C. De Clercq, J. J. DeLaunay, H. Dembinski, S. DeRidder, P. Desiati, K. D. de Vries, G. de Wasseige, M. de With, T. DeYoung, J. C. Díaz-Vélez, V. di Lorenzo, H. Dujmovic, J. P. Dumm, M. Dunkman, E. Dvorak, B. Eberhardt, T. Ehrhardt, B. Eichmann, P. Eller, P. A. Evenson, S. Fahey, A. R. Fazely, J. Felde, K. Filimonov, C. Finley, S. Flis, A. Franckowiak, E. Friedman, A. Fritz, T. K. Gaisser, J. Gallagher, L. Gerhardt, K. Ghorbani, P. Giommi, T. Glauch, T. Glüsenkamp, A. Goldschmidt, J. G. Gonzalez, D. Grant, Z. Griffith, C. Haack, A. Hallgren, F. Halzen, K. Hanson, D. Hebecker, D. Heereman, K. Helbing, R. Hellauer, S. Hickford, J. Hignight, G. C. Hill, K. D. Hoffman, R. Hoffmann, T. Hoinka, B. Hokanson-Fasig, K. Hoshina, F. Huang, M. Huber, K. Hultqvist, M. Hünnefeld, R. Hussain, S. In, N. Iovine, A. Ishihara, E. Jacobi, G. S. Japaridze, M. Jeong, K. Jero, B. J. P. Jones, P. Kalaczynski, W. Kang, A. Kappes,

- D. Kappesser, T. Karg, A. Karle, U. Katz, M. Kauer, A. Keivani, J. L. Kelley, A. Kheirandish, J. Kim, M. Kim, T. Kintscher, J. Kiryluk, T. Kittler, S. R. Klein, R. Koirala, H. Kolanoski, L. Köpke, C. Kopper, S. Kopper, J. P. Koschinsky, D. J. Koskinen, M. Kowalski, B. Krammer, K. Krings, M. Kroll, G. Krückl, S. Kunwar, N. Kurahashi, T. Kuwabara, A. Kyriacou, M. Labare, J. L. Lanfranchi, M. J. Larson, F. Lauber, K. Leonard, M. Lesiak-Bzdak, M. Leuermann, Q. R. Liu, C. J. Lozano Mariscal, L. Lu, J. Lünemann, W. Luszczak, J. Madsen, G. Maggi, K. B. M. Mahn, S. Mancina, R. Maruyama, K. Mase, R. Maunu, K. Meagher, M. Medici, M. Meier, T. Menne, G. Merino, T. Meures, S. Miarecki, J. Micallef, G. Momenté, T. Montaruli, R. W. Moore, R. Morse, M. Moulai, R. Nahnauer, P. Nakarmi, U. Naumann, G. Neer, H. Niederhausen, S. C. Nowicki, D. R. Nygren, A. Obertacke Pollmann, A. Olivas, A. O'Murchadha, E. O'Sullivan, P. Padovani, T. Palczewski, H. Pand ya, D. V. Pankova, P. Peiffer, J. A. Pepper, C. Pérez de los Heros, D. Pieloth, E. Pinat, M. Plum, P. B. Price, G. T. Przybylski, C. Raab, L. Rädcl, M. Rameez, K. Rawlins, I. C. Rea, R. Reimann, B. Relethford, M. Relich, E. Resconi, W. Rhode, M. Richman, S. Robertson, M. Rongen, C. Rott, T. Ruhe, D. Ryckbosch, D. Rysewyk, I. Safa, N. Sahakyan, T. Sälzer, S. E. Sanchez Herrera, A. Sandrock, J. Sandroos, M. Santander, S. Sarkar, S. Sarkar, K. Satalecka, P. Schlunder, T. Schmidt, A. Schneider, S. Schoenen, S. Schöneberg, L. Schumacher, S. Sclafani, D. Seckel, S. Seunarine, J. Soedingrekso, D. Soldin, M. Song, G. M. Spiczak, C. Spiering, J. Stachurska, M. Stamatikos, T. Stanev, A. Stasik, J. Stettner, A. Steuer, T. Stezelberger, R. G. Stokstad, A. Stöbl, N. L. Strotjohann, T. Stuttard, G. W. Sullivan, M. Sutherland, I. Taboada, J. Tatar, F. Tenholt, S. Ter-Antonyan, A. Terliuk, S. Tilav, P. A. Toale, M. N. Tobin, C. Toennis, S. Toscano, D. Tosi, M. Tselengidou, C. F. Tung, A. Turcati, C. F. Turley, B. Ty, E. Unger, M. Usner, J. Vandenbroucke, W. Van Driessche, D. van Eijk, N. van Eijndhoven, S. Vanheule, J. van Santen, E. Vogel, M. Vraeghe, C. Walck, A. Wallace, M. Wallraff, F. D. Wandler, N. Wand kowsky, A. Waza, C. Weaver, M. J. Weiss, C. Wendt, J. Werthebach, S. Westerhoff, B. J. Whelan, N. Whitehorn, K. Wiebe, C. H. Wiebusch, L. Wille, D. R. Williams, L. Wills, M. Wolf, J. Wood, T. R. Wood, K. Woschnagg, D. L. Xu, X. W. Xu, Y. Xu, J. P. Yanez, G. Yodh, S. Yoshida, and T. Yuan. Neutrino emission from the direction of the blazar TXS 0506+056 prior to the IceCube-170922A alert. *Science*, 361(6398):147–151, July 2018. doi: 10.1126/science.aat2890.
- E. Jourdain and J. P. Roques. 5 years of survey on the Crab Nebula with SPI/INTEGRAL. In *Proceedings of the 7th INTEGRAL Workshop*, page 143, Jan 2008.
- E. Jourdain, D. Götz, N. J. Westergaard, L. Natalucci, and J. P. Roques. INTEGRAL Cross-calibration Status: Crab observations between 3 keV and 1 MeV. In *Proceedings of the 7th INTEGRAL Workshop*, page 144, Jan 2008.

- C. F. Kennel and F. V. Coroniti. Confinement of the Crab pulsar's wind by its supernova remnant. *Astrophys. J.*, 283:694–709, August 1984. doi: 10.1086/162356.
- M. G. Kirsch, U. G. Briel, D. Burrows, S. Campana, G. Cusumano, K. Ebisawa, M. J. Freyberg, M. Guainazzi, F. Haberl, and K. Jahoda. Crab: the standard x-ray candle with all (modern) x-ray satellites. In Oswald H. W. Siegmund, editor, *UV, X-Ray, and Gamma-Ray Space Instrumentation for Astronomy XIV*, volume 5898 of *Society of Photo-Optical Instrumentation Engineers (SPIE) Conference Series*, pages 22–33, Aug 2005. doi: 10.1117/12.616893.
- Robert P. Kirshner. Spectrophotometry of the Crab Nebula. *Astrophys. J.*, 194:323–328, Dec 1974. doi: 10.1086/153248.
- F. S. Kitaura, H. Th. Janka, and W. Hillebrandt. Explosions of O-Ne-Mg cores, the Crab supernova, and subluminous type II-P supernovae. *Astr. Astrophys.*, 450(1): 345–350, Apr 2006. doi: 10.1051/0004-6361:20054703.
- L. Kuiper, W. Hermsen, G. Cusumano, R. Diehl, V. Schönfelder, A. Strong, K. Bennett, and M. L. McConnell. The Crab pulsar in the 0.75–30 MeV range as seen by CGRO COMPTEL. A coherent high-energy picture from soft X-rays up to high-energy gamma-rays. *Astr. Astrophys.*, 378:918–935, Nov 2001. doi: 10.1051/0004-6361:20011256.
- W. Kundt and E. Krotscheck. The Crab nebula - A model. *Astr. Astrophys.*, 83(1-2): 1–21, Mar 1980.
- P. O. Lagage and C. J. Cesarsky. The maximum energy of cosmic rays accelerated by supernova shocks. *Astronomy and Astrophysics*, 125:249–257, Sep 1983.
- S. Lebohec and J. Holder. The cosmic ray background as a tool for relative calibration of atmospheric Cherenkov telescopes. *Astroparticle Physics*, 19(2):221–233, May 2003. doi: 10.1016/S0927-6505(02)00201-3.
- J. C. Ling and Wm. A. Wheaton. Gamma-Ray Spectra and Variability of the Crab Nebula Emission Observed by BATSE. *Astrophys. J.*, 598(1):334–348, Nov 2003. doi: 10.1086/378700.
- M. S. Longair. *High Energy Astrophysics*. February 2011.
- P. Lundqvist, C. Fransson, and R. A. Chevalier. Photoionization of a fast shell around the Crab Nebula. *Astr. Astrophys.*, 162:L6–L8, Jul 1986.
- Yuri Lyubarsky. The termination shock in a striped pulsar wind. *Advances in Space Research*, 35(6):1112–1115, Jan 2005. doi: 10.1016/j.asr.2005.01.025.

- Maxim Lyutikov, Tea Temim, Sergey Komissarov, Patrick Slane, Lorenzo Sironi, and Luca Comisso. Interpreting Crab Nebula's synchrotron spectrum: two acceleration mechanisms. *Month. Not. Roy. Astr. Soc.*, 489(2):2403–2416, Oct 2019. doi: 10.1093/mnras/stz2023.
- K. K. Madsen, S. Reynolds, F. Harrison, H. An, S. Boggs, F. E. Christensen, W. W. Craig, C. L. Fryer, B. W. Grefenstette, C. J. Hailey, C. Markwardt, M. Nynka, D. Stern, A. Zoglauer, and W. Zhang. Broadband X-ray Imaging and Spectroscopy of the Crab Nebula and Pulsar with NuSTAR. *Astrophys. J.*, 801:66, March 2015. doi: 10.1088/0004-637X/801/1/66.
- K. Manolakou, D. Horns, and J. G. Kirk. Spectral evolution of non-thermal electron distributions in intense radiation fields. *Astr. Astrophys.*, 474(3):689–700, Nov 2007. doi: 10.1051/0004-6361:20078298.
- P. L. Marsden, F. C. Gillett, R. E. Jennings, J. P. Emerson, T. de Jong, and F. M. Olon. Far-infrared observations of the Crab nebula. *Astrophys. J.*, 278:L29–L32, Mar 1984. doi: 10.1086/184215.
- Jonatan Martín, Diego F. Torres, and Nanda Rea. Time-dependent modelling of pulsar wind nebulae: study on the impact of the diffusion-loss approximations. *Month. Not. Roy. Astr. Soc.*, 427(1):415–427, Nov 2012. doi: 10.1111/j.1365-2966.2012.22014.x.
- N. U. Mayall and J. H. Oort. Further Data Bearing on the Identification of the Crab Nebula with the Supernova of 1054 A.D. Part II. The Astronomical Aspects. *Astronomical Society of the Pacific*, 54(318):95–104, Apr 1942. doi: 10.1086/125410.
- Kevin Meagher. Six years of VERITAS observations of the Crab Nebula, 2015.
- M. Meyer, D. Horns, and H.-S. Zechlin. The Crab Nebula as a standard candle in very high-energy astrophysics. *Astr. Astrophys.*, 523:A2, November 2010. doi: 10.1051/0004-6361/201014108.
- P. G. Mezger, R. J. Tuffs, R. Chini, E. Kreysa, and H. P. Gemuend. Maps of Cassiopeia A and the Crab nebula at lambda 1.2 mm. *Astr. Astrophys.*, 167:145–150, Oct 1986.
- K. Nomoto. Evolutionary models of the Crab Nebula's progenitor. In M. C. Kafatos and R. B. C. Henry, editors, *The Crab Nebula and Related Supernova Remnants*, pages 97–113, Jan 1985.
- Ken'ichi Nomoto. Evolution of 8–10  $M_{sun}$  Stars toward Electron Capture Supernovae. II. Collapse of an O + NE + MG Core. *Astrophys. J.*, 322:206, Nov 1987. doi: 10.1086/165716.

- P. J. Owen and M. J. Barlow. The Dust and Gas Content of the Crab Nebula. *Astrophys. J.*, 801(2):141, Mar 2015. doi: 10.1088/0004-637X/801/2/141.
- J. Pétri and Y. Lyubarsky. Magnetic reconnection at the termination shock in a striped pulsar wind. *Astr. Astrophys.*, 473(3):683–700, Oct 2007. doi: 10.1051/0004-6361:20066981.
- Planck Collaboration, P. A. R. Ade, N. Aghanim, F. Argüeso, M. Arnaud, M. Ashdown, J. Aumont, C. Baccigalupi, A. J. Banday, and R. B. Barreiro. Planck 2015 results. XXVI. The Second Planck Catalogue of Compact Sources. *Astr. Astrophys.*, 594:A26, Sep 2016. doi: 10.1051/0004-6361/201526914.
- Oliver Porth, Serguei Komissarov, and Rony Keppens. 3D simulations of pulsar wind nebulae. In *40th COSPAR Scientific Assembly*, volume 40, pages E1.16–18–14, Jan 2014.
- G. Pühlhofer, O. Bolz, N. Götting, A. Heusler, D. Horns, A. Kohnle, H. Lampeitl, M. Panter, M. Tluczykont, and F. Aharonian. The technical performance of the HEGRA system of imaging air Cherenkov telescopes. *Astroparticle Physics*, 20(3): 267–291, Dec 2003. doi: 10.1016/j.astropartphys.2003.06.001.
- M. J. Rees and J. E. Gunn. The origin of the magnetic field and relativistic particles in the Crab Nebula. *Month. Not. Roy. Astr. Soc.*, 167:1–12, Apr 1974. doi: 10.1093/mnras/167.1.1.
- S. P. Reynolds and R. A. Chevalier. Evolution of pulsar-driven supernova remnants. *Astrophys. J.*, 278:630–648, Mar 1984. doi: 10.1086/161831.
- J. D. Scargle. Activity in the Crab Nebula. *Astrophys. J.*, 156:401, May 1969. doi: 10.1086/149978.
- Reinhard Schlickeiser. *Cosmic Ray Astrophysics*. 2002.
- Lorenzo Sironi and Anatoly Spitkovsky. Particle Acceleration in Relativistic Magnetized Collisionless Electron-Ion Shocks. *Astrophys. J.*, 726(2):75, Jan 2011. doi: 10.1088/0004-637X/726/2/75.
- Nathan Smith. The Crab nebula and the class of Type IIIn-P supernovae caused by sub-energetic electron-capture explosions. *Month. Not. Roy. Astr. Soc.*, 434(1):102–113, Sep 2013. doi: 10.1093/mnras/stt1004.
- Anatoly Spitkovsky and Jonathan Arons. Time Dependence in Relativistic Collisionless Shocks: Theory of the Variable “Wisps” in the Crab Nebula. *Astrophys. J.*, 603(2): 669–681, Mar 2004. doi: 10.1086/381568.

- David H. Staelin and III Reifenstein, Edward C. Pulsating Radio Sources near the Crab Nebula. *Science*, 162(3861):1481–1483, Dec 1968. doi: 10.1126/science.162.3861.1481.
- Tea Temim, Robert D. Gehrz, Charles E. Woodward, Thomas L. Roellig, Nathan Smith, Lawrence Rudnick, Elisha F. Polomski, Kris Davidson, Lunming Yuen, and Takashi Onaka. Spitzer Space Telescope Infrared Imaging and Spectroscopy of the Crab Nebula. *The Astronomical Journal*, 132(4):1610–1623, Oct 2006. doi: 10.1086/507076.
- D. F. Torres, J. Martín, E. de Oña Wilhelmi, and Analia Cillis. The effects of magnetic field, age and intrinsic luminosity on Crab-like pulsar wind nebulae. *Month. Not. Roy. Astr. Soc.*, 436(4):3112–3127, Dec 2013a. doi: 10.1093/mnras/stt1793.
- D. F. Torres, A. Cillis, J. Martín, and E. de Oña Wilhelmi. Time-dependent modeling of TeV-detected, young pulsar wind nebulae. *Journal of High Energy Astrophysics*, 1: 31–62, May 2014. doi: 10.1016/j.jheap.2014.02.001.
- Diego F. Torres, Analía N. Cillis, and Jonatan Martín Rodríguez. An Energy-conserving, Particle-dominated, Time-dependent Model of 3C 58 and Its Observability at High Energies. *Astrophys. J. Letters*, 763(1):L4, Jan 2013b. doi: 10.1088/2041-8205/763/1/L4.
- Virginia Trimble. Motions and Structure of the Filamentary Envelope of the Crab Nebula. *The Astronomical Journal*, 73:535, Sep 1968. doi: 10.1086/110658.
- J. Kelly Truelove and Christopher F. McKee. Evolution of Nonradiative Supernova Remnants. *The Astrophys. J. Supp.*, 120(2):299–326, Feb 1999. doi: 10.1086/313176.
- A. Unsöld and B. Baschek. Book Review: The new cosmos. - 5th ed. / Springer, 2001. *The Observatory*, 122(1167):125, Apr 2002.
- M. P. Veron-Cetty and L. Woltjer. Spectrophotometry of the continuum in the Crab Nebula. *Astr. Astrophys.*, 270:370–378, Mar 1993.
- D. Volpi, L. Del Zanna, E. Amato, and N. Bucciantini. Non-thermal emission from relativistic MHD simulations of pulsar wind nebulae: from synchrotron to inverse Compton. *Astr. Astrophys.*, 485(2):337–349, Jul 2008. doi: 10.1051/0004-6361:200809424.
- T. C. Weekes, M. F. Cawley, D. J. Fegan, K. G. Gibbs, A. M. Hillas, P. W. Kowk, R. C. Lamb, D. A. Lewis, D. Macomb, N. A. Porter, P. T. Reynolds, and G. Vacanti. Observation of TeV Gamma Rays from the Crab Nebula Using the Atmospheric Cerenkov Imaging Technique. *Astrophys. J.*, 342:379, Jul 1989. doi: 10.1086/167599.
- J. L. Weiland, N. Odegard, R. S. Hill, E. Wollack, G. Hinshaw, M. R. Greason, N. Jarosik, L. Page, C. L. Bennett, J. Dunkley, B. Gold, M. Halpern, A. Kogut,

- E. Komatsu, D. Larson, M. Limon, S. S. Meyer, M. R. Nolta, K. M. Smith, D. N. Spergel, G. S. Tucker, and E. L. Wright. Seven-year Wilkinson Microwave Anisotropy Probe (WMAP) Observations: Planets and Celestial Calibration Sources. *The Astrophys. J. Supp.*, 192(2):19, Feb 2011. doi: 10.1088/0067-0049/192/2/19.
- K. W. Weiler and N. Panagia. Are Crab-type Supernova Remnants (Plerions) Short-lived? *Astr. Astrophys.*, 70:419, Nov 1978.
- Martin C. Weisskopf, J. Jeff Hester, Allyn F. Tennant, Ronald F. Elsner, Norbert S. Schulz, Herman L. Marshall, Margarita Karovska, Joy S. Nichols, Douglas A. Swartz, and Jeffery J. Kolodziejczak. Discovery of Spatial and Spectral Structure in the X-Ray Emission from the Crab Nebula. *Astrophys. J. Letters*, 536(2):L81–L84, Jun 2000. doi: 10.1086/312733.
- K. C. Westfold. The Polarization of Synchrotron Radiation. *Astrophys. J.*, 130:241, July 1959. doi: 10.1086/146713.
- A. S. Wilson. The structure of the Crab Nebula-II. The spatial distribution of the relativistic electrons. *Month. Not. Roy. Astr. Soc.*, 160:355, 1972. doi: 10.1093/mnras/160.4.355.
- Paul K. H. Yeung and Dieter Horns. The Energy-dependent  $\gamma$ -Ray Morphology of the Crab Nebula Observed with the Fermi Large Area Telescope. *Astrophys. J.*, 875(2):123, Apr 2019. doi: 10.3847/1538-4357/ab107a.

# Acknowledgements

Several people have been involved with the past four years of my PhD life whom I would like to thank from the bottom of my heart for their constant support.

Firstly, I would like to express my sincere gratitude to my advisor Prof. Dr. Dieter Horns, for believing in me and giving me the opportunity to pursue research work in such an interesting topic. I am really grateful to him for his confidence in me, and for his continuous help, whenever I needed.

A heartfelt big thanks goes to Dr. Martin Tluczykont for his help regarding physics as well as computational problems. His patience and kindness was always an invaluable emotional support to me in all time of my PhD.

Besides my advisor, I would like to thank Prof. Dr. Günter Sigl for co-refereeing my thesis. My earnest thanks goes to the rest of my thesis committee: Prof. Daniela Pfannkuche, Prof. Jochen Liske, Marcus Brüggem, and Dr. Rolf Bühler, for their kind acceptance to be the part of the defense committee .

I would like to pay my special regards to the Deutsche Forschungsgemeinschaft (DFG), for providing the funding of my PhD and of the work related travel.

I wish to thank all the people who helped me for proof-reading this thesis and translating the abstract in german: Ali Baktash, Michael Blank, Dr. Le Hoang Nguyen, Haritha Retnakaran, Franziska Stief, Dr. Martin Tluczykont, and Thomas Wening.

A warm thanks goes to Rainer Peter Feller for his constant support regarding IT issues.

I am greatly indebted to Dr. Jhilik Majumdar with whom I shared the same office for more than two years and who has always supported me along the way. I also want to thank Chao Zhang for his kind help regarding computational issues, as well as our conversations about chinese history.

I thank my fellow officemates for their friendship, as well as their support regarding academic and non-academic concerns: Michael Blank, Yikun Gu, Dr. Le Hoang Nguyen,

Haritha Retnakaran, Franziska Stief, Paul Yeung. I also thank my dear group mates: Andrei Lobanov, Max Voss and Qixin Yu for making such a positive work environment.

I am also grateful to my long-time friends for their loyal friendship: Guilian Dessey, Lucas Grosset, Estelle Illous, Morgane König, Edouard Le cerf, Juliette Richoux, Jessica Robert, Marjorie Rousseau, and Romain Schira.

A special thank to Jelena Siegel who was there for me in the difficult moments and from whom I learned to always move step by step. I would like to thank the other friends that I have made in Hamburg: Anna und Alex, Hung-chun Chao, Farid Djabelkhir, Gautier Fayolle, Robert Stein, Thomas Wening. A special thank goes to H el ene for her support and patience, as well as for her cheerful guitar songs.

I am grateful to my parents, who have always believed in me and who have provided unconditional love and emotional support in my life. I am also grateful to my brothers, Salvador and Valentin.

And finally, last but by no means least, I cannot thank enough Dr. Coralie Bachy, Dr. Doris Folkerts, Prof. Dr. Christoph Keck, and Dr. Serge Kazandjian for their understanding and assistance during the toughest moments of these last years.

# Eidesstattliche Versicherung

*Declaration on oath*

Hiermit erkläre ich an Eides statt, dass ich die vorliegende Dissertationsschrift selbst verfasst und keine anderen als die angegebenen Quellen und Hilfsmittel benutzt habe.

*I hereby declare, on oath, that I have written the present dissertation by my own and have not used other than the acknowledged resources and aids.*

Hamburg

20th January, 2020

Unterschrift